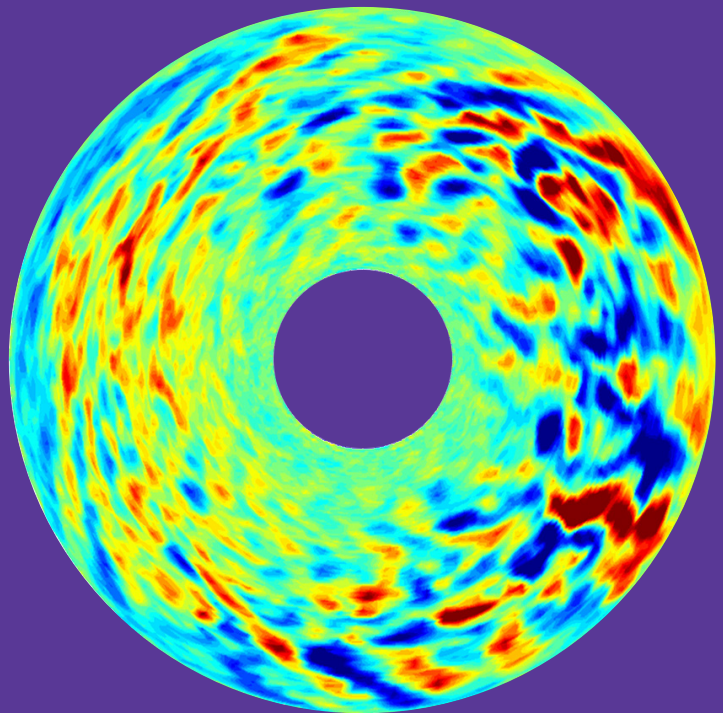


Gyrokinetic particle simulation for thermonuclear plasma turbulence studies in magnetic confinement

Salomon Janhunen



Gyrokinetic particle simulation for thermonuclear plasma turbulence studies in magnetic confinement

Salomon Janhunen

A doctoral dissertation completed for the degree of Doctor of Science (Technology) to be defended, with the permission of the Aalto University School of Science, at a public examination held in lecture hall K216 (Mechanical Engineering Building 1) on 19th of April 2013 at 12:00.

Aalto University
School of Science
Department of Applied Physics
Fusion and Plasma Physics

Supervising professor

Rainer Salomaa, Aalto University

Thesis advisor

Jukka Heikkinen, VTT

Preliminary examiners

Samuli Saarelma, CCFE, United Kingdom

Eric Serré, Université Aix Marseille, France

Opponents

Laurent Villard, École Polytechnique Fédéral Lausanne
Switzerland

Aalto University publication series

DOCTORAL DISSERTATIONS 56/2013

© Salomon Janhunen

ISBN 978-952-60-5098-0 (printed)

ISBN 978-952-60-5099-7 (pdf)

ISSN-L 1799-4934

ISSN 1799-4934 (printed)

ISSN 1799-4942 (pdf)

<http://urn.fi/URN:ISBN:978-952-60-5099-7>

Images: Salomon Janhunen

Unigrafia Oy

Helsinki 2013

Finland

Publication orders (printed book):

salomon.janhunen@aalto.fi

Author

Salomon Janhunen

Name of the doctoral dissertation

Gyrokinetic particle simulation for thermonuclear plasma turbulence studies in magnetic confinement

Publisher School of Science**Unit** Department of Applied Physics**Series** Aalto University publication series DOCTORAL DISSERTATIONS 56/2013**Field of research** Fusion and Plasma Physics**Manuscript submitted** 22 January 2013**Date of the defence** 19 April 2013**Permission to publish granted (date)** 20 March 2013**Language** English **Monograph** **Article dissertation (summary + original articles)****Abstract**

Thermal transport in a magnetised plasma is believed to be substantially enhanced due to turbulence. The ELMFIRE code has been developed for tokamak plasma turbulence studies in high temperature magnetized plasmas. ELMFIRE calculates the evolution of the Boltzmann equation in a magnetized plasma, including long scale interactions between particles calculated through field equations.

In this work we concentrate on benchmarking the ELMFIRE against published results from other turbulence codes, for instabilities (linear benchmarking) and turbulent heat flux (non-linear benchmarking). We investigate the effects of spatial and velocity-space resolution in the benchmarking cases.

Keywords fusion, plasma, transport, numerical simulation**ISBN (printed)** 978-952-60-5098-0**ISBN (pdf)** 978-952-60-5099-7**ISSN-L** 1799-4934**ISSN (printed)** 1799-4934**ISSN (pdf)** 1799-4942**Location of publisher** Espoo**Location of printing** Helsinki**Year** 2013**Pages** 183**urn** <http://urn.fi/URN:ISBN:978-952-60-5099-7>

Tekijä

Salomon Janhunen

Väitöskirjan nimi

Gyrokinetic particle simulation for thermonuclear plasma turbulence studies in magnetic confinement

Julkaisija Perustieteiden korkeakoulu**Yksikkö** Teknillinen fysiikka**Sarja** Aalto University publication series DOCTORAL DISSERTATIONS 56/2013**Tutkimusala** Fuusio ja plasmafysiikka**Käsikirjoituksen pvm** 22.01.2013**Väitöspäivä** 19.04.2013**Julkaisuluvan myöntämispäivä** 20.03.2013 **Kieli** Englanti **Monografia** **Yhdistelmäväitöskirja (yhteenveto-osa + erillisartikkelit)****Tiivistelmä**

Lämmön kuljetus magneettisesti koossapidetyssä plasmassa havaittiin odotettua suuremmaksi turbulenssin vuoksi. Simulointimalli nimeltä ELMFIRE on kehitetty Aalto Yliopiston ja VTT:n yhteistyössä tokamakissa havaittavan tehostuneen lämmön kuljetuksen tutkimiseen. ELMFIREssa käytetty malli perustuu kaasujen kineettiseen teoriaan, jota hyödyntäen voidaan simuloida fuusioreaktorissa tapahtuvia ilmiöitä ilman, että joudutaan olettamaan termodynaaminen tasapainotila (jota ei tokamakissa saavuteta).

Tutkimme tässä työssä ELMFIREn tuloksia kansainvälisessä kirjallisuudessa julkaistuihin tuloksiin, niin epävakaisuuksien kuin niistä syntyvän turbulenssin osalta.

Avainsanat fuusio, plasma, kuljetus, numeerinen mallinnus**ISBN (painettu)** 978-952-60-5098-0**ISBN (pdf)** 978-952-60-5099-7**ISSN-L** 1799-4934**ISSN (painettu)** 1799-4934**ISSN (pdf)** 1799-4942**Julkaisupaikka** Espoo**Painopaikka** Helsinki**Vuosi** 2013**Sivumäärä** 183**urn** <http://urn.fi/URN:ISBN:978-952-60-5099-7>

Preface

This thesis outlines some of the work done in the ELMFIRE group. The project was begun by Jukka Heikkinen, Timo Kiviniemi and me on 8th of December 2000 when I – as an undergraduate student – first printed out the MC code upon which we began to design the electric potential evaluations in real space. Since then the code has developed tremendously, and virtually none of the original lines of code exist anymore, after Francisco Ogando joined the group and introduced proper software development practices. The group has grown by two additional members: Susan Leerink who has concentrated on experimental comparisons and Tuomas Korpilo who has taken over code development. We believed then, as we still do now, that total distribution function calculations are the best way to simulate the complicated system that is the tokamak plasma from central axis to plasma-material boundary. We have been proven right since then, as most other groups have developed their own delta- f codes to incorporate full- f (or, total- f) characteristics.

Early on we decided to perform spectral analyses of the fluctuations, which are complicated by the simulation geometry through the rotational transform. Spectral analysis makes it possible to analyze the linear growth rates and frequencies of the instabilities, but a lot of optimization needed to be done on the simulation side, primarily due to the resource limits imposed, in retrospect. Since then the computational power of machines has grown by a factor of 2^{10} , but problem sizes have become much larger too.

A “standard” benchmarking regimen had emerged in the fusion community for turbulence codes through earlier publications by other authors, and because ELMFIRE incorporates many unique numerical methods, benchmarking of the code was begun in 2003 to improve general confidence in the results of the code. The standard regimen includes linear properties of geodesic acoustic modes and electrostatic drift-wave insta-

bilities, as well as saturation levels for transport and rotation. These had become very important since 1996, when Science magazine reported that “turbulence may sink titanic reactor” (according to computational predictions of the time), referring to Iter. Since then experimental scalings and more refined computational investigations have shown that such claims were premature, and additional understanding of transport is needed.

The ELMFIRE was one of the first particle codes to incorporate a working kinetic electron model, and as such most if not all of the benchmarks had to be performed with Boltzmann distributed electrons. The code was developed in close co-operation with the FT-2 tokamak group, who provided experimental data (starting from profiles) for us to analyze and reproduce with gyrokinetic simulations. The parameters of this experiment are well suited ELMFIRE simulations, because the small a/ρ_* value means that the simulation grid sizes do not need to be very high, and the high level of fluctuations also relax the simulation particle number needed. The high collisionality in this experiment also makes it possible to reach a neoclassical equilibrium relatively quickly.

All of the benchmark cases have been, alas, based on large tokamaks, and as such have been very expensive to simulate with ELMFIRE. The linear growth rate analysis for different wave lengths and non-linear saturation levels of the ITG/TEM branch of instability was quite involved computationally and the analysis needed to be developed over time to compensate for some of the restrictions imposed by computation. Whereas the FT-2 has been rather straightforward to simulate, the benchmark cases have even needed some code development to be amenable to analysis. The issue of turbulence saturation in the benchmark cases is still work under investigation, with new benchmark cases having been proposed within the TF-ITM framework that still need to be done, provided we are afforded some new computational resources.

In many ways, benchmarking has always had to go “against the wind”, because while such testing is crucial for the validity of the code, the cases investigated are also usually well known physics and as such can not provide new breakthroughs in turbulence and transport. However, history tells us that cross code benchmarking may in fact reveal new features of the physics involved in the non-linear regime because the models used to simulate the same physical system are different.

I would like to acknowledge the continued support given to me by Prof. Rainer Salomaa, who adopted me to the fusion group as an undergradu-

ate. I have also received support from Academy of Finland (SA), European Fusion Development Agreement (EFDA) in Association Euratom-Tekes, CSC Scientific Computing, and Wihuri Foundation. I would also like to thank my family, friends and Tuomas Karjalainen for the social support a person needs in his life.

Espoo, March 19, 2013,

Salomon Janhunen

Contents

Preface	1
Contents	5
List of Publications	7
Author's Contribution	9
1. Introduction	11
1.1 Particle trapping and curvature driven instabilities	15
1.2 The ELMFIRE code	15
2. Theoretical basis of ELMFIRE	19
2.1 Lagrangian computational cycle for the physics model	19
2.2 Kinetic description of plasma	20
2.3 Gyrokinetic Vlasov-Poisson system	22
2.4 Gyrokinetic theory as used in the ELMFIRE code	28
2.5 Magnetic and simulation geometry	33
3. Linear growth rate analyses	39
3.1 Linear growth of drift instability	39
3.2 The "Cyclone Base" case, with variations	46
3.2.1 TF-ITM Cyclone parameters	48
3.3 Adiabatic linear growth	49
3.4 Kinetic linear growth	52
4. Drift-wave driven transport	57
4.1 Introduction to drift-wave turbulence	57
4.1.1 The Hasegawa-Mima-Charney equation	58
4.2 The Cyclone Base case	60
4.2.1 Some background of the Cyclone cases	60

4.2.2	Adiabatic non-linear runs of Cyclone Base case	62
4.2.3	Initialisation and particle randomisation	64
4.2.4	Unphysical turbulence quenching mechanisms	66
4.2.5	Kinetic electron non-linear saturation	70
4.3	FT-2 simulations of turbulence and neoclassical physics . . .	72
4.3.1	Spectral investigations and dynamics of a flux-driven system	73
4.3.2	Neo-classical equilibrium and effect of turbulence . .	74
4.3.3	Long-term transport and comparison to Doppler re- flectometry	76
5.	Some numerical aspects of gyrokinetic particle simulation	79
5.1	Discretization, null-space and accuracy	79
5.1.1	Resolving power of a finite-differencing scheme	79
5.1.2	Comment on the implicit electron model	80
5.2	Quiescent initialization of the distribution function and toroidal randomization	82
5.3	Resolution requirements for simulations	84
5.4	Impact of averaging in neoclassical simulations	85
6.	Conclusions	87
	Bibliography	91
	Publications	97

List of Publications

This thesis consists of an overview and of the following publications which are referred to in the text by their Roman numerals.

I Heikkinen, Jukka.; Janhunen, Salomon; Kiviniemi, Timo; Ogando, Francisco. Full f gyrokinetic method for particle simulation of tokamak transport. *Journal of Computational Physics*, 227, pp.5582-5609, February 2008.

II Janhunen, Salomon; Ogando, Francisco; Heikkinen, Jukka; Kiviniemi, Timo; Leerink. Collisional dynamics of E_r in turbulent plasmas in toroidal geometry. *Nuclear Fusion*, 47 875-879, July 2007.

III Falchetto, Gloria; Scott, Bruce; Angelino, Paolo; Bottino, Andreas; Dannert, Tillman; Grandgirard, Virginie; Janhunen, Salomon; Jenko, Frank; Joliet, Sebastien; Kendl, Alex; McMillan, Ben; Naulin, Volker; Nielsen, A H; Ottaviani, Maurizio; Peeters, Arthur. The European turbulence code benchmarking effort: turbulence driven by thermal gradients in magnetically confined plasmas. *Plasma Physics and Controlled Fusion*, 50 1-12, 2008.

IV Henriksson, Svante; Janhunen, Salomon; Kiviniemi, Timo; Heikkinen, Jukka. Global spectral investigation of plasma turbulence in gyrokinetic simulations. *Physics of Plasmas*, 7 072303-7, 2006.

V Janhunen, Salomon; Kiviniemi, Timo; Heikkinen, Jukka; Korpilo, Tuomas; Leerink, Susan; Nora, Markus; Ogando, Francisco. Recent Ad-

vances in Gyrokinetic Full-f Particle Simulation of Medium Sized Tokamaks with ELMFIRE. *Contributions to Plasma Physics*, **50** 252-255, 2010.

VI Heikkinen, Jukka; Korpilo, Tuomas; Janhunen, Salomon; Kiviniemi, Timo; Leerink, Susan; and Ogando, Francisco. Interpolation for momentum conservation in 3D toroidal gyrokinetic particle simulation of plasmas. *Computer Physics Communications*, **183** 1719, 2012.

VII Leerink, Susan; Bulanin, Viktor; Gurchenko, Alexey; Gusakov, Evgeniy; Heikkinen, Jukka; Janhunen, Salomon; Altukhov, Alexey; Esipov, L; Kantor, M. Yu; Kiviniemi, Timo; Korpilo, Tuomas; Kuprienko, Dimitry; Lashkul, Serguey; Petrov, A.. Multi-scale investigations of drift wave turbulence and plasma flows: Measurements and full f gyrokinetic simulations. *Physical Review Letters*, **109** 165001, 2012.

Author's Contribution

Publication I: “Full f gyrokinetic method for particle simulation of tokamak transport”

As a co-author in this publication, the author of the thesis contributed to all parts of the text. The following investigations were performed by the author: linear and non-linear investigations of drift-wave turbulence, specifically section 5 introduction, and subsections 5.2, 5.3. The figures 1, 3, 4, 7 and 8 were produced by the author. The author has contributed to the development of the simulation model from the beginning.

Publication II: “Collisional dynamics of E_r in turbulent plasmas in toroidal geometry”

The author wrote the paper, produced all the pictures and replied to the criticism given by the referee.

Publication III: “The European turbulence code benchmarking effort: turbulence driven by thermal gradients in magnetically confined plasmas”

The author performed the transport analyses by ELMFIRE required for the paper, submitted data (including Q and n spectra) and reviewed the manuscript. The work related to this publication is described in Chapter 4. The author was the primary contributor from the ELMFIRE group. In this thesis, we discuss results that were not added to the paper.

Publication IV: “Global spectral investigation of plasma turbulence in gyrokinetic simulations”

In addition to revising the manuscript, the author contributed to the paper by developing analysis techniques required for spectral analysis, and discussing the results and techniques with the primary author on a daily basis. The author also contributed part of referee reply.

Publication V: “Recent Advances in Gyrokinetic Full-f Particle Simulation of Medium Sized Tokamaks with ELMFIRE”

The author provided everything to the paper except Section 3, which was done by Timo Kiviniemi. The author also corresponded with the referee of the paper.

Publication VI: “Interpolation for momentum conservation in 3D toroidal gyrokinetic particle simulation of plasmas”

The author did some of the investigations leading to the results, investigated the numerical instability observed and demonstrated the null-space of the momentum conserving operator (see section 5.1) in solution of polarization. Pictures 4, 5 and 6 were made by the author.

Publication VII: “Multi-scale investigations of drift wave turbulence and plasma flows: Measurements and full f gyrokinetic simulations”

The author contributed to the revision of the manuscript and discussed the work on a daily basis with the main author, contributed simulations and diagnostic programs for this work. The increase of radial resolution to improve turbulent saturation was suggested by the author of this thesis, which led to a drastic improvement in the results. The reason for this improvement is detailed in section 5.3. Also the neo-classical filtering developed in this thesis was used in the simulations to produce a neo-classical steady state before turbulence was allowed to develop.

1. Introduction

We live a precarious existence here on Earth, currently without the option to leave. Clearly a balance of resource use and waste management is difficult to achieve, and the network of feedback on Earth is complicated [1], and not very well understood. Human history is riddled with examples of fallen cultures, the most notable of which have been ancient Egyptians and the Mayan culture [2]. More often than not, environmental factors much less severe than the ones mentioned earlier have played into these collapses, which have occurred at the height of the culture's prosperity. To make a long story short, the reason why cultures collapse when no-one would expect them to (during their height) has to do with poor stewardship of depletable natural resources and slowly creeping man-made environmental damage, which is compounded by natural changes. Society has become more dependent on crops and agricultural techniques with stricter conditions for success, and when natural variation tips the balance, society falls. Here, improved agricultural technologies have made an unsustainable population growth (Malthusian catastrophe) possible, and their failure has made conditions during collapse much more severe.

Fusion reactions provide the possibility of satisfying the future energy requirements of humanity for millennia without the loss of quality of life, provided that other space¹ and resource limits are heeded. Access to a previously unusable energy source with limited environmental impact and vast reserves but potential society changing prospects is something that cannot be foregone easily.

Commercial fusion is a high technology area, where no advance comes easily. While a number of other approaches have been proposed for confinement of the plasma state required for thermonuclear fusion reactions

¹The experiments by John B. Calhoun on mice are a stark example of space as a limiting factor.

(e.g., inertial, electrostatic-inertial, to name a few), the best performance has been obtained by magnetic confinement up to date. The flagship of magnetic confinement is the *tokamak*, which astounded the fusion community in the late 60's by the high level of confinement achieved. Old newspapers of that period have predictions that the tokamak would start producing commercial fusion energy in 10 years time. This was not, alas, realized. The problem is that the tokamak operates in a state of self-organized criticality, where any deviations from the critical state introduces instabilities which degrade confinement (much like in a sand pile or a bank of snow).

Thermal transport in a magnetised plasma is intimately related to the biggest unsolved physics problem of turbulence. Turbulence is the very cause why heat escapes from the plasma core much more efficiently than through mere collisional transport, and why even the most successful magnetic fusion devices of today are not sufficient to produce commercial fusion power. While through experimental projections it has been estimated that a bigger reactor² will produce a significant excess of fusion energy, understanding of the physics involved in the heat and particle transport of such a machine in operation is still quite rudimentary. Many difficult engineering problems are also expected for a bigger reactor — and by no means do we wish to underestimate the effort needed to build such a machine as an international project where the parts are manufactured all over the world.

The tokamak has been the most successful geometry to date in terms of performance, and has been therefore the subject of intensive research. Since its invention by Tamm and Sakharov in the 1950's, the performance of the tokamak has steadily improved, and many aspects of the physics involved are well understood. Until fairly recently, the global magneto-hydrodynamic (MHD) stability (before beginning of 1970's) was a question of concern. At the same time, heating and accumulation of impurities have been extensively investigated, while more lately improving confinement has been one of the most important objectives. In current experiments MHD quasi-stable plasmas with constrained but desirable density and current profiles are generated regularly, and some very important confinement modes have been discovered. The confinement times of energy and density in the tokamak — and in other magnetic confinement

²The Iter experiment, <http://www.iter.org>

schemes – scale roughly as

$$\tau_E \sim \frac{L_r^2}{\chi},$$

where L_r is the characteristic scale length (related to the size) of the device, and χ is the characteristic diffusivity. To lengthen the confinement time τ_E (and therefore, improve the efficiency of the reactor), we must either enlarge the device or reduce overall diffusivity (i.e., transport). Building larger and larger devices is ultimately economically prohibitive, so reducing transport is a preferred way to improve performance. However, this requires improved understanding on physics of the transport coefficient, which needs additional scientific focus on the subject.

Although the plasma in current tokamak experiments is usually stable to global MHD modes which would destroy the confinement altogether, the plasma is always in a state of thermodynamic quasi-equilibrium with an abundance of free energy for driving more benign instabilities, which reduce the confinement time through convective-dominated transport (i.e., turbulence). Confinement modes which are observed to suppress this micro-turbulence (such as the high confinement mode, or H-mode) have been found experimentally. One of the outstanding problems of transport processes in tokamaks is the physics of achieving H-mode conditions (L-H transition) and in general transport barrier formation, explanation of which has attracted several possible hypotheses ranging from purely neoclassical (rotational runaway and orbit losses) to modulational instabilities between turbulent eddies and zonal flows [3,4]. Kinetic effects are important, because modes undergo Landau damping. Full f gyrokinetic simulation (the framework of this thesis) allows for the investigation of all these processes that affect the *distribution function* f of kinetic theory simultaneously. This is the relative advantage of ELMFIRE.

Earlier in the field people dreamt of building a comprehensive database of turbulence simulation scalings, which could be called upon to predict transport levels and flows of any experimental set-up [5]. However, as they were building this database, it was realised that at least seven normalized parameters (Larmor radius ρ_* , collisionality ν_* , ratio of dynamic to magnetic pressure β_p , ion-electron temperature ratio τ , inverse aspect ratio ε , safety factor q , curvature κ) were needed for such a database. Because the number of required simulations grows exponentially as a function of free parameters, it has since been recognized that it is much cheaper to run each of these cases separately with a turbulence code rather than build a database. Integrated multi-scale simulation platforms

(such as the one developed by European Fusion Development Agreement Task Force Integrated Tokamak Modelling, EFDA TF-ITM) where transport coefficients are received from turbulence codes and incorporated into macroscopic transport simulations are being developed to address this issue.

The basic tenets of science are that any hypothesis needs to be falsifiable, and steps must be taken to attempt to falsify it. Nothing can be proven right in this context, but at least a decent attempt to prove them wrong has to be made. This is the basic theme of this thesis: validation and verification of the ELMFIRE , to build confidence in any results that are derived from simulations. Validation is where the numerical model and the theoretical basis are compared, and verification is testing predictions given by the code to well known physical systems, other codes and experiments. Of course, as with any scientific hypothesis, falsification follows abandoning the previous hypothesis and developing a new one (in this case, remedying the code or theoretical basis). This cycle is never complete.

The thesis is built as follows: in Chapter 2 we describe drifts and particle trapping, and outline the most relevant drift-wave instabilities driven unstable by drifts. In Chapter 3 we attempt to describe concisely the linear benchmarking work which includes linear analyses of plasma waves in various experimental settings. Chapter 4 contains characterisation of turbulence and some results found while simulating the non-linear state after the linear transient. We also discuss some observations made during the benchmarking process, practical requirements for running the ELMFIRE code, and new diagnostics included in the ELMFIRE package of programs. The various benchmarking conditions are discussed. In Chapter 5 we include a discussion of some important numerical aspects that have been found during the development of the ELMFIRE code. The conclusions in Chapter 6 are followed by the set of collected articles that are referenced to in the thesis.

A theoretical survey of the model used in the ELMFIRE has been published based on two different perturbation theories, namely Lie transformations and Kruskal averaging co-ordinates, due to concern whether the Krylov-Bogoliubov averaging retain the Hamiltonian nature of the system. We shall talk about this in the next chapter.

1.1 Particle trapping and curvature driven instabilities

The matter inside the reaction vessel of the Tokamak is heated to high temperatures for fusion reactions to take place, and in this state the majority of atoms have been fully ionised. The bulk of ions and electrons in the vessel constitutes a *plasma*, which is confined by the use of the Lorentz force in strong magnetic fields. The kinetic theory of plasma (see for example Ref. [6]) is obtained by separating the large scale collective behaviour and small scale particle to particle interactions, which are treated as a scattering process. This approach drastically reduces the dimensionality of the problem (from 6^N to 6 dimension in phase space), which is further reduced through gauge transformations (or averaging, whichever one prefers) to a $5 + 1$ dimensional phase space using gyrokinetic approximations, which also modify the collisional operator slightly. In the following theoretical treatment we shall concentrate on the collective motion of particles and mostly neglect the scattering process for simplicity, while they are included in the code. The plasma in thermonuclear devices satisfies conditions for classical physics very well, so we neglect quantum mechanical aspects of the system except for the electron Coulomb logarithm in collisions. Also, relativistic effects (such as retarded potentials) are neglected for simplicity. These approximations are justified by the relatively low energy and density of the bulk tokamak plasma considered in transport calculations, but are not always applicable in all of fusion research.

1.2 The ELMFIRE code

Computational physics has become an indispensable tool in fusion research because experiments are expensive, take a long time to prepare, and measurements of some important phenomena and quantities are very difficult with existing equipment, requiring specific experimental set-ups. Simulations are used in optimization of experiments and plasma characteristics, in the prediction of planned experiments, and interpretation of experimental results. New simulation models are also being developed to aid in theoretical work.

Plasma turbulence is believed to be one of the main processes leading to enhanced (anomalous) radial transport observed in tokamaks, which reduce the confinement to unacceptable levels. Small scale, low frequency instabilities drive that turbulence and its study is therefore of crucial im-

portance for improving confinement efficiency. The overall interaction of those small scale processes can however be correctly simulated with global simulations that cover all, or a significant part, of the whole tokamak. In order to reproduce interesting processes where the particle distribution function deviates from Maxwellian, kinetic methods are needed. As most interesting processes occur at a characteristic frequency much lower than the particle gyration around the magnetic field, the gyrokinetic model was introduced, first for the linear regime [7] and later for nonlinear problems [8, 9]. This method produced considerable savings in computation by ignoring the high frequency phenomena of not relevant importance.

The gyrokinetic method was further simplified with the assumption that particle distributions are close to a known kind (e.g. Maxwellian), introducing the δf technique [10]. This method allows for further reduction in computation at the expense of limiting its range of accuracy due to its assumption on the particle distribution. With the δf approach, gyrokinetic plasma simulation has become a standard tool for transport analysis in toroidal magnetic fusion devices, under conditions of weak perturbations [11–16]. All these methods calculated the electrostatic potential from a complicatedly modified Poisson equation, and lacked a proper treatment of the electromagnetic perturbations with multiscale structures in both space and time. A different way to express the same problem was presented later [17] with a scheme based on Krylov-Boholiubov averaging method where the polarization drift is included into the equations of motion. Also considerations for inhomogeneous plasma and electromagnetic fluctuations have been developed [18] for the gyrokinetic model.

Another simplification commonly used applies to the consideration of electrons. Their inertia may be neglected by considering an adiabatic model, resulting in further computational savings. One of the reasons why the study of kinetic electrons has received little attention is mainly due to computational difficulty as electrons move much faster than ionic species. However lately new techniques are being developed [19] to study their influence on unstable modes, like the ETG.

From the gyrokinetic theory, two main approaches have been followed for computational resolution of the intervening equations: deterministic and Monte Carlo particle in cell (PIC) codes. Both approaches can work under both δf and full f models, have been intensively tested [20] producing similar results with still remarkable persistent differences regarding

zonal flows [21] which have influence on transport and conductivity.

The ELMFIRE code [22] solves the gyrokinetic full f equations for quasi-neutrality with a PIC algorithm based on a variation of the gyrokinetic model developed in reference [17]. The main difference to the standard theory is the definition of the gyroaveraging procedure, where the $E \times B$ velocity is subtracted from the particle velocity. The main features of the numerical solution of the model are described in section 2.1. In Chapter 3 and Chapter 4 the results of standard comparison benchmarks [12] are presented, both in the linear and saturation regimes. By linear testing we refer to growth rate and phase evolution of most unstable modes (the equations which are linear), while in non-linear cases saturation levels of heat conductivity are investigated. These tests are not applicable as comparisons to experimental data, however there are enough computational results from different models to serve as a benchmark of sufficient confidence.

As ELMFIRE solves the gyrokinetic equations with a Monte Carlo method, its results suffer from statistical noise that arises from using a finite number of test particles. Noise production in PIC codes has been widely studied in Ref. [23], but beyond this simulations of ETG instability [24] have shown the possibility of noise strongly affecting growth rates. The study of noise and initialisation influence on results is therefore a key issue, and is addressed in Chapter 3. Finally conclusions show the key points regarding the development of ELMFIRE and its applications. The ELMFIRE code has been used for analyzing the turbulence spectra in tokamak plasmas (PIV).

The code is being developed as a co-operative project of Aalto University School of Science and VTT Technical Research Centre of Finland to investigate transport phenomena in the tokamak, especially in the scrape-off layer (SOL) where plasma comes directly into contact with solid matter (a limiter or a divertor). In such conditions it is expected that large deviations from the equilibrium distribution function may be observed due to kinetic effects, and that the electron and ion species both contribute to the physics observed. Because kinetic effects and non-linear polarization are important, conventional fluid models can not be used effectively in this regime to study the forementioned problems. It is important to note that while δf codes need to iterate with an external transport model to model experiments, full f codes can develop meaningful comparisons to experiments with suitable sources and sinks.

2. Theoretical basis of ELMFIRE

2.1 Lagrangian computational cycle for the physics model

The computational algorithm of the gyrokinetic full- f model ELMFIRE is best categorised as a Lagrangian explicit/implicit predictor-corrector solver for the Boltzmann equation in a magnetized plasma. The computational cycle is illustrated in figure 2.1. The distribution function f is represented as a discrete sample, and evolved by advancing the localised phase space volume (i.e., test particle or marker) with its Hamiltonian equations of motion. In this way, the distribution function may be evolved

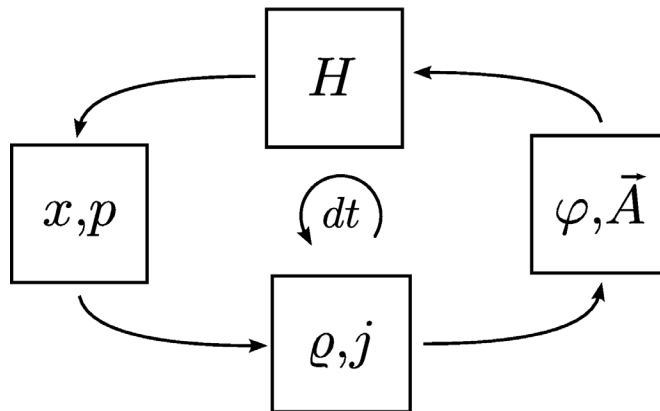


Figure 2.1. The Hamiltonian computational cycle of ELMFIRE . From the top, particles move according to their Hamiltonian equations without polarization, and the polarization operator is collected. Fields are solved from quasi-neutrality using the polarization operator, and the polarization is applied to the particles and collisions are applied. A new Hamiltonian is obtained, and the cycle begins anew.

particle by particle using field data obtained from the previous time step, and the polarization drift motion contribution is estimated and applied afterwards. This method (some controversy in nomenclature exists between

implicit or predictor-corrector¹) has several features which may be useful in turbulence simulations. It includes non-linear polarization which is usually neglected, and eases calculations of the polarization operator for non-Maxwellian distributions.

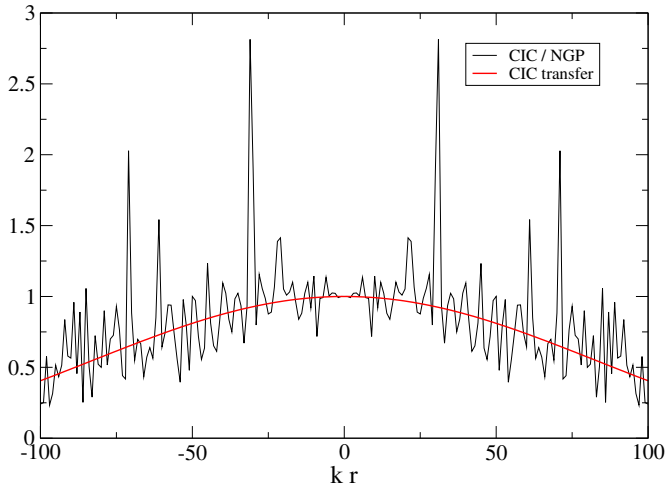


Figure 2.2. Measured spectral transfer function of the cloud-in-cell (CIC) interpolation technique in relation to the nearest-grid-point (NGP) method (relative amplitudes). The CIC method introduces filtering of the particle density by distributing particle weight on the grid. The analytical transfer function is $g(kr) = 4 \sin^2(\pi kr/N)/(2\pi kr/N)^2$ with $N = 200$.

The polarization response is estimated by taking finite sized particles [25] and estimating the density response to the polarization motion. This is constrained by quasi-neutrality, and a solution for the electric field at the beginning of the next time step is obtained. This method has been found to be very stable in practice, but finite sized particles introduce additional filtering on the grid (see figure 2.2) which may be numerically important. Numerical properties of this method, and if it may be used in conjunction with advanced numerical methods such as finite volume methods, may need to be investigated in the future.

2.2 Kinetic description of plasma

The *Boltzmann equation* of a multi-species plasma (usually one species of ions, and the electron species) is given in the Lagrangian (or material) coordinates by

$$\frac{df_a}{dt} = C_i(f_a) \quad (2.1)$$

¹A question raised in discussions with Harold Weitzner, Courant Institute, NYU.

where f is the distribution function, species $a, i \in \{\text{ions, electrons}\}$,

$$\frac{d}{dt} = \frac{\partial}{\partial t} + \sum_i \frac{dz_i}{dt} \frac{\partial}{\partial z_i} \quad (2.2)$$

for any set of non-Cartesian coordinates z_i , and C_i is the species-to-species collision operator which we will discuss later. The Boltzmann equation essentially expresses the conservation of the distribution function f_a in time in the coordinate system which follows the plasma species in question. We shall ignore the collision term $C_i(f_a)$ in the following analysis, although it is included in the numerical model. The collisionless Boltzmann equation for plasma is called the *Vlasov equation*.

The electromagnetic field acts as a body force for the distribution-fluid, and in the presence of magnetic and electric fields (\vec{B} and \vec{E} , respectively), the Vlasov equation in the Eulerian (or phase space) coordinates becomes

$$\frac{\partial f_a}{\partial t} + \vec{v} \cdot \vec{\nabla} f_a + \frac{q_a}{m_a} [\vec{E} + \vec{v} \times \vec{B}] \cdot \vec{\nabla}_v f_a = 0, \quad (2.3)$$

where $f(\vec{x}, \vec{v}; t)$, $\vec{\nabla} = \sum_k i_k \frac{\partial}{\partial x_k}$ and $\vec{\nabla}_v = \sum_k i_k \frac{\partial}{\partial v_k}$ are the partial differential operators in the Cartesian rectangular phase space (\vec{x}, \vec{v}) with i_k as its unit vectors, q_a and m_a are the charge and mass of the particle species in question. While it might seem that Eq. (2.1) and Eq. (2.3) are completely different equations altogether, the difference between them is that Eq. (2.1) is stated in the frame of the fluid in Lagrangian co-ordinates (as opposed to external observer of the Eulerian co-ordinates), and thus the systems do not differ for our choice of interactions except for the collision term.

A plasma consists of charged particles (namely, electrons and ions), and as such, any fluctuations in the relative densities of particle species and their velocities in the plasma result in an electromagnetic field, which obeys the *Maxwell's equations*

$$\begin{cases} \vec{\nabla} \cdot \vec{E} = \frac{Q}{\varepsilon_0}, & \vec{\nabla} \times \vec{E} = -\frac{\partial \vec{B}}{\partial t}, \\ \vec{\nabla} \cdot \vec{B} = 0, & \vec{\nabla} \times \vec{B} = \mu_0 \vec{j} + \frac{1}{c^2} \frac{\partial \vec{E}}{\partial t}, \end{cases} \quad (2.4)$$

where ε_0 and μ_0 are the permittivity and permeability of vacuum, \vec{j} is the current density, $c = 1/\sqrt{\varepsilon_0 \mu_0}$ is the speed of light in vacuum. Charge density Q and current density \vec{j} in terms of the distribution functions f_a are given by the *constitutive relations*

$$Q = \sum_a q_a \int f_a d^3v, \quad \vec{j} = \sum_a q_a \int \vec{v} f_a d^3v. \quad (2.5)$$

It is the coupling between motion and fields (Eqs. 2.3 and 2.4) to which plasma owes its complex and highly nonlinear nature which exhibits itself in all scales of interest.

The Vlasov-Maxwell system of equations as stated in Eqs. (2.3) and (2.4) can not be utilised directly in numerical simulations for processes that occur in the drift-wave or transport time scale. The system imposes strict limits on the temporal and spatial resolutions due to fast processes associated with particle motion (e.g., cyclotron motion and plasma oscillations²), but fortunately these processes can be dealt with by using a perturbative approach which we outline in Section 2.3.

It can be shown that the Vlasov equation can be transformed to single (and multiple) particle dynamics through the application of point particles in the form of delta functionals (*Klimontovich distribution*), so we will use the gyrokinetic theory interchangeably as single particle theory in the following discussion.

2.3 Gyrokinetic Vlasov-Poisson system

There are a number of ways to perturbatively expand the Vlasov-Maxwell system over the particle gyro-motion, which yield a set of gyrokinetic equations [9, 18, 26, 27]. There exists a wealth of theoretical literature on this issue beyond the references given. In this presentation we shall opt to take clarity over completeness, and for a thorough derivation of the gyrokinetic system the reader is advised to peruse the references. Great care has to be taken to end up with equations that conserve the phase space and avoid secular terms. The expansion is still being debated in the scientific literature and is by no means entirely finished at the time of writing this thesis. Gyrokinetic theory by itself is of interest not only to fusion physics, but also to space plasma physics.

The Vlasov equation (2.3) includes the fast time scale associated with particle gyro-motion in the magnetic field. This motion has the period $\Omega = q_a B/m$, which is called the *cyclotron resonance frequency*, and it appears in the $\frac{q_a}{m_a} \vec{v} \times \vec{B} \cdot \vec{\nabla}_v f_a$ term in Eq. (2.3). The averaging (or gauge transformation) removes the fast time scales associated with the gyro-motion, but retains the finite Larmor radius effects. These effects are important in turbulence simulations, because they affect the growth rates of instabilities and their saturation levels.

²The plasma oscillation is removed by numerical dissipation.

The Vlasov (or Boltzmann) equation can be transformed to any coordinates (the coordinate system in Eq. (2.2) is arbitrary) to facilitate the gyro-averaging procedure. A natural choice of coordinates are the *gyro-centre coordinates*, given by

$$\begin{cases} \vec{x} = \vec{R} + \vec{\rho} \\ \vec{v} = \vec{v}_{\parallel} + \vec{v}_{\perp} = v_{\parallel} \hat{b} + v_{\perp} (\hat{e}_1 \cos \alpha + \hat{e}_2 \sin \alpha), \end{cases} \quad (2.6)$$

where \vec{R} is the gyro-centre coordinate, $\vec{\rho} = \Omega^{-1} \hat{b} \times \vec{v}$ is the Larmor radius, $\hat{b} = \frac{\vec{B}}{B} = \hat{e}_1 \times \hat{e}_2$ is the unit vector along the magnetic field, v_{\parallel} is the velocity component parallel to the magnetic field, v_{\perp} is the perpendicular velocity component, α is the gyro-angle. We define the *magnetic moment* as the lowest order adiabatic invariant $\mu = v_{\perp}^2/2B$, which arises as an invariant during development of the perturbation theory.

The gyrokinetic equations are obtained from the Vlasov-Maxwell system by assuming the *gyrokinetic ordering*,

$$\frac{\omega}{\Omega} = O(\epsilon), \quad \frac{\rho}{L} = O(\epsilon), \quad L \sim L_{\parallel}, \quad \frac{v_{E \times B}}{v_{\text{th}}} = O(\epsilon), \quad (2.7)$$

where ω is the frequency of the perturbations, L is the characteristic background scale length, L_{\parallel} is the scale length of the perturbations parallel to the magnetic field lines, $\vec{v}_{E \times B}$ is $E \times B$ drift velocity, v_{th} is the characteristic thermal velocity of the distribution, and ϵ is a smallness parameter. Two other frequently taken approximations in transport models are the *drift ordering*, where the finite Larmor radius effects are ignored by taking $\rho/L \rightarrow 0$, and the *MHD ordering* with $v_{E \times B}/v_{\text{th}} = O(1)$. The drift ordering may be utilized for the kinetic electron species.

The transformation to the gyro-centre coordinates $(\vec{R}, \mu, v_{\parallel}, \alpha)$ allows us to write the unperturbed Vlasov equation Eq. (2.3) as

$$\begin{aligned} \frac{\partial f}{\partial t} + \left(\vec{v}_{\parallel} + \frac{\vec{E} \times \vec{B}}{B^2} \right) \cdot \vec{\nabla}_R f - \Omega \frac{\partial f}{\partial \alpha} \\ + \vec{v} \cdot \left(-\vec{\nabla} \vec{\rho} \cdot \vec{\nabla}_R f + \vec{\nabla} v_{\parallel} \frac{\partial f}{\partial v_{\parallel}} + \vec{\nabla} \mu \frac{\partial f}{\partial \mu} + \vec{\nabla} \alpha \frac{\partial f}{\partial \alpha} \right) \\ + \frac{q_e}{m} \vec{E} \cdot \left(\hat{b} \frac{\partial f}{\partial v_{\parallel}} + \frac{\vec{v}_{\perp}}{B} \frac{\partial f}{\partial \mu} + \frac{\hat{b} \times \vec{v}_{\perp}}{v_{\perp}^2} \frac{\partial f}{\partial \alpha} \right) = 0. \end{aligned} \quad (2.8)$$

It is interesting to note that through the co-ordinate transformation we have separated drift-motion generating terms and the terms associated with cyclotron oscillation.

The system may then be averaged by $\langle \cdot \rangle_{\alpha} = (2\pi)^{-1} \int \cdot \delta(\vec{x} - \vec{\rho}) d\alpha$, and the system is solved to first order in ϵ , and gyrokinetic equations correct

to $O(\epsilon^2)$ are obtained. The gyrokinetic equation is given by

$$\begin{aligned} \frac{\partial \langle f \rangle_\alpha}{\partial t} + \frac{1}{B_\parallel^*} \left(\vec{v}_\parallel + \vec{v}_d + \frac{\langle \vec{E} \rangle_\alpha \times \vec{B}}{B^2} \right) \cdot \vec{\nabla}_R \langle f \rangle_\alpha \\ + \left(\vec{a}_\parallel + \frac{q_e}{m} \langle \vec{E} \rangle_\alpha \cdot \hat{b} \right) \frac{\partial \langle f \rangle_\alpha}{\partial v_\parallel} = C(f_i) \end{aligned} \quad (2.9)$$

where the drift of the gyro-centre \vec{v}_d and the parallel acceleration a_\parallel are defined by

$$\vec{v}_d \equiv \vec{b} \times \left(\frac{v_\parallel^2}{\Omega} \hat{b} \cdot \vec{\nabla} \hat{b} + \frac{v_\perp^2}{2\Omega} \vec{\nabla} \ln B \right), \quad (2.10)$$

$$a_\parallel \equiv -\frac{v_\perp^2}{2} \hat{b} \cdot \vec{\nabla} \ln B, \quad (2.11)$$

$$B_\parallel^* = B \left(1 + \frac{v_\parallel}{\Omega} \hat{b} \cdot \vec{\nabla} \times \hat{b} \right). \quad (2.12)$$

The gyro-centre drift includes the curvature and gradient drifts which are important in inhomogeneous magnetic fields (such as the field in a tokamak). The parallel acceleration a_\parallel is usually neglected as a higher order term, and B_\parallel^* is the phase space Jacobian. It is important to note that we omit in this treatment the ponderomotive terms in the gyrokinetic electric potential for simplicity. The total distribution is expressed as follows:

$$f = \langle f \rangle_\alpha + \epsilon g = \langle f \rangle_\alpha + \frac{q_e}{mB} (\phi - \langle \phi \rangle_\alpha) \frac{\partial \langle f \rangle_\alpha}{\partial \mu}. \quad (2.13)$$

The Maxwell equations can be transformed in the same manner, giving their gyrokinetic electromagnetic equivalents. We consider only electrostatic perturbations and a static magnetic field background, which gives us the gyrokinetic Poisson equation

$$\nabla^2 \phi + \frac{q_e^2}{mB\epsilon_0} \int (\phi - \langle \phi \rangle_\alpha) \frac{\partial \langle f \rangle_\alpha}{\partial \mu} \delta(\vec{R} + \vec{\rho} - \vec{x}) d\vec{R}d\vec{v} = -\frac{1}{\epsilon_0} (q_e \tilde{n}_i - en_e), \quad (2.14)$$

and the electric field is given by $\vec{E} = -\vec{\nabla}\phi$. The second term on the left hand side is the *polarization density*. ELMFIRE includes the polarization drift in the equations of motion and calculates the electric field from quasi-neutrality. This approach is given to more detail in section 2.4. In ELMFIRE the polarization density is inseparable from the gyrocenter density.

The electron Larmor radius is smaller than the ion Larmor radius by a factor of $\sqrt{m_e/m_i} \approx 1/60$, so we may use the *drift-kinetic equation* for the electrons:

$$\frac{\partial f_0}{\partial t} + \frac{1}{B_\parallel^*} \left(\vec{v}_\parallel + \vec{v}_d + \frac{\vec{E} \times \vec{B}}{B^2} \right) \cdot \vec{\nabla}_R f_0 + \left(a_\parallel + \frac{q_e}{m} \vec{E} \cdot \hat{b} \right) \frac{\partial f_0}{\partial v_\parallel} = 0. \quad (2.15)$$

In some investigations where the electron kinetics are of no interest the response of electrons to charge imbalances are thought to be instantaneous (which they generally are not due to trapping). In this case the electron species can be assumed to be *adiabatic*, and the electron response can be expressed through the Maxwell-Boltzmann distribution:

$$f_e(x, v) = e^{-\frac{H}{k_B T}},$$

$$n_e(\vec{x}) = \int f(x, v) dV_v = n_{e0} e^{-\frac{q_e \delta \phi}{k_B T_e}} \approx n_{e0} \left(1 - \frac{q_e \delta \phi}{T_e} + O(\epsilon^2) \right), \quad (2.16)$$

where n_{e0} is the electron background density and T_e is the electron temperature, H is the Hamiltonian and $\delta \phi$ is the electric perturbation. While the implementation of a kinetic electron model is entirely non-trivial, the adiabatic model is very simple: the electron contribution appears only in the polarization equation. Electron trapping does, however, play an important role in transport simulations as a mechanism for charge imbalance and drift-wave drive. Both the kinetic and adiabatic electron models have been implemented successfully in the ELMFIRE .

The electrostatic gyrokinetic equations presented are nonlinear, non-local (due to gyroaveraging) and allow deviations from the equilibrium distribution. This gives us great confidence that they allow simulating the core plasma as well as the scrape-off layer plasma (with provisions). The gyrokinetic equation may be developed to a hierarchy of gyrofluid equations in analogous manner to the standard development of MHD equations from the Vlasov equation.

The effect of trapping is two-fold. The compressibility generated by the magnetic drifts drive previously stable drift modes unstable, and the trapping of electrons causes a non-adiabatic response which may also drive instabilities due to imperfect charge neutralization by the fields. In figure 2.3 we show some of the primary types of particle orbits in the absence of electric fields. There is a discontinuous transition from a passing orbit to a trapped orbit, and different probability distribution ($\propto 1/v_r$) for density. The radial velocity of the trapped and passing particles in figure 2.3 are shown in figure 2.4. This complicates initialization because the Maxwell-Boltzmann distribution is not adequate.

The equations of motion that would be obtained from the gyrokinetic equations using the Klimontovich representation for the distribution could be used to simulate the individual particles. However, numerically it is advantageous to simulate the canonical equations of motion because oscillating integrands (due to magnetic field inhomogeneity) are difficult to

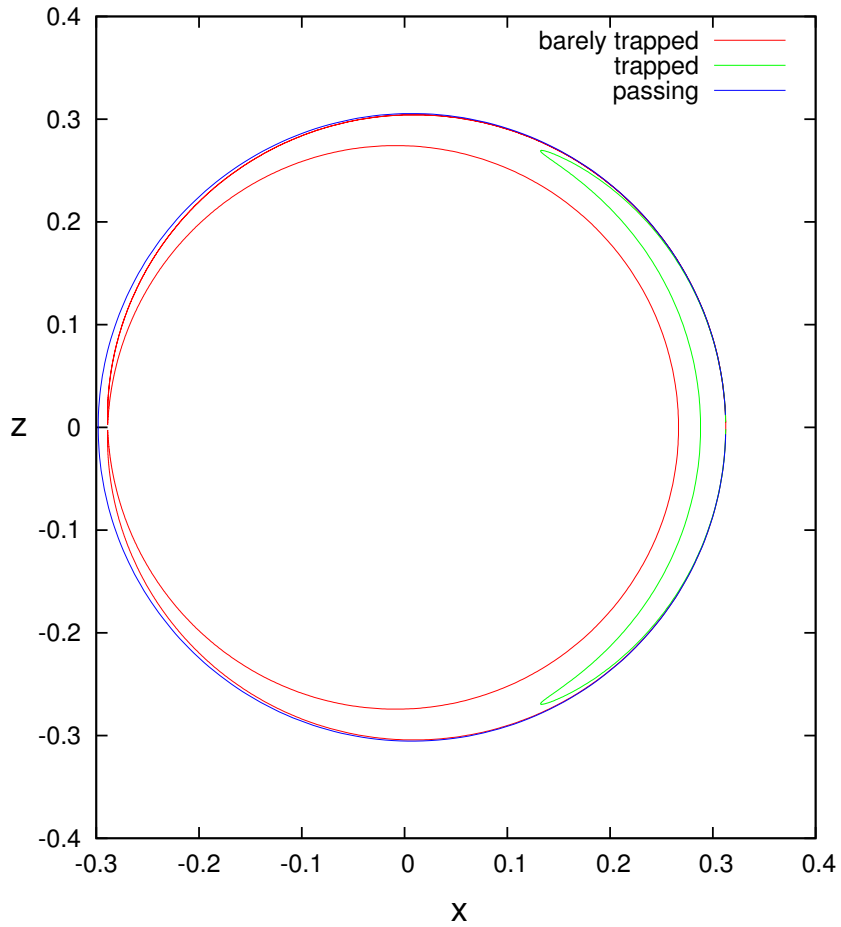


Figure 2.3. Orbits for particles with different pitches calculated with the LISCO code (by Heikkinen, Kurki-Suonio & Carlsson). Note the discontinuity in inboard probability density due to transition from trapped to passing particle orbit topology.

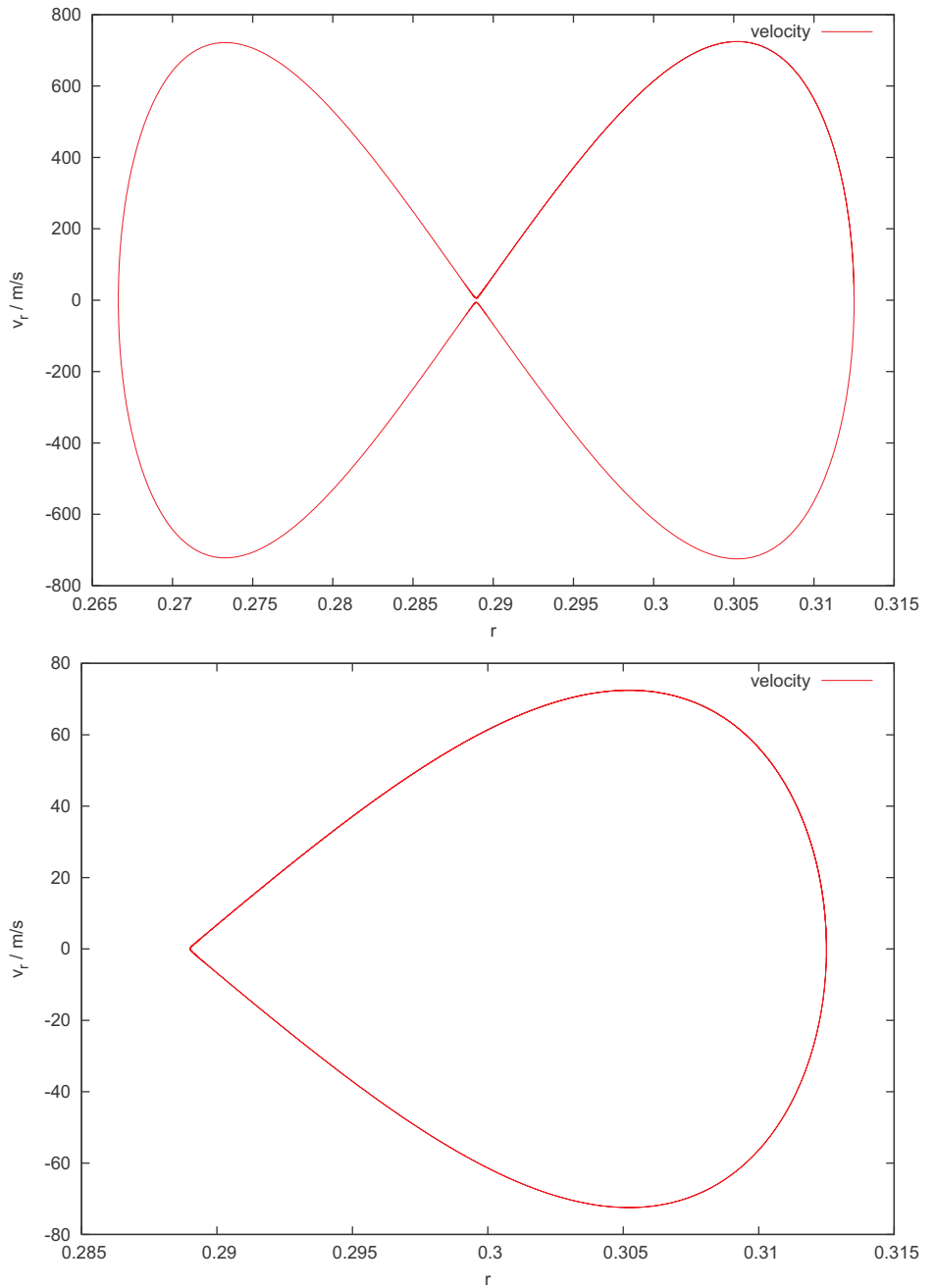


Figure 2.4. Radial velocity for the barely trapped and barely passing particles. We see that the left lobe is cut off after transition to passing.

accurately simulate. We shall talk about the magnetic field and equations of motion in section 2.5.

2.4 Gyrokinetic theory as used in the ELMFIRE code

Gyrokinetic equations of motion, Poisson equation, and energy and momentum conservation laws were derived in [27] based on the reduced-phase-space Lagrangian and inverse Kruskal iteration [28]. This formalism together with the choice of the adiabatic invariant $J = \langle \vec{p} \cdot \partial \vec{x} / \partial \phi \rangle$ as one of the averaging coordinates in phase space provides an alternative to the standard gyrokinetics, and has been adopted as the basis of development for ELMFIRE. These equations, developed to the 2nd order in gyrokinetic smallness parameter, do not show explicit ponderomotive-like (in potential) or polarization-like (in density) terms. Gyrophase and field dependent gyroradius functions through gyroaveraged coordinates can be used in direct numerical integration of the gyrokinetic equations in particle simulation of the field and particles with full distribution function, using *pullback* and *push-forward* transformation mappings. This allows, for example, the choice between gyrokinetic systems with polarization drift either present or absent in the equations of motion. From a full- f particle simulation standpoint, this is simpler than numerical solution of complicated integro-differential equations for the polarization density.

In the following we shall neglect the magnetic inhomogeneity and perturbations for simplicity. However, it is straightforward to extend the equations for inhomogeneous magnetic field using the same procedure as in the following, but also as relying on the formalism as shown in the previous section. A similar extension to perturbed magnetic field is also feasible when based on the general equations quoted in [28, 29]. The gyrokinetic orderings $\omega/\Omega \sim \rho/L \sim \epsilon$ and $E_{\perp}/(BV_{\perp}) \sim \epsilon$ for perturbations are adopted. The latter condition for the limit of the magnitude of the $\vec{E} \times \vec{B}$ drift velocity may be considered mandatory for the iteration procedure applied in the present formalism.

A necessary ordering is that electrostatic potential and related variations in particle distribution can have large long-wavelength components but only small short-wavelength components, i.e., $|\hat{b} \times \vec{E}| \sim vB\epsilon$ for the electric field \vec{E} , where $\hat{b} = \vec{B}/B$ is the unit vector along the magnetic field \vec{B} and \vec{v} is the particle velocity. Otherwise, macroscopic variables are assumed to vary on a scale longer than gyroradius ρ , i.e., $\nabla \sim 1/L$

with $L \sim \rho/\epsilon$. Here, ϵ is an expansion parameter of the gyrokinetic theory to obtain the averaged slow motion behind the fast gyro-oscillation, i.e., $t \rightarrow s = t/\epsilon$. Usually in gyrokinetics, and also in the present work, one assumes the macroscopic variables to vary in time slower than the gyroperiod, i.e., $d/dt = 1/T$ with $T \sim \Omega/\epsilon = (eB/m)/\epsilon$.

The gyrokinetic transformation involves transformation from the coordinates \vec{x}, \vec{v} to \vec{R}, U, J, ϕ , which allows to describe the particle slow motion in terms of only \vec{R}, U, J without explicit dependence on the gyroangle like variable ϕ . Here, \vec{R} defines a so called gyrocentre position by $\vec{\rho} = \vec{x}(R, U, J, \phi, t) - \vec{R}$ with $\vec{\rho}$ denoting gyroradius like variable. U has a correspondence to the particle parallel velocity along the magnetic field, and J to the gyro-oscillation energy of the particle. For implementation of the inverse Kruskal iteration [28, 30, 31] for this purpose and to follow the denotation adopted in [28], we adopt the following definitions $\vec{v} = u_{\parallel} \hat{b} + u_{\perp} \vec{n}_1$ with $\vec{n}_1 = -\sin(\theta) \hat{e}_1 - \cos(\theta) \hat{e}_2$ and $\vec{n}_2 = \cos(\theta) \hat{e}_1 - \sin(\theta) \hat{e}_2$, and $\vartheta = \theta/2\pi$, and denote $(\vec{x}, u_{\parallel}, u_{\perp}, \vartheta) \equiv (\vec{y}, \vartheta)$. Here, given in right-hand-rule order, the unit vectors perpendicular to the magnetic field are $\hat{e}_1 = \hat{b} \cdot \nabla \hat{b} / |\hat{b} \cdot \nabla \hat{b}|$ and $\hat{e}_2 = \hat{b} \times \hat{e}_1$, and thus depend only on \vec{x} . The particle-related basis set with \vec{n}_1 and \vec{n}_2 depends in addition to \vec{x} also on the instantaneous orientation of the particle velocity in terms of the angle θ .

The spatial components of the velocity in transformed coordinates \vec{g} are ordered as

$$\vec{g}_x^{(0)} = U \hat{b} + V_{\perp} \vec{n}_1 \quad (2.17)$$

$$\begin{aligned} \vec{g}_x^{(1)} &= \vec{g}_x^{(0)} + (u_{\parallel}^{(1)} - U) \hat{b} + (u_{\perp}^{(1)} - V_{\perp}) \vec{n}_1 - 2\pi(\vartheta^{(1)} - \phi) V_{\perp} \vec{n}_2 \\ &= \vec{g}_x^{(0)} + \frac{\epsilon}{\omega^{(0)}} \frac{e}{m} \left[\int^{\phi} (\hat{b} \cdot \vec{E}(\vec{x}^{(1)}, \epsilon s) - \hat{b} \cdot \vec{E}(\vec{R}, \epsilon s)) d\phi \hat{b} \right. \\ &\quad + \int^{\phi} \vec{n}_1 \cdot \vec{E}(\vec{x}^{(1)}, \epsilon s) d\phi \vec{n}_1 \\ &\quad \left. + \int^{\phi} (\vec{n}_2 \cdot \vec{E}(\vec{x}^{(1)}, \epsilon s) - \langle \vec{n}_2 \cdot \vec{E}(\vec{x}^{(1)}, \epsilon s) \rangle) d\phi \vec{n}_2 \right]. \quad (2.18) \end{aligned}$$

Denoting $\vec{G} = \vec{g}_x^{(1)} - \vec{g}_x^{(0)}$, one can find from the above equation using partial integration that $\langle \vec{G} \rangle = \langle \vec{G}_{\perp} \rangle = (\epsilon/\omega^{(0)})(e/m) \langle \vec{E} \times \hat{b} \rangle / (2\pi)$. Here, $\langle \vec{n}_1 \cdot \vec{E} \rangle = 0$ follows from the electrostatic relation $2\pi(V_{\perp}/\Omega) \vec{n}_1 \cdot \vec{E}(\vec{x}^{(1)}, \epsilon s) = -\partial\Phi(\vec{x}^{(1)}, \epsilon s)/\partial\phi$.

One may then write directly for the solution of $\vec{x}^{(2)}$ and for the gyror-

dius $\vec{\rho}^{(2)}$ up to this order

$$\begin{aligned} \vec{\rho}^{(2)} = \vec{x}^{(2)} - \vec{R} &= \frac{\epsilon}{2\pi\omega^{(0)}} V_{\perp} \vec{n}_2 + \frac{\epsilon}{\omega^{(0)}} \int^{\phi} \vec{G}_{\parallel} d\phi \\ &+ \frac{\epsilon}{2\pi\omega^{(0)}} \hat{b} \times \vec{G} - \frac{\epsilon^2}{2\pi[\omega^{(0)}]^2} \frac{e}{m} \hat{b} \times \int^{\phi} (\vec{E} - \langle \vec{E} \rangle) d\phi + \epsilon^2 \vec{x}_{c2}. \end{aligned} \quad (2.19)$$

In the above equations \vec{E} is evaluated at position $\vec{x}^{(1)}$. Without loss of freedom, one may set $\langle \int^{\phi} (\vec{E} - \langle \vec{E} \rangle) d\phi \rangle = 0$ and $\langle \int^{\phi} \vec{G}_{\parallel} d\phi \rangle = 0$. The integration constant \vec{x}_{c2} can be chosen otherwise arbitrarily. Evidently, with this integration constant one can control whether the drift velocities are let to affect the gyroradius or not (e.g., the $\langle \vec{E} \rangle \times \vec{B}$ drift contribution through the $\hat{b} \times \vec{G}$ term to $\vec{\rho}$). As it will turn out later in our formalism, this constant also determines whether the polarization drift appears in the drift velocity, and similarly whether the so called polarization density will appear explicitly in the gyrokinetic Poisson equation.

As shown in [27] the potential variation within this formalism gives the Poisson equation

$$\epsilon_0 \nabla \cdot \vec{E}(\vec{r}, t) = \sum_{p.s.} e \int d^3 R dU dJ f_p \langle \delta(\vec{r} - \vec{x}) \rangle - \nabla_r \cdot P, \quad (2.20)$$

where the Dirac's delta function has been used to express the variation $\delta_f \Phi(\vec{x}, t) = \int d^3 r \delta(\vec{r} - \vec{x}) \delta_f \Phi(\vec{r}, t)$. The so called polarization term $\nabla_r \cdot P$ collects the rest of the variation terms. Its detailed form is not expressed here. It turns out that this term is zero to the iteration order considered in the present work.

The present formalism has conservation laws for the energy and angular momentum. Within the framework of Kruskal's theory, it is most natural to identify the gyrocentre position \vec{R} with the point \vec{r} in this context. Integration of the obtained local energy conservation law with respect to \vec{r} yields the following expression for the total energy

$$K = \int \left\{ \frac{1}{2} \epsilon_0 E^2 + \frac{1}{2\mu_0} B^2 + \vec{E} \cdot \vec{P} + \sum_{p.s.} \int dU dJ \left[f_p \left\langle \frac{m}{2} v^2 \right\rangle \right]_{\vec{R}=\vec{r}} \right\} d^3 r. \quad (2.21)$$

Similarly, for the total angular momentum \vec{L} of the system one obtains

$$\begin{aligned} \vec{L} = \int \left\{ \vec{r} \times \left[\epsilon_0 \vec{E} \times \vec{B} + \vec{P} \times \vec{B} + \sum_{p.s.} \int dU dJ [f_p \langle m \vec{v} \rangle]_{\vec{R}=\vec{r}} \right] \right. \\ \left. + \sum_{p.s.} \int dU dJ [f_p \langle \vec{\rho} \times m \vec{v} \rangle]_{\vec{R}=\vec{r}} \right\} d^3 r. \end{aligned} \quad (2.22)$$

The corresponding local expressions of the energy and angular momentum conservation laws can be found in [29]. The latter can be more useful

in diagnostics of the energy and angular momentum in simulation codes, as in diagnostics the inflow and outflow of energy or momentum through any boundary of the diagnostic region has to be accounted for in any practical realization.

Using the iterated solutions for $\vec{x}^{(2)}$ and $\vec{v}^{(1)}$ obtained earlier, one finds $\hat{A} = \vec{A} + (m/e)U\hat{b} + 2\pi m\omega^{(0)}\epsilon\hat{b} \times \vec{x}_{c2}$, $\hat{A}_U = 0$, $\partial\hat{\Phi}/\partial U = (m/e)U$. Therefore from the equations of motion one obtains to second order in ϵ

$$\begin{aligned}\vec{V}_R &= \dot{R} = U\hat{B}/B^* + \hat{E} \times \hat{b}/B^* \\ V_U &= \dot{U} = (e/m)\hat{B} \cdot \hat{E}/B^*\end{aligned}\quad (2.23)$$

with $B^* = B[1 + 2\pi m(\omega^{(0)}/B)\epsilon\nabla \times (\hat{b} \times \vec{x}_{c2}) \cdot \hat{b}]$ and $\hat{B} = \vec{B} + 2\pi m\omega^{(0)}\epsilon\nabla \times (\hat{b} \times \vec{x}_{c2})$. To express these in terms of the electric field \vec{E} one needs to calculate \hat{E} [27].

After some algebra one finds

$$\begin{aligned}e\hat{E} &= \langle e\vec{E} \rangle - m \left[\frac{\partial\langle\vec{G}\rangle}{\partial t} + \langle\vec{G}\rangle \cdot \frac{\partial\langle\vec{G}\rangle}{\partial\vec{R}} \right] \\ &+ m \left[\frac{\partial(\langle\vec{G}_\perp\rangle + \vec{H})}{\partial t} + \langle\vec{G}_\perp\rangle \cdot \frac{\partial(\langle\vec{G}_\perp\rangle + \vec{H})}{\partial\vec{R}} \right] + O(\epsilon^3).\end{aligned}\quad (2.24)$$

Here $\vec{H} = \epsilon^2(e/m)\vec{x}_{c2} \times \vec{B}$. In obtaining Eq. (2.24), one exploited the identity

$$\left\langle \Delta \frac{\partial(\vec{x}^{(2)} - \vec{x}^{(1)})}{\partial\phi} \cdot \int^\phi (\vec{E}_\perp - \langle\vec{E}_\perp\rangle) d\phi \right\rangle = \left\langle \frac{\partial(\vec{x}^{(2)} - \vec{x}^{(1)})}{\partial\phi} \cdot \Delta \int^\phi (\vec{E}_\perp - \langle\vec{E}_\perp\rangle) d\phi \right\rangle, \quad (2.25)$$

where Δ is any differential operator acting on the expression immediately in front of it and commuting with ϕ integration.

Equations (2.23) with the expression (2.24) provide the gyrokinetic equations of motion for \vec{R} and U correct to second order in ϵ . It is of interest to note that with the integration constant \vec{x}_{c2} one is able affect the appearance of the drift motion in this presentation. Choosing $\vec{x}_{c2} = 0 = \vec{H}$, one effectively leaves only the $\langle\vec{E}\rangle \times \vec{B}$ drift in the perpendicular drift motion, while the choice $\vec{H} = -\langle\vec{G}_\perp\rangle$ introduces also the polarization drift motion (which comes from the convective time derivative of $\langle\vec{E}\rangle \times \vec{B}$ motion) into the perpendicular drift motion. It's important to note that with these choices, it was also defined whether the $\langle\vec{E}\rangle \times \vec{B}$ drift motion was allowed to affect the gyroradius in Eq. (2.19) or not. That the appearance of the polarization drift in the drift motion is in this way connected to the definition of the gyroradius in gyrokinetics was already noted by P. Sosenko et al [17]. It is the power of the present inverse Kruskal iteration procedure

where the choice of the presence of the polarization drift in drift motion can be simply turned on or off in due course of developing the formalism within the same theory expansion.

One should also note that $\langle e\vec{E} \rangle$ in Eq. (2.24) is defined at $\vec{x}^{(2)}$. By Taylor expanding \vec{E} about $\vec{x}^{(1)}$, one finds that $\langle e\vec{E} \rangle = -e\nabla_R\Upsilon$, where Υ is the nonlinear potential including the ponderomotive potential as it appears in the standard gyrokinetic theory [18] with $\vec{x}_{c2} = 0$ or in its modified version with polarization drift [17] with $\epsilon^2\vec{x}_{c2} = -\hat{b} \times \langle \vec{G} \rangle / \Omega$. In the latter case, the ponderomotive potential has an additional term $\epsilon^2\vec{x}_{c2} \cdot \langle (\partial\Phi/\partial\vec{x})(\vec{x}^{(1)}) \rangle$.

It is interesting to note that (2.20) with $\vec{P} = 0$ and $\vec{x} = \vec{x}^{(2)}$ reproduces the standard gyrokinetic result [27]. If one wishes to have the polarization drift in the perpendicular drift motion one chooses $\epsilon^2\vec{x}_{c2} = -(\epsilon/2\pi\omega^{(0)})\hat{b} \times \langle \vec{G}_\perp \rangle$ instead of $\vec{x}_{c2} = 0$.

The inverse Kruskal iteration with the Dirac's constrained Hamiltonian [28] and with the choice of the adiabatic invariant $J = \langle \vec{p} \cdot \partial\vec{x}/\partial\phi \rangle$ as one of the averaging coordinates in phase space presents suitable and transparent in obtaining gyrokinetic equations under different assumptions of gyrocentre coordinates. This includes the standard gyrokinetic formalism as well as its variation where the polarization drift is enclosed in the gyrocentre motion. The latter gives a gyrokinetic Poisson equation that reduces to a condition for particle-like charge densities with no explicit polarization term. It is directly solvable with particle simulation methods using direct sampling of particle density with gyroangle and field dependent gyroradius function. The required effort is in the iteration of the Euler equations for the particle position and velocity up to the desired order in gyrokinetic parameter that can be performed with the inverse Kruskal method.

The present formalism has been exploited in constructing the gyrokinetic full f particle code ELMFIRE [22]. Here, the free constant \vec{x}_{c2} was chosen to let the ion polarization drift to appear in the gyrocentre drift motion. The remaining trembling in the gyroradius (see Eq. (2.19))

$$\Delta\rho^{(2)} = \frac{\epsilon}{2\pi\omega^{(0)}}\hat{b} \times (\vec{G} - \langle \vec{G} \rangle) - \frac{\epsilon^2}{2\pi\omega^{(0)2}}\frac{e}{m}\hat{b} \times \int^\phi (\vec{E} - \langle \vec{E} \rangle) d\phi + \frac{\epsilon}{\omega^{(0)}} \int^\phi \vec{G}_\parallel d\phi \quad (2.26)$$

is taken into account directly in sampling the density from \vec{R} to \vec{r} with a ϕ -varying gyroradius $\rho^{(2)}$ in the gyrokinetic Poisson equation. This part of the charge density vanishes at long wavelength limit of perturbations, and can be modelled in an explicit sense for solving Φ over the time step.

In ELMFIRE, the polarization charge density is sampled directly from the polarization drift motion

$$\vec{V}_{Rp} = -(m/e) \left[\frac{\partial \langle \vec{G} \rangle}{\partial t} + \langle \vec{G} \rangle \cdot \frac{\partial \langle \vec{G} \rangle}{\partial \vec{R}} \right] \times \hat{b}/B$$

of the ion gyrocentres. This part consists also of long wavelength perturbations and is thus modelled in an implicit sense for solving Φ over the time step, i.e., the sample of this charge density is expressed in terms of the Φ at the end of the time step.

Alternatively, one could have set $\vec{x}_{c2} = 0$ as in the standard model and could have directly sampled charge densities and separately the coefficient matrix of the Poisson equation from the linear \vec{E} dependent tremblings of the particle gyroradii (including polarization effects), i.e., from Eq. (2.26) by setting $\langle \vec{G} \rangle = 0$ there. With this scheme as well as with the previous one, one may directly calculate the $\langle \vec{E} \rangle$ term in Eq. (2.24) without resorting to separate evaluation of the somewhat complex analytical expression of the ponderomotive force.

The procedures given above provide a viable simulation technique valid for wavelength range limited only by the simulation grid and by the accuracy of interpolation methods. The method is attractive as it readily allows introduction of either higher order or otherwise cumbersome additions of the gyrokinetic formalism to the numerical implementation. Here, one exploits the direct sampling of the particle density from \vec{R} to \vec{r} with a field and ϕ -varying gyroradius in the gyrokinetic Poisson equation either in an explicit or implicit sense, depending on its complexity. The standard way of introducing higher order differentials for this purpose may turn out to be impractical for numerical realization in more complex cases as with higher order corrections.

2.5 Magnetic and simulation geometry

The quasi-toroidal coordinate system (pictured in figure 2.5) maybe parametrized by

$$\begin{cases} x = (R_0 + r \cos \theta) \cos(\zeta) \\ y = (R_0 + r \cos \theta) \sin(\zeta) \\ z = -r \sin \theta, \end{cases} \quad (2.27)$$

and, if it is assumed that coordinates where the field equations given are the quasi-ballooning coordinates [35] which approximately follow the

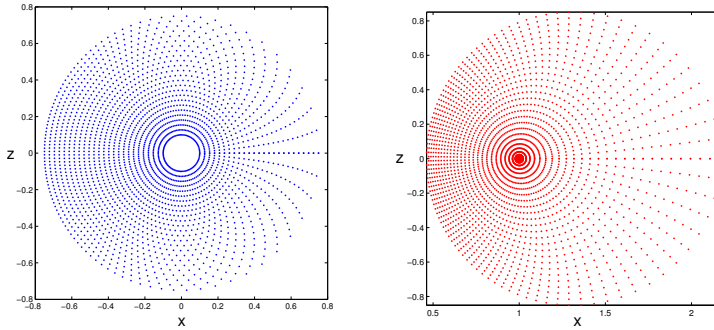


Figure 2.5. Exaggerated representation of the poloidal cross section of the quasitoroidal computational grid in the absence of rotational transform. The area elements are scaled to be of equal volume in the Boozer co-ordinates. On the right a corresponding toroidal co-ordinate system is shown.

magnetic field lines. This choice of coordinates relaxes computational effort by allowing long toroidal cells. The coordinate transformation from the quasitoroidal $(r, \theta(\vartheta_w), \zeta)$ coordinates to the magnetic field aligned (r, χ, ζ) coordinates (which follow the field lines) is given by

$$\chi = \theta_w - \iota(r)\zeta, \quad (2.28)$$

with $\iota = 1/q$. The co-ordinate ϑ_w is related to θ by

$$\vartheta_w = \frac{1}{\sqrt{1 - \varepsilon^2}} \arccos\left(\frac{\varepsilon + \cos \theta}{1 + \varepsilon \cos \theta}\right).$$

These are the coordinates used in ELMFIRE calculations for the fields.

The quasi-ballooning coordinates impose periodic conditions on physical quantities \aleph in the following manner:

$$\begin{cases} \aleph(r, \chi + 2\pi, \zeta) = \aleph(r, \chi, \zeta) \\ \aleph(r, \chi - 2\pi\iota(r), \zeta + 2\pi) = \aleph(r, \chi, \zeta). \end{cases} \quad (2.29)$$

There is another parametrization for the torus, named *toroidal coordinates* (pictured in figure 2.5) in the literature, parametrized by (u, v, φ) :

$$\begin{cases} x = \frac{a \sinh v \cos \varphi}{\cosh v - \cos u} \\ y = \frac{a \sinh v \sin \varphi}{\cosh v - \cos u} \\ z = \frac{a \sin u}{\cosh v - \cos u}, \end{cases} \quad (2.30)$$

which has the advantage of separable solutions for the Laplace equation.

Using the quasitoroidal Boozer coordinates (we shall return to these later) [37–39], we can express the magnetic field as

$$\vec{B} = g(\psi_p)\nabla\zeta + \mu_0 I(\psi_p)\nabla\theta_w + \delta(\psi_p, \theta_w)\nabla\psi_p, \quad (2.31)$$

where $g(\psi_p) = B_T R$, $2\pi I(\psi_p)$ the total current inside the magnetic surface as labeled by the poloidal magnetic flux $2\pi\psi_p$. Alternatively, the vector potential is $\vec{A} = \psi\nabla\theta_w - \psi_p\nabla\zeta$. In the following, we shall take $\delta \equiv 0$ [37]. Straight-field-lines in the (θ_w, ζ) -plane (poloidal-toroidal plane) are ensured by

$$q(\psi_p) = \frac{\vec{B} \cdot \nabla\zeta}{\vec{B} \cdot \nabla\theta_w} \quad (2.32)$$

with q as the *safety factor*. Note that because B is a function of poloidal angle ($1/R$ dependence), either ζ or θ_w angle must be nonuniform to make q constant on a flux surface. From the particle Lagrangian $L = mv^2/2 + q_e\vec{A} \cdot \vec{v} - q_e\phi$, one may derive (to first order in ρ/ℓ) the drift Lagrangian as

$$L_d = mv_{\parallel}^2 + q_e\vec{A} \cdot \vec{v}_{gc} + \mu B - H \quad (2.33)$$

where $H = mv_{\parallel}^2/2 + \mu B + q_e\phi$ is the lowest order drift Hamiltonian. We have from the chain rule $d\psi_p/dt = \dot{\psi}_p = \vec{v}_{gc} \cdot \nabla\psi_p$, $d\theta_w/dt = \dot{\theta}_w = \vec{v}_{gc} \cdot \nabla\theta_w$, $d\zeta/dt = \dot{\zeta} = \vec{v}_{gc} \cdot \nabla\zeta$ for the components of the guiding-center velocity. From $\vec{B} = g(\psi_p)\nabla\zeta + \mu_0 I(\psi_p)\nabla\theta_w$ one finds

$$v_{\parallel} = \vec{v}_{gc} \cdot \vec{B}/B = (g\dot{\zeta} + \mu_0 I\dot{\theta}_w)/B. \quad (2.34)$$

The drift-Lagrangian L_d can therefore be written as

$$\begin{aligned} L_d &= m\Omega\rho_{\parallel}(g\dot{\zeta} + \mu_0 I\dot{\theta}_w)/B + q_e(\psi_p\nabla\theta_w - \psi_p\nabla\zeta) \cdot \vec{v}_{gc} + \mu B - H \\ &= q_e\rho_{\parallel}(g\dot{\zeta} + \mu_0 I\dot{\theta}_w) + q_e\psi_p\dot{\theta}_w - q_e\psi_p\dot{\zeta} + \mu B - H \\ &\equiv P_{\theta_w}\dot{\theta}_w + P_{\zeta}\dot{\zeta} + \mu B - H, \end{aligned}$$

where $P_{\theta_w} = q_e(\mu_0 I\rho_{\parallel} + \psi_p)$ and $P_{\zeta} = q_e(g\rho_{\parallel} - \psi_p)$ are momenta canonical to θ_w and ζ . The drift-Hamiltonian is given by

$$H = \frac{q_e^2}{m}\rho_{\parallel}^2 B^2/2 + \mu B + e\phi. \quad (2.35)$$

The Hamiltonian equations of motion are given by

$$\begin{cases} \dot{P}_{\zeta} = -\partial H/\partial\zeta, & \dot{P}_{\theta_w} = -\partial H/\partial\theta_w, \\ \dot{\theta}_w = \partial H/\partial P_{\theta_w}, & \dot{\zeta} = \partial H/\partial P_{\zeta}. \end{cases} \quad (2.36)$$

Using the expressions for P_{θ_w} and P_{ζ} , one finds $q_e g\psi_p = gP_{\theta_w} - \mu_0 I P_{\zeta} - e\mu_0 I\psi_p$. Differentiation of this equation gives

$$d\psi_p = \frac{g dP_{\theta_w} - \mu_0 I dP_{\zeta}}{q_e D} \quad (2.37)$$

where $D = \rho_{\parallel}(g\mu_0 I' - g'\mu_0 I) + \mu_0 I + gq$ with the prime denoting derivation with respect to ψ_p . Therefore

$$\frac{\partial\psi_p}{\partial P_{\theta_w}} = \frac{g}{q_e D}, \quad \frac{\partial\psi_p}{\partial P_{\zeta}} = -\frac{\mu_0 I}{q_e D}. \quad (2.38)$$

From the expressions of P_θ and P_ζ , one finds

$$\begin{aligned} dP_\theta &= q_e(\mu_0 I' \rho_{\parallel} d\psi_p + \mu_0 I d\rho_{\parallel} + q d\psi_p) \\ dP_\zeta &= q_e(g' \rho_{\parallel} d\psi_p + g d\rho_{\parallel} - d\psi_p) \end{aligned}$$

Eliminating $d\psi_p$ gives

$$d\rho_{\parallel} = \frac{(\mu_0 I' \rho_{\parallel} + q)dP_\zeta - (g' \rho_{\parallel} - 1)dP_\theta}{q_e D} \quad (2.39)$$

from which follows

$$\frac{\partial \rho_{\parallel}}{\partial P_\theta} = \frac{1 - \rho_{\parallel} g'}{q_e D}, \quad \frac{\partial \rho_{\parallel}}{\partial P_\zeta} = \frac{q + \mu_0 I' \rho_{\parallel}}{q_e D}. \quad (2.40)$$

The particle guiding-centre equations can thus be written using the Hamilton's equations as

$$\begin{aligned} \dot{P}_\zeta &= -q_e \frac{\partial \phi}{\partial \zeta} - \left(\mu + \frac{q_e^2}{m} \rho_{\parallel}^2 B \right) \frac{\partial B}{\partial \zeta} \\ \dot{P}_\theta &= -q_e \frac{\partial \phi}{\partial \theta_w} - \left(\mu + \frac{q_e^2}{m} \rho_{\parallel}^2 B \right) \frac{\partial B}{\partial \theta_w} \\ \dot{\zeta} &= -\frac{\mu_0 I}{D} \frac{\partial \phi}{\partial \psi_p} - \left(\frac{\mu}{q_e} + \frac{q_e}{m} \rho_{\parallel}^2 B \right) \frac{\mu_0 I}{D} \frac{\partial B}{\partial \psi_p} + \frac{q_e \rho_{\parallel} B^2 (q + \rho_{\parallel} \mu_0 I')}{m D} \\ \dot{\theta}_w &= \frac{g}{D} \frac{\partial \phi}{\partial \psi_p} + \left(\frac{\mu}{q_e} + \frac{q_e}{m} \rho_{\parallel}^2 B \right) \frac{g}{D} \frac{\partial B}{\partial \psi_p} + \frac{q_e \rho_{\parallel} B^2 (1 - \rho_{\parallel} g')}{m D} \end{aligned}$$

The canonical momenta P_θ and P_ζ are not very useful in particle tracking. Instead, we wish to replace them with ψ_p and ρ_{\parallel} . Using the differentials of ψ_p and ρ_{\parallel} , we can solve for the relations of $\dot{\psi}_p$ and $\dot{\rho}_{\parallel}$ to \dot{P}_θ and \dot{P}_ζ which gives

$$\begin{aligned} \dot{\psi}_p &= \frac{\mu_0 I}{D} \frac{\partial \phi}{\partial \zeta} - \frac{g}{D} \frac{\partial \phi}{\partial \theta_w} + \left(\mu + \frac{q_e^2}{m} \rho_{\parallel}^2 B \right) \left[\frac{\mu_0 I}{q_e D} \frac{\partial B}{\partial \zeta} - \frac{g}{q_e D} \frac{\partial B}{\partial \theta_w} \right], \\ \dot{\rho}_{\parallel} &= -\frac{q + \rho_{\parallel} \mu_0 I'}{D} \frac{\partial \phi}{\partial \zeta} - \frac{1 - \rho_{\parallel} g'}{D} \frac{\partial \phi}{\partial \theta_w} \\ &\quad + \left(\mu + \frac{q_e^2}{m} \rho_{\parallel}^2 B \right) \left[\frac{q + \rho_{\parallel} \mu_0 I'}{q_e D} \frac{\partial B}{\partial \zeta} - \frac{1 - \rho_{\parallel} g'}{q_e D} \frac{\partial B}{\partial \theta_w} \right], \end{aligned} \quad (2.41)$$

which are used in ELMFIRE simulations for particle pushing, with the distinction that the gyroaveraged electric field is used, making these equations equivalent to Eq. (2.9) and (2.23). The particles also experience collisions through a stochastic operator and polarization motion which is implicitly solved and applied after explicit particle pushing.

The co-centric circles approximation (currently used in ELMFIRE) for the geometry has flux surfaces coincident with the quasitoroidal (r, ζ) . The functions $I(r)$, $q(r)$, $g(r)$, $J(r, \theta)$, and the magnetic coordinates ψ_p , θ_w , ζ related analytically by

$$\begin{aligned} 2\pi \mu_0 I &= B_p R \epsilon \kappa, & 2\pi q &= g \epsilon \kappa / B_p R, & 2\pi J &= \epsilon \kappa R / B_p, \\ \psi_p &= \int_0^r B_p R dr, & \theta_w &= (2\pi / \kappa) \int_0^\varphi d\varphi / (1 + \epsilon \cos \varphi), & \zeta &= \phi, \end{aligned}$$

using $\epsilon = r/R$, and $\kappa(\epsilon) = \int_0^{2\pi} d\varphi/(1 + \epsilon\cos\varphi)$. Here we have also, $\vec{B} = B_T\hat{\phi} + B_p\hat{\phi}$, $g = B_T R$ is constant in space, and $B_p R$ is a function of only r .

3. Linear growth rate analyses

Nothing happens until
something moves.

Albert Einstein

Instability in a system is apparent, when the system is in static equilibrium (i.e., sum of forces and moments are zero), but dynamically tends to move away from it. Such a case may be easily illustrated by the example of a pen balanced on its tip; statically all forces are balanced and the system is in equilibrium, but when time is allowed to start, the pen tips over and finds a dynamical equilibrium. In this crude illustration of instability we have all the basic elements present: a small perturbation is needed to get the pen going, the tilt of the pen grows, and after a short while, the pen finds equilibrium on its side at the table having dissipated the free energy available to it through deformation, waves and heat.

3.1 Linear growth of drift instability

Generally the problems of flows in fluids are highly non-linear. Such problems may be generally represented as a system of ordinary differential equations

$$\begin{aligned}\frac{d\mathbf{X}}{dt} &= f(\mathbf{X}) \\ \mathbf{X}(t=0) &= \mathbf{a}(\mathbf{x}),\end{aligned}\tag{3.1}$$

where $\mathbf{a}(\mathbf{x})$ is an initial state, $\mathbf{X}(\mathbf{x})$ is the state variable dependent on coordinates \mathbf{x} , and f is a (generally non-linear) function on the state variable and t is time. The issue of linear growth of unstable modes presents itself when the non-linear equations are linearized about the fixed point (i.e., the initial state) $f(\mathbf{a}) = \mathbf{0}$. Linearisation of Eq. (3.1) about a fixed point

yields the linear problem

$$\begin{aligned}\frac{d\mathbf{X}}{dt} &= \mathbf{A}(\mathbf{X} - \mathbf{a}) = \mathbf{A}\delta\mathbf{X} \\ \mathbf{X}(t=0) &= \mathbf{a},\end{aligned}\tag{3.2}$$

with $\mathbf{A} = (\partial_{\mathbf{x}}f)(\mathbf{a})$, which has the formal solution $\delta\mathbf{X}(t) = \delta\mathbf{X}(t=0) \exp \mathbf{A}t$. The solution to the linear differential system of Eq. (3.2) is called the *linear solution*. As a result, we may find decaying or growing solutions which generally have time-dependent oscillations if \mathbf{A} has complex eigenvalues. Through Fourier-analysis, the problem can be expressed as an algebraic problem in (\mathbf{k}, ω) -space. Because here only stability is of concern, we may illustrate this with a single complex eigenvalue of \mathbf{A} by writing out an “atomic” solution

$$\delta x_k(t) = \delta x_k(t=0) \exp i(\mathbf{k} \cdot \mathbf{x} - \omega t)\tag{3.3}$$

where ω is a complex eigenvalue and \mathbf{k} is the wave vector (related to coordinates \mathbf{x}). If we write $\omega = \omega_r + i\gamma$, we find unstable (exponentially growing) solutions when $\gamma > 0$. We will call ω_r frequency and absolute value of γ the growth rate of a linear eigenmode, with the complex ω as the eigenvalue. In principle, it is possible to have constant driving terms in Eq. (3.1) which do not appear in the linearised problem, but here only exponentially growing instabilities (which eventually dominate) are of interest. One of the classical examples of such an analysis is the *Rayleigh-Taylor* instability, where fluid layers (e.g., water on oil) interchange due to gravitation. In the tokamak plasma the analogous driving force is inhomogeneity of the magnetic field. The existence of non-linearly driven instabilities (such as the parametric instability of zonal flow) is noteworthy, as this analysis utterly neglects them.

As an example of linear instability analysis we present the derivation of the reactive fluid model introduced by B. Coppi and utilized by J. Weiland [40] for quasilinear scaling of turbulent transport. The model is based on the Braginskii closure obtained by expanding the kinetic theory on an orthogonal basis (Sonine polynomials) and deriving first-order corrections [41]. This model is used in analysis of experiments using transport codes (such as JINTRAC), amongst other theoretical and experimental scalings. In the following treatment, we follow the procedure of Weiland to find growth rates and frequencies for the Ion Temperature Gradient (ITG) and Trapped Electron Mode (TEM) branch of drift insta-

bility. The MHD equations are given by

$$\frac{\partial n_a}{\partial t} + \vec{\nabla} \cdot (n_a \vec{v}_a) = 0, \quad (3.4)$$

$$\frac{\partial \vec{v}_a}{\partial t} + \vec{v}_a \cdot \vec{\nabla} \vec{v}_a = \frac{q_a}{m_a} \left(\vec{E} + \vec{v}_a \times \vec{B} \right) - \frac{1}{m_a n_a} \left(\vec{\nabla} p_a + \vec{\nabla} \cdot \boldsymbol{\pi}_a \right), \quad (3.5)$$

$$\frac{3}{2} n_a \left(\frac{\partial}{\partial t} + \vec{v}_a \cdot \vec{\nabla} \right) T_a + p_a \vec{\nabla} \cdot \vec{v}_a = -\vec{\nabla} \cdot \vec{q}_a, \quad (3.6)$$

$$\frac{dp_a}{dt} - \gamma p \vec{\nabla} \cdot \vec{v}_a = 0 \quad (3.7)$$

where n_a is the density of particle species a and v_a its fluid velocity, $\vec{E} = -\vec{\nabla} \phi$ is the electric field and ϕ is the electric potential, p_a is the scalar pressure, $\boldsymbol{\pi}_a$ is the viscosity tensor (the non-spherical part of the pressure tensor), and \vec{q}_a is the heat flux. The continuity equation is stated in Eq. (3.4) (which can also be used to derive charge conservation), Eq. (3.5) is the fluid momentum conservation equation, and Eq. (3.6) is the equation for energy conservation (also called the Braginskii energy equation). We also assume that the compression associated with perturbations is adiabatic (Eq. (3.7)), an assumption which holds for rapid processes. We use $\gamma = \frac{d+2}{d} = \frac{5}{3}$, because the system is essentially three dimensional (parallel and perpendicular pressures are not discriminated).

The Braginskii closure to the fluid hierarchy is attained by assuming that the heat flux is diamagnetic,

$$\vec{q}_a \approx \vec{q}_{*a} = \frac{5}{2} \frac{p_a}{m_a \Omega_a} \hat{b} \times \vec{\nabla} T_a, \quad (3.8)$$

which gives us

$$\vec{\nabla} \cdot \vec{q}_a = \vec{\nabla} \cdot \vec{q}_{*a} = -\frac{5}{2} n_a \vec{v}_{*a} \cdot \vec{\nabla} T_a + \frac{5}{2} n_a \vec{v}_{Da} \cdot \vec{\nabla} T_a. \quad (3.9)$$

The magnetization flow is discussed in more depth in Ref. [6].

We also assume that the fluid velocity \vec{v}_a is given by the second order iterative solution to the momentum equation (3.5),

$$\vec{v}_a = \vec{v}_{*a} + \vec{v}_{Ea} + \vec{v}_{\pi a} + \vec{v}_{pa}, \quad (3.10)$$

$$\vec{v}_{*a} = \frac{\hat{b} \times \vec{\nabla} p_a}{n_a m_a \Omega_a}, \quad (3.11)$$

$$\vec{v}_{Ea} = \frac{\vec{E} \times \hat{b}}{B}, \quad (3.12)$$

$$\vec{v}_{\pi a} = \frac{\hat{b} \times \vec{\nabla} \cdot \boldsymbol{\pi}_a}{n_a m_a \Omega_a}, \quad (3.13)$$

$$\vec{v}_{pa} = \frac{1}{\Omega_a} \frac{d(\hat{b} \times \vec{v}_a)}{dt} \approx \frac{1}{\Omega_a B} \frac{d\vec{E}}{dt}, \quad (3.14)$$

where \vec{v}_{*a} is the diamagnetic drift, \vec{v}_{Ea} is the $E \times B$ -drift, $\vec{v}_{\pi a}$ is the viscosity drift and \vec{v}_{pa} is the polarisation drift velocity, with $\frac{d}{dt} = \frac{\partial}{\partial t} + \vec{v}_a \cdot \vec{\nabla}$ as the

convective derivative, and the \vec{v}_{Ea} is used as the dominating fluid velocity in the polarization velocity.

It is important to note, that the velocities given above do not include the gradient and curvature drifts, which are present in the kinetic treatment. They do arise in the fluid treatment as well if we allow the magnetic field to have inhomogeneity, which gives us an analogous drift

$$\vec{v}_{Da} = \frac{T_a}{m_a \Omega_a} \hat{b} \times \left(\hat{b} \cdot \vec{\nabla} \hat{b} + \vec{\nabla} \ln B \right), \quad (3.15)$$

but this velocity does not appear unless the true fluid velocities (v_{*a} , v_{Ea} , and so on) are operated upon, like in the flux divergence term of the continuity equation. They therefore represent compressibility of the flux.

We will frequently use $\vec{\nabla} \cdot (n_a \vec{v}_a)$ and $\vec{\nabla} \cdot \vec{v}_a$, so it is useful to state them explicitly:

$$\vec{\nabla} \cdot (n_a \vec{v}_{Ea}) = \frac{q_a}{T_a} \vec{v}_{Da} \cdot \vec{\nabla} \phi + \vec{v}_{Ea} \cdot \vec{\nabla} n_a \quad (3.16)$$

$$\vec{\nabla} \cdot (n_a \vec{v}_{*a}) = \frac{1}{T_a} \vec{v}_{Da} \cdot \vec{\nabla} p_a \quad (3.17)$$

$$\vec{\nabla} \cdot [n_a (\vec{v}_{pa} + \vec{v}_{\pi a})] = \vec{\nabla} \cdot \left[\frac{n_a}{\Omega_a} \frac{\partial (\hat{b} \times \vec{v}_a)}{\partial t} \right]. \quad (3.18)$$

We may write (remember that $\hat{b} \times \vec{\nabla} p \cdot \vec{\nabla} p = 0$)

$$\frac{3}{2} n_a \vec{v}_{*a} \cdot \vec{\nabla} T_a - T_a \vec{v}_{*a} \cdot \vec{\nabla} n_a = \frac{5}{2} n_a \vec{v}_{*a} \cdot \vec{\nabla} T_a, \quad (3.19)$$

which conveniently cancels with the diamagnetic part of the heat flux of Eq. (3.9) in Eq. (3.6). Let us write $\omega_{*a} = \vec{v}_{*a} \cdot \vec{k}$, $\omega_{Da} = \vec{v}_{Da} \cdot \vec{k}$, where \vec{k} is the wave vector. With $\vec{v} = \vec{v}_{Ea} + \vec{v}_{*a}$ we may manipulate the energy equation to

$$\frac{1}{T_a} \frac{\partial T_a}{\partial t} + \frac{1}{T} \vec{v}_{Ea} \cdot \vec{\nabla} T_a - \frac{2}{3} \frac{1}{n_a} \vec{v}_{Ea} \cdot \vec{\nabla} n_a + \frac{5}{3} \frac{1}{T_a} \vec{v}_{Da} \cdot \vec{\nabla} T_a - \frac{1}{n_a} \frac{\partial n_a}{\partial t} = 0. \quad (3.20)$$

Now, let us linearize the system by assuming $T = T_0 + \delta T$, $n = n_0 + \delta n$, ϕ is the perturbed potential, and Fourier analyze the problem ($\vec{\nabla} \rightarrow i\vec{k}$, $\partial/\partial t \rightarrow -i\omega$), which gives us the linearised temperature perturbation for the ions (the electrons are treated in similar manner):

$$\frac{\delta T_i}{T_i} = \frac{\omega}{\omega - \frac{5}{3} \omega_{Di}} \left(\frac{\delta n_i}{n_i} + \frac{\omega_{*e}}{\omega} \left(\eta_i - \frac{2}{3} \right) \frac{e\phi}{T_e} \right), \quad (3.21)$$

where $\eta_i = \frac{L_{ni}}{L_{Ti}}$ for the ions, and $L_{Ti} = |\nabla \log T_i|^{-1}$ and $L_{ni} = |\nabla \log n_i|^{-1}$ are the temperature and density scale lengths (for the ions), respectively. Now, from the continuity equation with $\vec{v}_i = \vec{v}_{*i} + \vec{v}_{Ei} + \vec{v}_{\pi i} + \vec{v}_{pi}$ we obtain

$$\frac{\partial n_i}{\partial t} + \frac{1}{T_i} \vec{v}_{Di} \cdot \vec{\nabla} p_i + \frac{q_i n_i}{T_i} \vec{v}_{Di} \cdot \vec{\nabla} \phi + \vec{v}_{Ei} \cdot \vec{\nabla} n_i + \vec{\nabla} \cdot [n_i (v_{pi} + v_{\pi i})] = 0, \quad (3.22)$$

which through similar Fourier analysis, with the aid of $\vec{\nabla} \cdot [n_i(v_{pi} + v_{\pi i})] = ink^2 \rho_s^2 (\omega - \omega_{*i}) \frac{e\phi}{T_e}$ ($\rho_s = \frac{c_s}{\Omega_i}$, and $c_s = \sqrt{T_e/m_i}$ is the sound velocity) and linearization gives

$$\frac{\delta n_i}{n_i} = \left[\omega (\omega_{*e} - \omega_{De}) + \left(\eta_i - \frac{7}{3} + \frac{5}{3} \varepsilon_n \right) \omega_{*e} \omega_{Di} - k^2 \rho_s^2 (\omega - \omega_{*iT}) \left(\omega - \frac{5}{3} \omega_{Di} \right) \right] \times \left[\omega^2 - \frac{10}{3} \omega \omega_{Di} + \frac{5}{3} \omega_{Di}^2 \right]^{-1} \frac{e\phi}{T_e}, \quad (3.23)$$

where $\varepsilon_n = \frac{2L_n}{L_B}$, $L_B = \frac{B}{|\nabla B|}$ is the magnetic field gradient scale length, and $\omega_{*iT} = \omega_{*i}(1 + \eta_i)$. The procedure is in no way limited to the ions, so for the trapped electrons we obtain a similar expression, except that ρ_s is assumed to be zero for electrons (their Larmor radii are negligible). By quasi-neutrality $\delta n_i = \delta n_e$ and writing the electron density perturbation as an adiabatic part $\delta n_e/n_e = e\phi/T_e$ (for the free electrons) and the trapped part (with $f_t = \sqrt{\varepsilon}$ as the trapped fraction, ε is the inverse aspect ratio), we obtain the dispersion relation

$$\begin{aligned} & \frac{\omega_{*e}}{N_i} \left[\omega(1 - \varepsilon_n) + \left(\eta_i - \frac{7}{3} + \frac{5}{3} \varepsilon_n \right) \omega_{Di} \right. \\ & \quad \left. - k^2 \rho_s^2 [\omega - \omega_{*i}(1 + \eta_i)] \left(\frac{\omega}{\omega_{*e}} + \frac{5}{3\tau} \varepsilon_n \right) \right] \\ & = f_t \frac{\omega_{*e}}{N_e} \left[\omega(1 - \varepsilon_n) + \left(\eta_e - \frac{7}{3} + \frac{5}{3} \varepsilon_n \right) \omega_{De} \right] + 1 - f_t, \end{aligned} \quad (3.24)$$

where we have introduced $\tau = T_e/T_i$, $\eta_e = L_{ne}/L_{Te}$ (produced in the same manner as for the ions) and

$$N_j = \omega^2 - \frac{10}{3} \omega \omega_{Dj} + \frac{5}{3} \omega_{Dj}^2, \quad j \in \{e, i\}. \quad (3.25)$$

The mode can be classified by examining $N_i - N_e < 0$: if the inequality is true, the mode is the ion temperature gradient mode, otherwise it is the trapped electron mode. They travel in different directions, TEM travels along ω_{*e} whereas ITG travels along ω_{*i} , which are opposite. The poloidal wave vector in a tokamak may be written as $k = m/r$, where m is the mode number.

As we can see, the dispersion relation given by Eq. (3.24) is a quartic polynomial, which is cumbersome (but possible) to solve by hand. Because all the coefficients are real there may only be even numbers of complex solutions, which are complex conjugates of each other, $\omega = \omega_r \pm i\gamma$. While this fact does not simplify solving the problem, it implies two important things. First, any solution with a negative imaginary part has a conjugate pair, so finding such a root implies that there is an unstable solution with

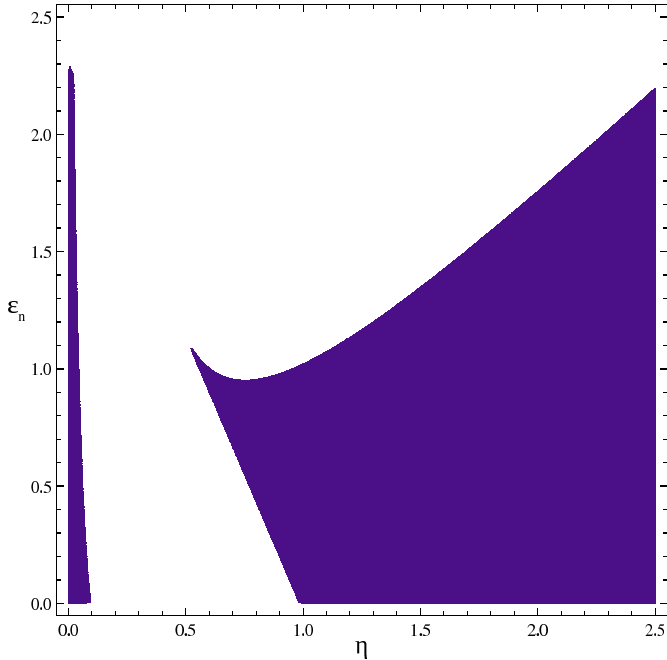


Figure 3.1. Stability diagram for the FT-2 machine parameters obtained by solving the dispersion relation 3.24 with Mathematica for different values of η and ϵ_n . The coloured area is unstable. Here $\tau = 2$ and $I_{\text{tot}} = 18.9$ kA.

equal absolute values. Because all roots may be complex, we have the possibility of two different unstable modes simultaneously in the plasma, which may be ITG and/or TEM. The dispersion relation is easily solved using symbolic analysis software such as Mathematica (as illustrated by figure 3.1) or by solving the eigenvalue problem of the Frobenius companion matrix numerically. The growth rates and frequencies may then be used to calculate quasilinear transport rates for particles and heat.

The linearised fluid equations presented above do capture some of the physics associated with ITG/TEM branch of drift modes, however the model predicts excessively high mode growth rates when k_{\perp} is chosen to be at the maximal growth rate (with respect to GS2 [42]). Weiland chooses $k_{\perp}\rho$ well below the maximum, with $k_{\perp}^2\rho^2$ of 0.05 to 0.1 depending on the reference. With this caveat, we take this model and use it as an order-of-magnitude estimate for simulation parameters. We have solved the dispersion relation for the ‘‘Cyclone base case’’ [12] parameters of section 3.2, over $k_{\perp}\rho_s \in [0, 2]$. In figure 3.2 we plot the unstable modes found in this region for an adiabatic electron case with $f_t = 0$ and $\eta_e = 0$, and a kinetic electron case with $\eta_e = 0$ but non-zero f_t . These cases have also been

used in ELMFIRE simulations of drift wave turbulence in benchmarking, with mode growth rate and frequency spectra used as an aid in selecting suitable simulation parameters (e.g., timestep) for benchmarking the ELMFIRE, in addition to numerical stability and implicit dissipation conditions.

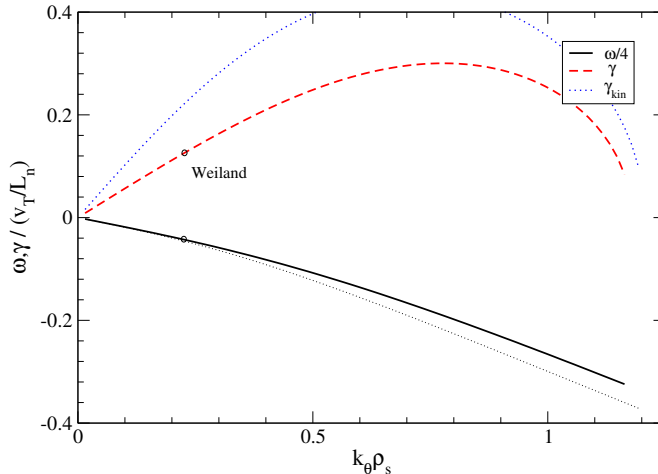


Figure 3.2. Growth rates and frequencies of the ITG/TEM drift instabilities with the “Cyclone base case” parameters, taking the trapping fraction $f_t = 0$ and $\eta_e = 0$. We interpret from Ref. [35] that the Weiland points correspond to the values highlighted with circles. Growth rate for trapped electron fraction of $f_t = \sqrt{2\epsilon/(1+\epsilon)}$ is enhanced. Compare with figure 3.9.

According to Eq. (3.3) we may find a growing solution in an “experimental” context (e.g., ELMFIRE simulation) by examining the time series of the eigenmode expansion of the physical quantity, be it density or the potential. However, it is important to note that in general the eigenmodes in a complex geometry are not pure toroidal Fourier modes, but instead a more complex structure (called a ballooning structure) which involves a set of Fourier modes. Nevertheless, we may express a perturbation in the form

$$\phi(r, \vartheta, \zeta) = \sum_{m,n} \phi_{m,n}(r) e^{i(m\vartheta+n\zeta)}. \quad (3.26)$$

when (r, ϑ, ζ) are taken as coordinates on the parametric torus (see Sec. 2.5).

As a matter of convenience, the reader is directed to read Ref. [35] where the Fourier analysis technique is outlined. However, this coordinate transformation which had been made for simplifying the numerical solution of the gyrokinetic Poisson equation complicates Fourier-analysis, because the (m, n) modes populate only the region near $m\mu \approx n$.

The dynamics of a typical growing (m, n) mode is shown in Fig. 3.3.

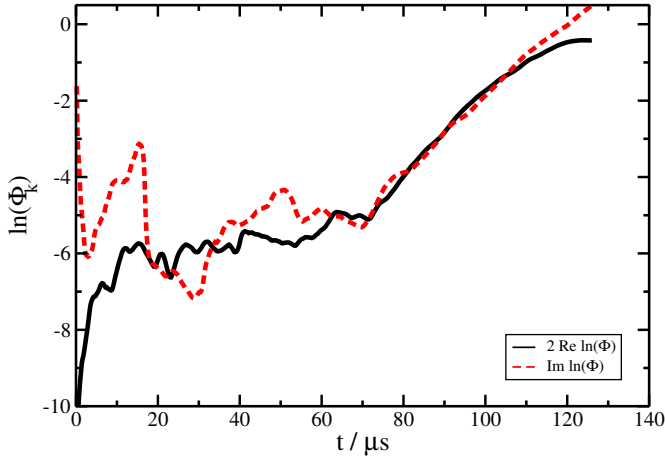


Figure 3.3. The complex logarithm of a Fourier mode in an ELMFIRE simulation for the adiabatic Cyclone Base case.

There is a waiting period in the simulation as the modes phase themselves, and a growth period is observed for the amplitude and the phase after the seed fluctuations have set in. The complex logarithm of the Fourier coefficient for the mode exhibits linear behavior, and when the mode amplitude reaches sufficient values the growth is inhibited. In this case the spanning Fourier spectrum has been restricted to improve signal-noise ratio by including only a specified n -mode in the charge separation.

3.2 The “Cyclone Base” case, with variations

The “Cyclone base” case parameters were given as dimensionless quantities, such as R/L_T , R/L_n , $\eta_i = L_n/L_T$, $\tau = T_e/T_i$, a/R , q and \hat{s} , where the temperature and density scale lengths are given by $L_T^{-1} = |\nabla \ln T|$ and $L_n^{-1} = |\nabla \ln n|$, respectively, R is the major radius and a is the minor radius, $\hat{s} = \frac{r}{q} \frac{dq}{dr}$ is the magnetic shear, q is the magnetic safety factor and ν is the collisionality. The results were given also in dimensionless quantities. While this method avoids confusion with units, it also leaves the freedom of scaling R , a , T_i and n_i in a consistent manner (see table 3.1). Also, different authors appear to use different ion species and ion-electron mass ratios for their results in the literature, while others do not specify these at all.

This has resulted in several different versions of the same parameter set for which the ELMFIRE is run: the scaled Cyclone parameters used in

the adiabatic linear analyses, and differently scaled parameters used in kinetic non-linear runs. The Integrated Tokamak Modelling Task Force (TF-ITM) IMP#4 project has defined the parameters in a dimensional form, and also these differ from original ELMFIRE Cyclone tests.

Table 3.1. Initial parameters for the ‘‘Cyclone base case’’ test cases with adiabatic and kinetic electrons. These parameters were chosen to satisfy the normalized values.

$R/L_T = 6.9$	$R/L_n = 2.2$	$R/a = 2.78$	$r_0/a = 0.5$	$\hat{s} = 0.78$
$q(r_0) = 1.42$	$R = 0.55 \text{ m}$	$T_i = 100 \text{ eV}$	$n_i = 0.5 \cdot 10^{18} \text{ m}^{-3}$	

In the linear and kinetic non-linear comparative tests we adopt the so-called ‘‘Cyclone DIII-D base case’’ dimensionless parameters [12] with hydrogen ions, a widely used test case described in Table 3.1. Correspondingly, initial density and temperature radial profiles are given as $n_0[1 + \alpha_n \tanh \frac{r_0-r}{\alpha_n L_n}]$, $T_0[1 + \alpha_T \tanh \frac{r_0-r}{\alpha_T L_T}]$ with $\alpha_n = \alpha_T = 0.95$, $r_0 = (r_L + r_R)/2$, $n_0 = 5 \cdot 10^{19} \text{ m}^{-3}$, $T_0 = 100 \text{ eV}$, for the analysis of the Cyclone base case in the adiabatic case. In the kinetic electron case we use an initial density $n_0 = 5 \cdot 10^{17} \text{ m}^{-3}$ and $\alpha_n = \alpha_T = 0.9$. For the linear analysis, the inner and outer radii of the simulation region are $r_L = 0.16 \text{ m}$, $r_R = 0.24 \text{ m}$ with $a = 0.3975 \text{ m}$ as the minor radius. The plasma current density profile is taken as $j = j_0(1 - r^2/a^2)^{\alpha_I}$ with $j_0 = I_0(1 + \alpha_I)/\pi a^2$ giving the maximum current density in terms of the total plasma current I_0 and minor radius a . In the following, we have $\alpha_I = 3.0$, $B_T = 1.1 \text{ T}$, $R = 1.1 \text{ m}$, and $I_0 = 200 \text{ kA}$. At $r = r_0$, $\rho_i/a = 0.0023$. These parameters give the same normalized parameters locally at r_0 .

For the kinetic transport simulations, we have chosen the scaled set of ‘‘Cyclone base’’ parameters. It is important to note, however, that these parameters were not used for the adiabatic non-linear evaluations, which were performed much later under the EFDA TF-ITM framework.

The electron model used in adiabatic simulations assumes Boltzmann-distributed electrons, whose response to an electric potential Φ is taken as

$$n_e = \langle n_i \rangle + \delta n_e = \langle n_i \rangle e^{\frac{e(\Phi - \langle \Phi \rangle)}{T_e}} \approx \langle n_i \rangle \left(1 + \frac{e(\Phi - \langle \Phi \rangle)}{T_e} \right), \quad (3.27)$$

where $\langle n_i \rangle$ and $\langle \Phi \rangle$ are the flux surface averages of the simulated ion density and potential. This model allows for the ion temperature gradient instability, but not any instabilities associated with electron motion such as trapped electron modes or electron temperature gradient modes.

3.2.1 TF-ITM Cyclone parameters

Currently the most important part of IMP #4 is the cross verification process. In 2006 the ‘‘Cyclone base’’ case was chosen for this task while the problems associated with it are recognised. In the literature for non-linear transport analyses dimensionless parameters are given, which could be referenced to. However, the ITM background parameters were set in terms of absolute values and profiles: $T_e = T_i = 2\text{keV}$, $B = 1.91\text{T}$, $L_T = 0.246\text{m}$, $a = 0.625\text{m}$, $R_0 = 170\text{cm}$, $L_T/L_n = 0.321$, $q = 1.4$, $\hat{s} = 0.78$. Hence, for example, the local value of ρ^*/L_T is 0.0138 or about 1/73, while the global value of a/ρ^* is 184.7.

Table 3.2. Initial parameters for the ITM#4 ‘‘Cyclone base case’’ test cases.

$R/L_T = 6.9$	$R/L_n = 2.2$	$R/a = 2.78$	$r_0/a = 0.5$	$\hat{s} = 0.78$
$q(r_0) = 1.42$	$R = 1.7\text{ m}$	$T_i = 2000\text{ eV}$	$n_i = 0.45 \cdot 10^{19}\text{ m}^{-3}$	

The model geometry is concentric circular. The outer third quarter is $0.5 < r/a < 0.75$. The q profile is a parabolic one satisfying the local parameters: $q = 0.854 + 2.184(r/a)^2$.

Model density and temperature profiles are prescribed in terms of their gradients,

$$\begin{aligned} R\nabla T_i &= 2\text{ keV} \times R/L_T \times p(r) \\ R\nabla n_i &= 4.5 \cdot 10^{19}\text{ m}^{-3} \times R/L_n \times p(r) \\ R\nabla T_e &= R\nabla T_i \\ R\nabla n_e &= R\nabla n_i \end{aligned}$$

where

$$p(r) = -1 + \text{sech}^2\left(\frac{r-r_l}{\delta a}\right) + \text{sech}^2\left(\frac{r-r_r}{\delta a}\right) \quad (3.28)$$

$$\int p(r) dr = -r + \delta a \left(\tanh\left(\frac{r-r_l}{\delta a}\right) + \tanh\left(\frac{r-r_r}{\delta a}\right) \right) \quad (3.29)$$

is a normalised profile with boundary buffer zones δa . The boundary layer may be left out in the ELMFIRE simulations, because density gradients near the boundary reduce χ_i estimate values, and make plots made while running the case more meaningful. For global codes it is important to remember that scale lengths are functions of temperature, and as such, results in the profiles of the following form (analogously for density):

$$T(r) = 2\text{ keV} \exp \frac{1}{L_T} \left(a/2 - r + \delta a \left(\tanh\left(\frac{r-r_l}{\delta a}\right) + \tanh\left(\frac{r-r_r}{\delta a}\right) \right) \right), \quad (3.30)$$

which ensures that the L_T is constant over simulation region, which is needed for comparisons with the flux-tube codes. Adiabatic electrons with density scaling factor taken from initial quasi-neutrality (when $\phi = 0$) was chosen.

3.3 Adiabatic linear growth

Up to recently, very few codes in addition to ELMFIRE had a working kinetic electron model (especially in non-linear simulations). The adiabatic model was developed to ELMFIRE some time after the kinetic electrons were developed, but because mostly all published benchmarking data was for adiabatic electrons, it had to be used. The adiabatic model is given in equation 2.16.

The standard ‘‘Cyclone base’’ case is an adiabatic electron case with a hyperbolic tangential density and temperature profile given by $n, T \propto 1 + \alpha \tanh((r_{\text{ref}} - r)/(\alpha L))$, where L is the gradient scale length and $\alpha = 0.05$ is a boundary factor that is chosen so that values near boundaries are finite. The maximal temperature and density gradients are chosen at $r_{\text{ref}}/a = 0.5$, where the mode growth spectrum is investigated. In essence, the ELMFIRE was rendered a linear stability code for this purpose. While not developed as such, linear stability calculation of modes is an important benchmark for the code to pass as a tool for non-linear simulations.

The development of linear growth profiles as shown in Publication I figure 3 was not a simple procedure in terms of running the ELMFIRE and analysis methods used, because at the time computational resources were very limited. The DIII-D experiment is a mid-range tokamak, and as such has a relatively low $\rho_* = \rho_s/a \approx 1/184$. The resolution needed for simulating an experiment scales roughly as ρ_*^{-2} , and a high resolution entails using high numbers of particles for acceptable noise levels. Also, the initialisation procedure was found to contaminate the signal by introducing a high initial perturbation, which limited the region of acceptable linear growth. It is important to realise that the particular Fourier transform used in this context is not the traditional one, but a variation where m numbers are independent but n modes have a phase shift which is linearly dependent upon m .

The particle noise could have been suppressed by using sufficient number of particles per mode, but limiting the number of modes was computationally more attractive because the noise spectrum is broadband and

scales as $1/\sqrt{N}$ with N particles. As the discretisation of the field equations needs to be sufficiently refined, the resolution may not be restricted in this way. Particle noise may be reduced by using Fourier filtering (later used by others, see for example Ref. [43]) for a specific toroidal n -mode, allowing only the corresponding band of m -modes to grow. Distribution function initialization has to be done carefully when performing such investigations on the ELMFIRE, as shown in section 5.2. A local Maxwellian was chosen for the adiabatic linear growth rate analyses. In this initialization, all modes are absent in the beginning and the logarithm of the amplitude starts from $-\infty$.

Very quickly it was observed that changing the poloidal resolution would affect the growth rates of the modes, although the system should be well resolved. This can be seen very clearly in Fig. 3.4 where we see an increase of the growth rate of the (30, 21) mode as a function of the maximal poloidal resolution (with $m = dNY/2$), until a sufficient resolution is attained.

The linear growth rate spectrum given in Publication I Fig. 3 has been obtained by using local Maxwellian initialization, and by keeping only one n -mode in each point with $k_\theta \rho_s = \frac{qm}{r} \rho_s$. The nominal simulation parameters for the adiabatic linear growth rate analyses are given in Table 3.3, where dNX , dNY and dNZ are the number of radial, poloidal and toroidal grid points in the quasi-ballooning co-ordinates, respectively, and Δt is the time step. Particle numbers were varied between $N_{\text{part}} = (9 - 23) \cdot 10^6$ by increasing the number of pitch values in the initial distribution to keep the particle number per cell constant for similar noise characteristics in the simulations.

Table 3.3. Simulation parameters used for the adiabatic linear Cyclone test cases.

$dNX = 25 - 31$	$dNY = 150 - 500$	$dNZ = 4 - 16$	$\Delta t = 2 \cdot 10^{-7} \text{ s}$
-----------------	-------------------	----------------	--

In figure 3.5 we show the typical m -structure for $\{\phi_k^2\}_\Omega$ for the logarithm of the mode energy (in arbitrary units) as a function time. As can be seen, most of the mode energy is associated with the resonant mode at $q = 10/7$ at radius $r/a = 0.5$. This means that effectively the total energy associated with an n mode can be used for evaluating the growth rate. This is not the case for mode phases, however, and therefore only the resonant mode was used for calculating the phase velocity.

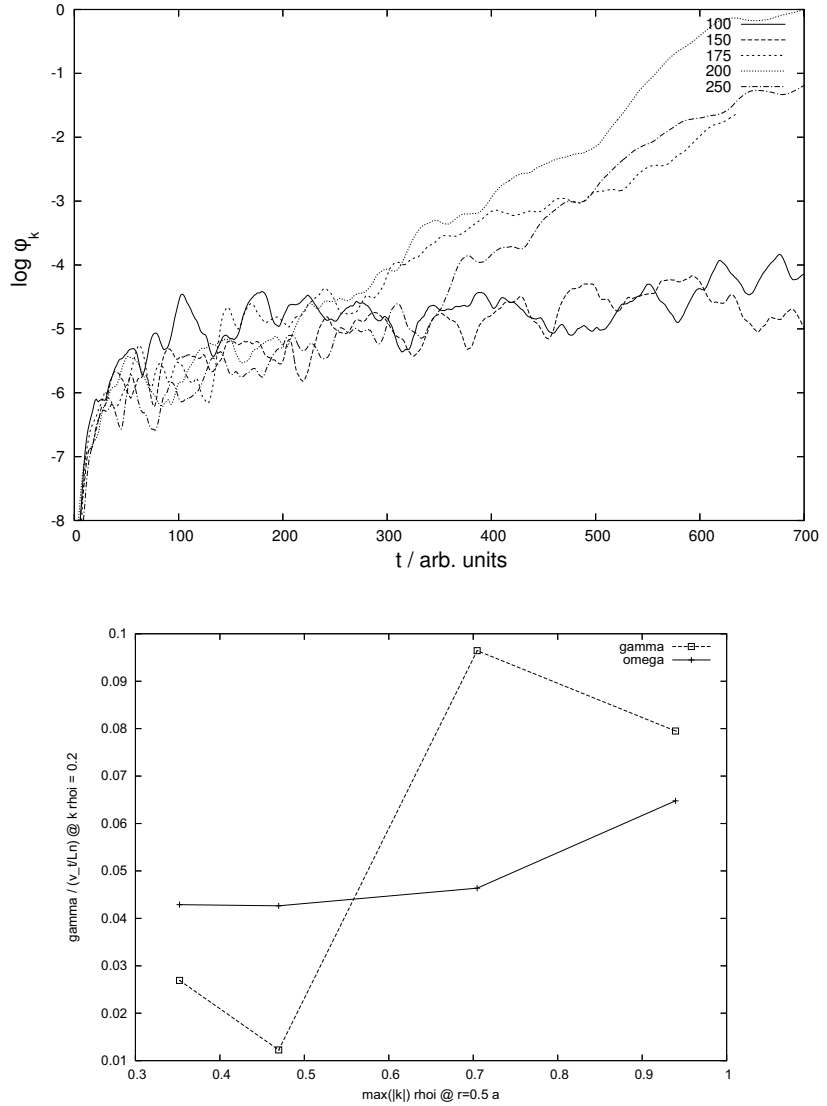


Figure 3.4. Linear growths for different poloidal grid values. We give the logarithm of energy in arbitrary units as a function of time steps taken. There is a threshold value for resolution.

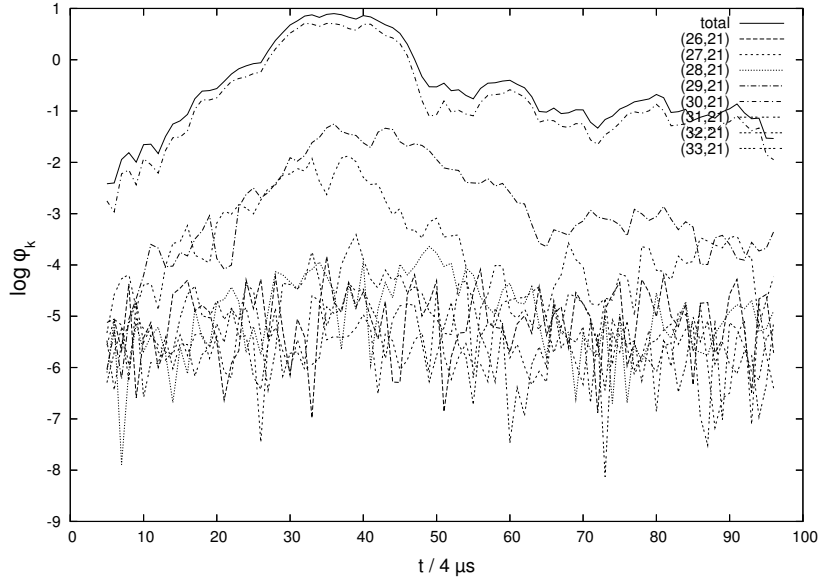


Figure 3.5. Typical mode energy dependence for different m values for $n = 21$, in logarithmic arbitrary units. Time unit on the horizontal axis is $4 \mu\text{s}$.

3.4 Kinetic linear growth

The case with kinetic electrons was not as well investigated in the literature, probably due to the state of kinetic electron development at the time. The non-adiabatic electron response introduces new branches of instability in addition to the ion temperature gradient mode. With only one reference (i.e., Ref. [44]) available to the authors' knowledge, we were restricted to a case with a $\nu^* \neq 0$ and $L_{Te} \rightarrow \infty$, which has the same ITG instability (due to the lack of electron drive) but where the existence of a trapped electron fraction is predicted to further increase growth rates. The paper addresses linear and non-linear evolution of modes, and finite β stabilization of ITG modes.

Because GS2 [42] was not used by the ELMFIRE group for linear stability calculations at the time, this singular reference was chosen as the kinetic electron benchmark case. Discussions with other physicists in the field would have been very useful to this exercise, in retrospect. Correspondence was unsuccessful, as none of the earlier authors wished to (or, were unable to) discuss this exercise with us.

With the kinetic electron population simulated by the full- f particle method, noise problems were further aggravated. In Fig. 3.6 a typical unfiltered result is shown without periodization in the phase signal. If

any modes were to be found at all, the signal is drowned out by the noise and initialisation. Increasing the number of particles was not an option due to the meager computational resources afforded by the group at the time. After trying several variations of simulation parameters unsuccessfully, a drastic filtering regime was adopted: the signal is filtered in time, and the total energy of corresponding n -mode is calculated over a region of the simulation volume, inspired by Ref. [45] (see figure 3.8). Time filtering

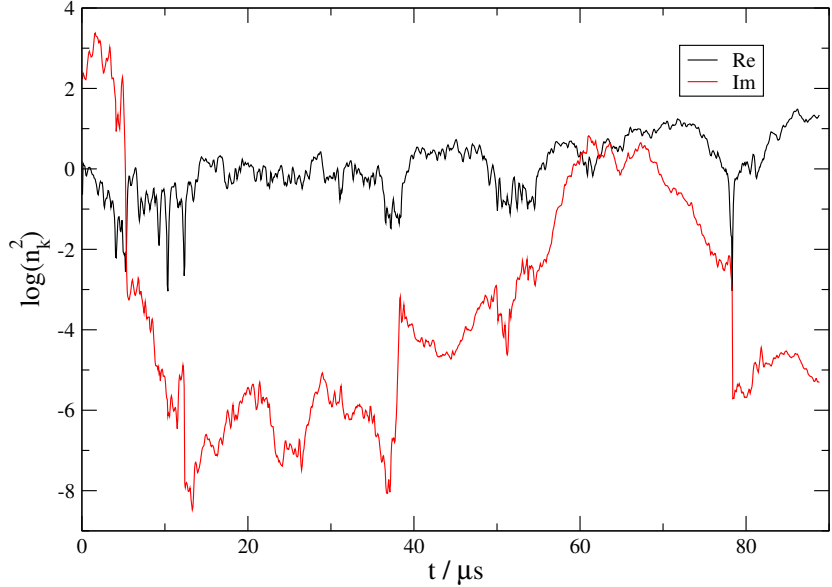


Figure 3.6. Time trace of the time evolution of amplitude and phase of $(70, 49)$ at $r = a/2$. Here time filtering has not been performed.

of the signal, if done properly, suppresses higher frequency oscillations while keeping lower frequency oscillations relatively intact. Although filtering will reduce also the amplitudes of the signal as well as the “noise” we want rid ourselves of, the signal to noise ratio improves as only relative changes in the amplitudes are needed for the linear growth rate and frequency analyses. This is the case only if the filtering window is not changed during the filtering procedure. If the window for a moving average changes, the spectral properties will change (namely the transfer function) and therefore may influence the analysis. A transfer function for a moving average filter is illustrated in figure 3.7.

However, the filtering in time introduces a different problem: a linear growth is exponential, and as such, has a wide spectrum. Applying different width moving averages on different data points will change the results, and therefore the time-filtering scheme is dangerous if used un-

wisely.

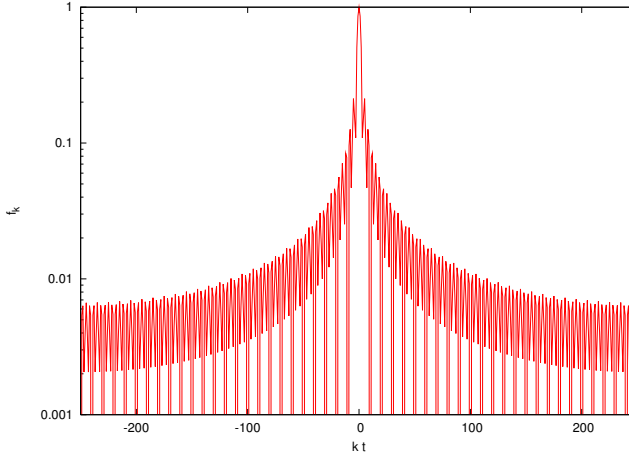


Figure 3.7. A typical transfer function for a moving-average filter of width of 150 points on a time series of 500 points. The analytic transfer function is $g(k) = \sin(Mk)/M \sin(k)$, with $k \in [-\pi, \pi]$ and M is the number of points.

The integration of a quantity $A(\psi_p)$ over volume Ω is given by

$$\{A\}_\Omega = \frac{\int_\Omega A(\psi_p) J(\psi_p, \chi, \zeta) d\psi_p d\chi d\zeta}{\int_\Omega J(\psi_p, \chi, \zeta) d\psi_p d\chi d\zeta}, \quad (3.31)$$

where J is the Jacobian. When $A(\psi_p) = n_i^2(\psi_p; m, n)$ we obtain a measure of the energy associated with the Parseval sum of (m, n) modes for the n mode under investigation. Finding the radial extent of growing modes was done manually over all the possible (m, n) combinations in the simulation, and uniform centered time averaging was performed for the complex Fourier coefficients. We show the typical m -structure for $\{n_i^2\}_\Omega$ for the mode energy in figure 3.8 (in arbitrary units). As can be seen, the most unstable mode here is a side-band mode which is localized off of the nominal region at $q = 10/7$, and the analyses were made for such modes with highest late time amplitudes. This was deemed necessary to obtain a reasonable scale of growth. Error bars have been obtained from least-squares fitting, but are unreliable due to the strong filtering required.

Table 3.4. Simulation parameters for the kinetic linear Cyclone test cases.

$dNX = 31$	$dNY = 300$	$dNZ = 8$	$\Delta t = 7 \cdot 10^{-8} \text{ s}$	$N_{\text{part}} = (28 - 75) \cdot 10^6$
------------	-------------	-----------	--	--

The results from this procedure are given in Publication I figure 3, and the later evaluated GS2 results are shown in figure 3.9. With current resources the kinetic linear growth rate analyses could be done even without

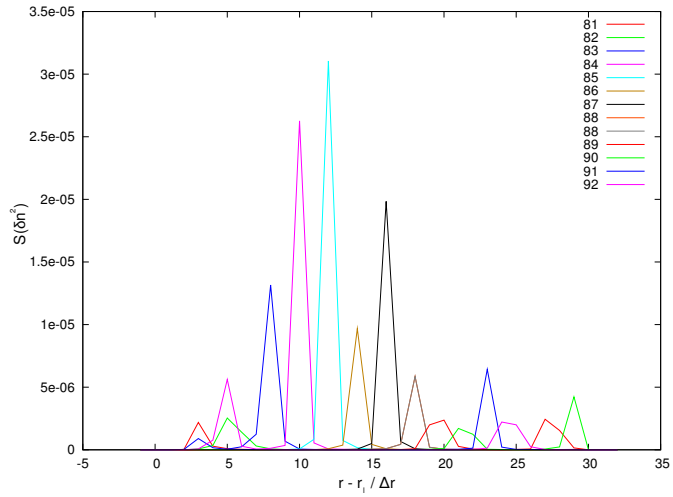


Figure 3.8. A typical radial profile of the energy associated with modes for multiple growing modes in the kinetic simulations. Radial localization of modes is observed.

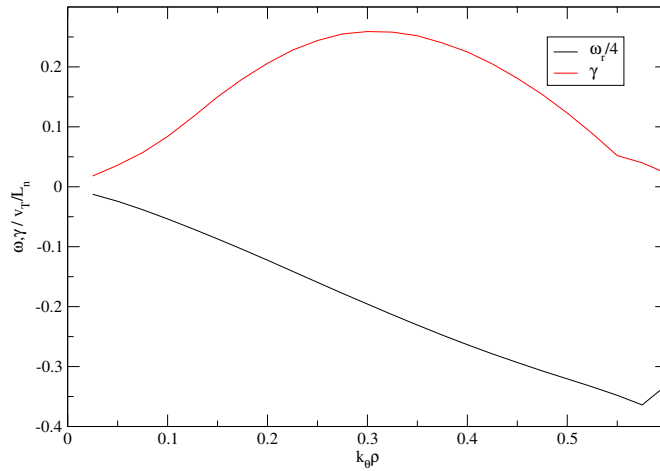


Figure 3.9. Growth rate and frequency spectra for the kinetic Cyclone Base case obtained with the GS2 code.

filtering, which has been done for adiabatic Cyclone calculations. However, these would benefit from spectral filtering and prior equilibration of neoclassical physics using the spectral filter given in Chapter 5. In this case the effect of neoclassical background flows on linear growth rate analyses could be determined using a full *f*code. This was deemed to be outside of the scope of this thesis.

4. Drift-wave driven transport in the presence of neoclassical transport

Big whirls have little whirls,
That feed on their velocity; And
little whirls have lesser whirls,
And so on to viscosity.

Lewis Fry Richardson

4.1 Introduction to drift-wave turbulence

In a non-linear simulation there are generally three phases of the transport evolution. First, there is the (almost) linear growth of an instability, after which the mode growth saturates through non-linearities and simultaneous generation of neoclassical flows, and a steady state of turbulence may be attained. However, a linearly unstable case may be non-linearly stable because of the generation flows in the system, a secondary instability which initially was stable may arise, or transport may be oscillatory due to a dynamics of the flows. Even when the simulation is started with low initial fluctuations, the linear and saturation phases will always be present if unstable conditions are assumed.

Linear growth rate analyses have been used widely to predict transport in the magnetic fusion community, but due to the forementioned reasons are of limited value in analyses of turbulence. Non-linear processes in saturation generally play a much more important part than the linear drive itself [46], although quasi-linear theory may be taken as the first crude approach to turbulence (especially for weak turbulence, a desired property).

How the saturation develops is a rather complicated issue. Turbulent transport depends on background flows (turbulently or neoclassically driven) and wave-wave interaction as well as the driving instability. In any exper-

iments, such flows may be pre-existent and develop during transport and coupled zonal flow (ZF) dynamics. In the simulations any initial flows and perturbations may be added, but without experimental knowledge are conjecture, at best. Therefore, the only possibility is to simulate simplified cases and attempt to induce physical processes that correspond to the experimental situations from which current experimental knowledge, in terms of simultaneous plasma parameters, is unfortunately rather limited. Thus, the computational process that leads to saturation of turbulence through linear growth, non-linear saturation and flow generation is artificial and does not generally occur in nature.

Turbulent saturation in a simulation may be declared when the transport becomes such that quick dynamic changes no longer occur and a steady mean level of transport is attained. Without particle and heat sources and sinks the linear drive is exhausted due to relaxation of profiles and transport quickly wanes. Transport saturation is therefore a dynamical concept, which needs a balance of sources and sinks to exist.

Interaction between waves is currently believed to be the most important process how a turbulent state is reached. When an instability reaches a critical level, it excites secondary waves through non-linear scattering processes (cascades), which siphon off energy from the original wave and grow. These secondary waves interact with other waves of shorter and longer wave lengths in a similar manner, and progressively smaller scale fluctuations emerge. The smaller waves damp due to viscosity, and a stationary turbulent state emerges.

4.1.1 The Hasegawa-Mima-Charney equation

The saturation process of turbulence may be illustrated by the Hasegawa-Mima-Charney (HMC) equation, which presents itself in drift-wave physics as well as flows in planetary atmospheres (Rossby waves). In the latter case the Lorentz force is supplanted with the Coriolis force obtained from the change to a non-inertial rotating co-ordinate system. In plasmas, the scalar potential is electric, whereas in planetary atmospheres it is gravitational.

We begin with the fluid momentum equation using truncation closure at

momentum,

$$\frac{\partial n_a}{\partial t} + \vec{\nabla} \cdot (n_a \vec{v}_a) = 0, \quad (4.1)$$

$$\frac{\partial \vec{v}_a}{\partial t} + \vec{v}_a \cdot \vec{\nabla} \vec{v}_a = \frac{q_a}{m_a} \left(\vec{E} + \vec{v}_a \times \vec{B} \right) - \frac{1}{m_a n_a} \vec{\nabla} p_a, \quad (4.2)$$

which gives us as the the lowest order solution, with $\nabla p \rightarrow 0$ and $\vec{E} = -\nabla\phi$, in the form

$$v_E = -\nabla\phi \times \frac{\vec{B}}{B_0^2} \quad (4.3)$$

which allows us to iteratively solve equation 4.2:

$$\frac{\partial \vec{v}_E}{\partial t} + \vec{v}_E \cdot \vec{\nabla} \vec{v}_E = \frac{q_a}{m_a} \vec{v}_p \times \vec{B} \rightarrow \vec{v}_p = \frac{1}{\Omega_i B_0} \left[-\frac{\partial}{\partial t} \nabla_{\perp} \phi - (\vec{v}_E \cdot \nabla_{\perp}) \nabla_{\perp} \phi \right], \quad (4.4)$$

and express the total fluid velocity as

$$\vec{v} = -\nabla\phi \times \frac{\vec{B}}{B_0^2} + \frac{1}{\Omega_i B_0} \left[-\frac{\partial}{\partial t} \nabla_{\perp} \phi - (\vec{v}_E \cdot \nabla_{\perp}) \nabla_{\perp} \phi \right]. \quad (4.5)$$

The magnetic field has been assumed to be homogeneous which removes compressibility through the gradient and curvature and v_E , and because the pressure gradient was neglected, also the diamagnetic velocity is removed.

The continuity equation may be re-expressed as

$$\frac{d \ln n}{dt} + \nabla \cdot \vec{v} = 0, \quad (4.6)$$

with incompressible (in the highest order) flow and adiabaticity $\delta n/n_0 = e\phi/T_e$, which lead us to

$$\ln n = \ln n_0 + \ln \left[1 + \frac{\delta n}{n_0} \right] = \ln n_0 + \ln \left[1 + \frac{e\phi}{T_e} \right] \approx \ln n_0 + \frac{e\phi}{T_e}. \quad (4.7)$$

Including the advection and compressibility by v

$$\frac{\partial}{\partial t} \left[\frac{e\phi}{T_e} \right] + \vec{v}_E \cdot \nabla \ln n_0 + \nabla \cdot \vec{v}_p = 0, \quad (4.8)$$

which written out gives

$$\frac{\partial}{\partial t} \left(\frac{1}{\Omega_i B_0} \nabla_{\perp}^2 \phi - \frac{e\phi}{T_e} \right) + (\vec{v}_E \cdot \nabla) \left[\frac{1}{\Omega_i B_0} \nabla_{\perp}^2 \phi - \ln \frac{n_0}{\Omega_i} \right] = 0. \quad (4.9)$$

The equation is now normalized by

$$\Omega_i t \rightarrow t, \quad \frac{(x, y)}{\rho_s} \rightarrow (x, y), \quad \frac{e\phi}{T_e} \rightarrow \phi$$

and we obtain the Hasegawa-Mima-Charney equation

$$\frac{\partial}{\partial t} (\nabla^2 \phi - \phi) - [(\nabla \phi \times \hat{b}) \cdot \nabla] \left[\nabla^2 \phi - \ln \frac{n_0}{\Omega_i} \right] = 0. \quad (4.10)$$

The equation may be expanded as a Fourier sum of elementary solutions, just as we did for the linear system in Chapter 3, which gives us

$$\begin{aligned}\partial_t \phi_k &= i\omega_k \phi_k + \sum_{k_1+k_2=k} \Lambda_{k_1, k_2}^k \phi_{k_1} \phi_{k_2}, \\ \Lambda_{k_1, k_2}^k &= \frac{1}{2} \frac{\hat{b} \cdot (k_1 \times k_2)}{1 + k^2} (k_2^2 - k_1^2), \\ \omega_k &= \frac{k \times \hat{b}}{1 + k^2} \cdot \frac{\nabla n_0}{n\Omega_i}.\end{aligned}\tag{4.11}$$

We see that the time derivative operates on a linear quantity, and the non-linear term includes a quadratic nonlinearity and an imaginary advector. There is no linear instability in this model, only propagation of modes, so the model excludes linear growth (in contrast to Chapter 3, where non-linearity was dropped). This equation conserves energy and enstrophy, and is therefore a suitable toy model for considerations into vortex dynamics in the plasma, such as the generation of zonal flows through the modulational instability [47]. Even a noise-driven Hasegawa-Mima produces a spectrum [48], which is important to acknowledge especially in the context of Monte Carlo simulations.

Results of ELMFIRE simulations are compared in Publication IV to Hasegawa-Wakatani simulation results where the electron adiabaticity condition is relaxed. Initial dimensional analysis [49] suggested that the energy spectrum of drift waves should fall off as $S(\phi_k^2) \propto k^{-5}$, if low- β plasmas are considered. Differences in dynamics across flux surfaces and on flux surfaces, generally spectra of the form $k_\theta^{-\alpha_\theta} k_r^{-\alpha_r}$ are found. Numerical simulations of Hasegawa-Wakatani equations [50] yield the values of $\alpha = 1.6$, $\alpha = 2.7$, $\alpha = 4.2$ for the exponent of $S(\tilde{n}_k^2)$ spectra, in progressively more adiabatic (i.e., collisionless in the absence of trapping) regimes.

4.2 The Cyclone Base case

4.2.1 Some background of the Cyclone cases

The ‘‘Cyclone base’’ case has not been deliberately chosen to be a benchmark case, but it has become such *ad hoc* through extensive investigations in the literature. It is based on the DIII-D shot #18499¹. It has several problems as a benchmark case for turbulence studies. The q profile in the case is not realistic (i.e., experimentally reproducible), and

¹See <http://www.ipp.mpg.de/~bds/cyclone/D3D81499/>.

due to the H-mode transport barrier present in the edge it incorporates a huge pedestal. It is — like almost all experimental situations — near the threshold of instability, where plasma shape and electromagnetic effects are important, and various heat sources (Ohmic, neutral particle injection, radiofrequency) are present. Transport scaling obtained by increasing the temperature gradient is purely artificial, and not experimentally reproducible due to profile stiffness observed in experiments.

However, as a code-to-code comparison, such a case is of interest. In the absence of sources and sinks, the χ_i value is expected to slowly decay as the gradients relax and instability drive diminishes. The simulation should produce a stable system as its end result. Transport scalings based on this observation have been developed (see Ref. [12]), and it was therefore decided in the TF-ITM framework to compare the χ_i versus R/L_T evolution in transport. Because turbulent dynamics should be independent of the initial values set into codes, the χ_i curves should overlap in long enough simulations.

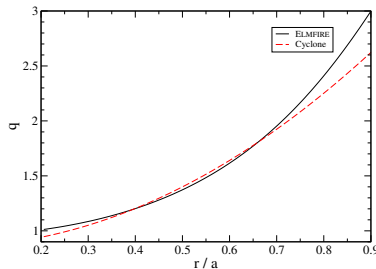


Figure 4.1. The q -profile as a function of normalized radius in the Cyclone base case and ELMFIRE, obtained from minimization of the squared errors of q while keeping the real shear at $r/a = 0.5$.

The radial heat energy flux for adiabatic simulations can be obtained from the distribution function as a moment, using

$$Q_r = \int H v_r f J dv_{\perp} dv_{\parallel}, \quad (4.12)$$

where H is the drift-Hamiltonian ((2.35)), the radial velocity includes drifts. In practice, this can be evaluated by taking the difference between the starting position and ending position of the particle, and dividing by the time step. It can be shown that for adiabatic electrons the mean particle flux over the flux surface is zero, so the energy and heat fluxes are equal. The full fluxes are diagnosed in ELMFIRE, however. There is a question whether the electric potential should be included in the energy flux, but it has not been included in the results we give below. The heat

and energy fluxes are related through

$$\vec{Q} = \vec{q} + \gamma p \vec{v}, \quad (4.13)$$

where the factor $\gamma = 3/2$ is chosen because of partial cancellation of the convective flux and work done by electrostatic field on the radial current [51, 52].

With ELMFIRE first long simulations exhibited a non-convergence of transport, as shown in Publication III and Publication V. The quenching of turbulence coincides with growth of a characteristic electric field structure. The question why this non-convergence is observed arises. In the following discussion we attempt to evaluate various hypotheses on this issue, and present simulations where the effect is absent.

4.2.2 Adiabatic non-linear runs of Cyclone Base case

The original ‘‘Cyclone base’’ case [12] is a problem where adiabatic electrons are assumed. This case has become a standard benchmark for all turbulence codes, and therefore has been investigated also with ELMFIRE.

The first adiabatic non-linear runs of ‘‘Cyclone base’’ case with density dependent particle weights were encouraging (see figure 4.2). Here a local adiabatic model (2.16) with only toroidally localized average over the flux surface was used, and only later was improved to ensure that from the full flux-surface average of the linearized electron response was used. The initial results were suspect, and investigations on the adiabatic model were taken. Equal particle weights were introduced, because it was observed that the binary collision model of Ref. [53] did not function well with unequal particle weights and impurities (not used here), and particle noise properties were expected to improve in long simulations.

Also one misadventure was the use of concurrent ion density as the electron background density. A peculiar non-convergence of transport was observed for cases where the electron density was allowed to follow the flux-surface average of the ion density. The adiabatic model was modified to keep electron density at the same value as the flux surface averaged value of the ion density just after initialisation. We discuss the choice of the adiabatic model more in depth in Chapter 2. The change from the older adiabatic model with $\langle n_e \rangle = \langle n_i \rangle(t)$ to an adiabatic model with $\langle n_e \rangle = \langle n_i \rangle(t = 0)$ changed the dynamics remarkably in the new simulations with constant particle weights, in the absence of collisions. In the erroneous simulations we found that strong radial density rippling (with

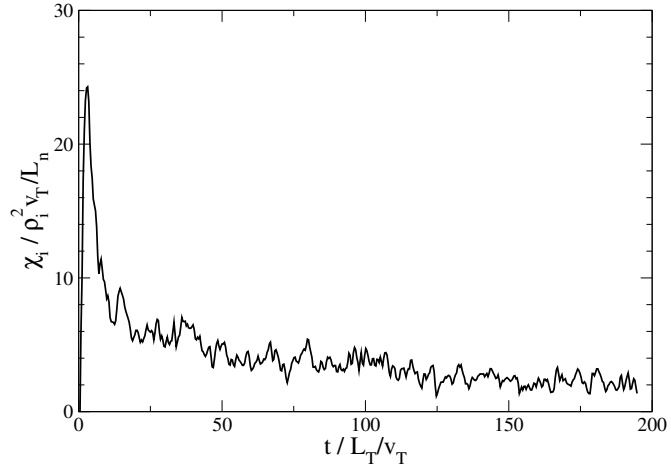


Figure 4.2. The preliminary result for χ_i . Here particles with density dependent weights were used.

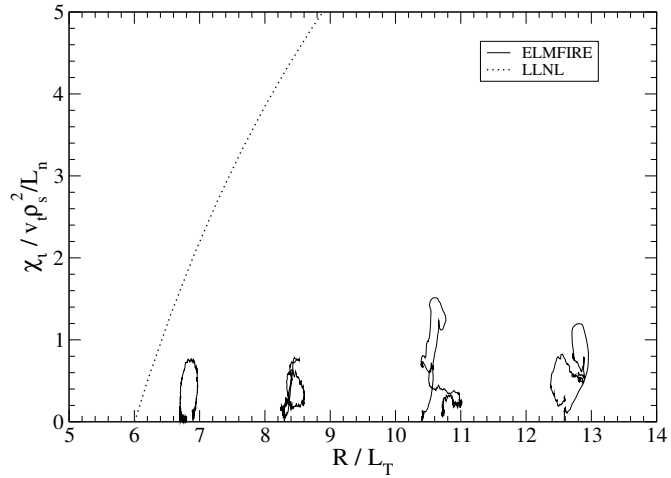


Figure 4.3. The χ_i scaling with $n_e \propto \langle n_i \rangle (t = 0)$. The LLNL scaling curve from Ref. [12] is given for reference.

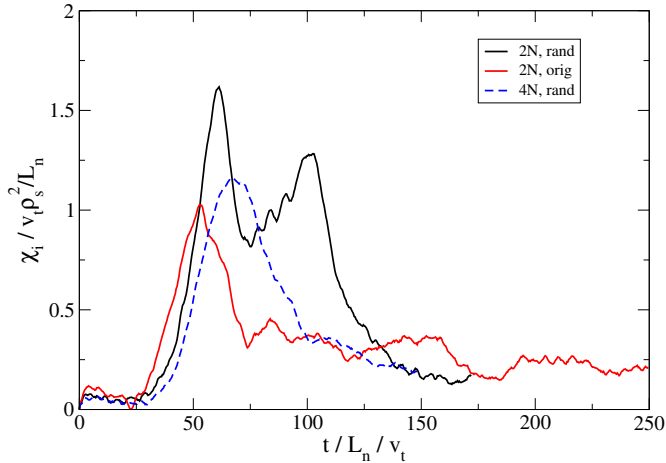


Figure 4.4. Adiabatic “Cyclone base” simulations for $R/L_T = 8.28$ case, with original initialisation and ζ -angle randomisation with 445 million particles (2N) and 890 million particles (4N).

almost singular k_r) was created through particle transport which caused electric fields that suppressed turbulence, but in the newer simulations such rippling effect was absent. However, as shown in figure 4.3, these simulations also were non-convergent. The simulations that were developed furthest at the time, with highest particle numbers, were presented in Publication III.

4.2.3 Initialisation and particle randomisation

Because the initialisation manifests an initial disturbance as shown in figure 5.5, it was deemed necessary to control the initialised spectrum by randomisation in the ζ -direction. This procedure is allowed by the fact that the particle motion is invariant (for axisymmetry and in the absence of electric fields) for rotations along the torus. Because all $n \neq 0$ modes that arise from the initialisation are suppressed by this procedure, density is efficiently smoothed, while allowing for a seed perturbation in density that ensures growth of instabilities (from shot noise). The initialisation perturbation is dependent on the number of initialisation points in configuration space co-ordinates, and as such, changes in particle numbers are performed for the pitch variable. It is unaffected by the particle weighting scheme. We believe this perturbation arises due to finite steps used in following the particles while they are being initialized (see Chapter 5.2). However, while increasing the number of initialization points from 30 to 90 increases the maximal mode number of the disturbance, significant

low-order mode numbers exist.

Several simulations were performed for randomized and original initial distributions with different marker numbers, but for clarity we show only three in figure 4.4. Here the initial transient and later evolution are illustrated by first taking a nominal simulation where 445 million particles were used (2N,orig), randomizing the initial distribution from this case before fields have acted on them (2N,rand), and simulating a 890 million particle case with randomisation. If convergence of the initial transient is found between the randomized cases, we may assess the simulations to be converged. While these simulations show similar initial dynamics, the height and shape of the initial transient is very different. This suggests that convergence has not been found yet.

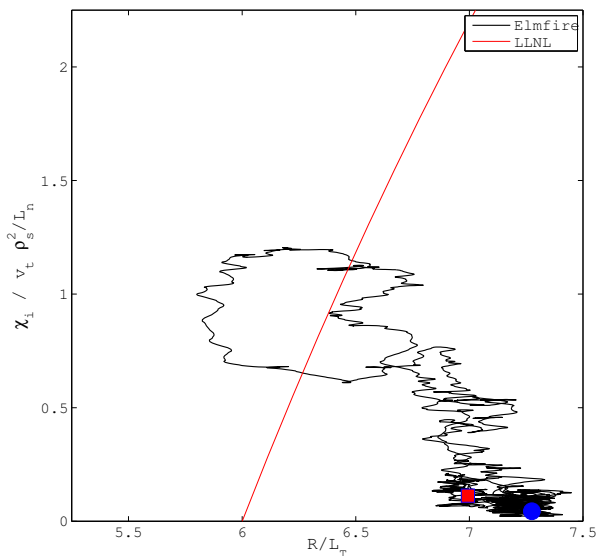


Figure 4.5. The local χ_i scaling with R/L_T at $r/a = 0.5$ in the PPCF PIII $R/L_T = 6.9$ case, with the LLNL scaling curve from Ref. [12]. We observe clear non-convergence of the heat conductivity in this case.

We have simulated in figure 4.6 the standard $R/L_T = 6.9$ case with uneven particle weights, in contrast to figure 4.5. With these parameter choices we observe profile relaxation and a bursty χ_i which terminates near the LLNL stabilization value. In figure 4.7 we show that the transport is almost entirely due to convection, based on the plots from the convective heat flux $Q = 5/3 p v_{E \times B}$ and from the purely statistical measure

obtained in the code. The varying particle weights allow for more particle allocation in the high-density inner regions, with improved noise characteristics. We observe that an increased particle number improves also transport convergence, which suggests that the problem is noise related.

4.2.4 Unphysical turbulence quenching mechanisms

Finite orbit width effects are rarely investigated by gyrokinetic codes, because in δf codes the curvature and gradient terms do not act on the background. In gyro-fluid codes such neoclassical effects are introduced through additional conductivities, and as such, finite orbit width effects are neglected. The ELMFIRE is unique in this regard, as such background distribution dependent terms are naturally included, but this dynamics causes also additional problems near the boundaries due to combination of orbit losses and boundary conditions.

Particle noise and the thermalization problem

Generally it is accepted that numerical simulation of turbulence (of any kind) is challenging, because non-linear interactions create progressively shorter wavelengths in the system. In a real system they will be eventually thermalized by collisions, but in a simulation the thermalization problem is related to the fact that any undamped simulation system with a cascade and a resolution limit will inevitably hit that limit, because the cascade produces ever smaller scales. This is remedied in gyrofluid codes by introducing hyperviscosity (e.g, $\mu \nabla^6 v$) which damps away high- k fluctuations but retains long wavelength fluctuations. The ORB5/NEMORB gyrokinetic particle codes use a Krook collisional operator to achieve the same damping [54].

In ELMFIRE simulations where the whole simulation region is affected by collisions with a fictitious background distribution we also observe saturation of χ_i , but because this method introduces also a drag on the mean flows we discard this option as a possible solution.

It is also possible for particle noise to drown out a coherent signal, which can be seen in Publication I.

Proposed mechanism for E_r growth from cooling in absence of Γ

Heat transport naturally leads to temperature relaxation, and if the distribution function is assumed to have thermalized well in this process, we may infer a density change (due to change in the mean orbit width). In the

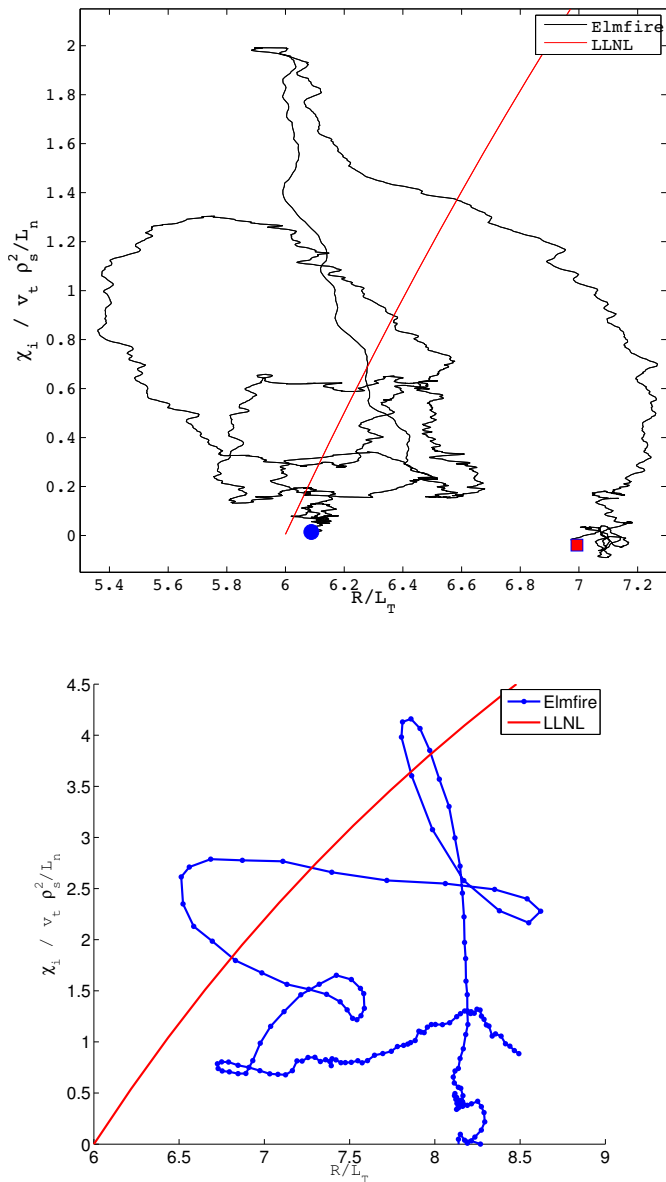


Figure 4.6. Heat flux as a function of R/L_T in simulations with unequal weights. The LLNL curve [12] is plotted as reference in both cases. The simulation starts at the square and ends at the circle. The values are evaluated at $r/a = 0.5$. The total particle number is 800 M in the 6.9 case and 3000 M in the 8.28 case.

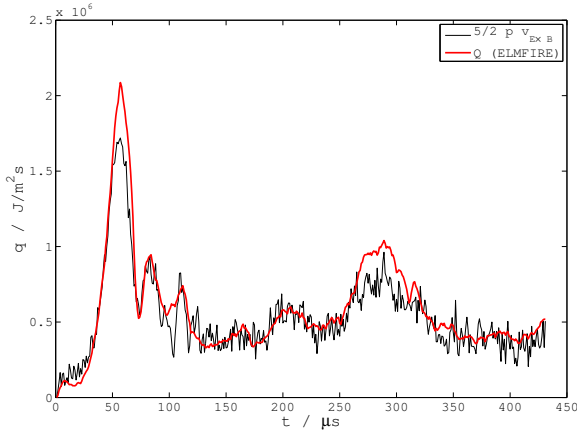


Figure 4.7. Comparison of the $E \times B$ flux to energy (Q_i) flux in the $R/L_T = 10.35$ case at $r/a = 0.5$. The flux is clearly dominated by convection.

adiabatic electron model this density change is ignored, which will lead to a difference between electron and ion density, which results in a polarization response and $E \times B$ flows. This is best illustrated by the following analysis.

If, for simplicity, one takes the perturbation $c \cos(r/b)$ of the ion orbit half width w due to the ion temperature relaxation along the radial direction r , the related shrinking and widening of orbits causes an ion density perturbation $-(cw/3b^2)n_0 \cos(r/b)$, where n_0 is the unperturbed density at $r/b = \pi/2$. Taking into account of the ion polarization, quasineutrality condition gives the potential perturbation $-\Omega c B(w/3) \cos(r/b)$, where Ω is the ion cyclotron frequency and B is the magnetic field.

We calculate the amplitude $-\Omega c B w/3$ for the ELMFIRE Cyclone Base case simulation in figure 4.3. Here, $B = 1.91$ T, $\Omega = 10^8$ s $^{-1}$, and $w = 2.5$ cm for thermal bananas at radius $r/a = 0.5$ (the node of bipolarity $r/b = \pi/2$). The relative ion orbit width perturbation c/w can be, directly read from the data e.g., at the end of calculation. From the picture of T_i profile, we read for the perturbation T_i about -250 eV at the inner relaxation maximum implying $c/w = 0.035$. If these numbers, and the fraction of trapped ions 0.3, now are put into our expression of potential perturbation amplitude, we get 500 V at the inner relaxation maximum for the potential perturbation at the end of calculation.

Note that we have a negative c at the $r/a = 0.5$ (negative maximum of perturbation) which means a positive potential maximum at that point. Both the direction and amplitude of the resulting bipolar perturbation

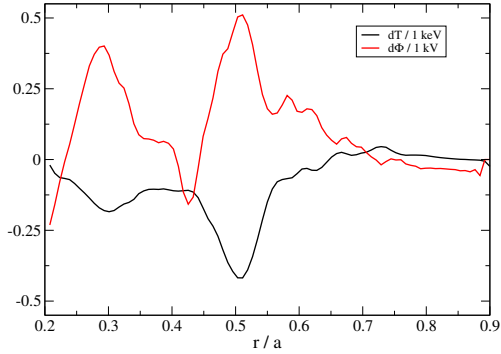


Figure 4.8. Cooling induced electric potential growth at $r/a = 0.5$ in adiabatic Cyclone case with $R/L_T = 10.35$.

bation from ELMFIRE simulation are in fair agreement with this theory. What matters here is the magnitude of T_i and its relaxation. The larger T_i or its relaxation, the larger is the effect. In our Cyclone base simulations, we have taken $T_i \approx 4000$ eV at the inner edge. T_i relaxation is also enhanced by the (unphysical) initial transient in ion heat diffusivity in simulations. Thus, for comparison of results from different codes, we have to look at whether the T_i relaxation is equally strong and T_i is at the same level (ion orbits wide enough to clearly see the effect). E.g., any effort to keep the inner edge in thermal bath with T_i fixed there in GYSELA (see PIII) may mask this effect.

When electrons are kinetic and collisions are taken into account, the above effect can affect transport, but due to electron dynamics saturates. Collisions take care of the return ion current which neutralizes the charge separation from ion orbit modification sooner or later. Also, T_i relaxation is now also partially controlled by ambipolar electron/ion radial convection. Convective heat losses do not cause orbit modifications between ions and electrons. In kinetic ELMFIRE simulations with collisions, this effect has not been clearly identified.

The result means that it is not possible to calculate saturation in the adiabatic limit in the full f code unless electron adiabaticity is redefined to prevent charge separation through the ion orbit shrinking/widening (but this may cause other problems) or unless T_i profile is kept unrelaxed (by some thermal bath or similar ways). In the kinetic case, collisions and electron/ion convection ultimately cancel this charge separation thus preventing any steady potential bipolarity (the latter may appear only transiently for weak collisions).

Strong curvature in the electric potential induces an orbit squeezing (or,

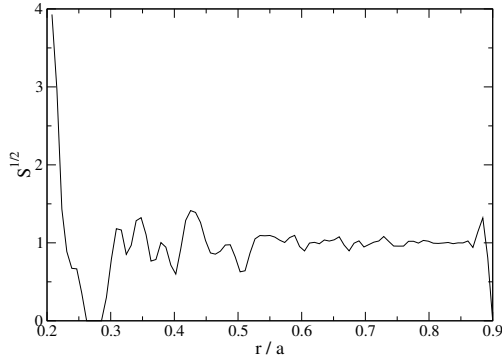


Figure 4.9. Radial profile of the orbit squeezing parameter of figure 4.8.

widening) effect [55], which also changes density profile. In figure 4.9 we present the squeezing parameter

$$S = 1 - \frac{q_e}{m_d \Omega_p} \frac{\partial^2 \phi}{\partial r^2}, \quad (4.14)$$

where $\Omega_p = q_e B_p / m_d$ is the bounce frequency. The particle orbits are proportional to the squeezing parameter by $S^{-1/2}$, so if $S < 1$ we obtain widened orbits. This appears to be important near the inner border of the simulation, where the orbit loss dynamics caused by the widening may influence radial electric field dynamics. Here we have used Dirichlet boundary conditions for the potential. Particle boundary conditions are as in Publication I.

The growth of electric field shear stresses turbulence, and beyond some limit, suppresses it. This could result in a decaying of the saturation state in adiabatic cases.

4.2.5 Kinetic electron non-linear saturation

Electron non-adiabaticity introduces several changes to the transport dynamics: electron trapping makes the electron response to ion perturbations less efficient and therefore enhances growth rates of modes (see Chapter 3), and makes significant density relaxation (beyond polarisation density response) possible. Therefore, this presents a new channel of heat transport, namely ballistic transport due to gross $E \times B$ radial particle flux (which is absent in adiabatic simulations).

The non-linear simulations where the modes are allowed to interact are performed using the same Cyclone base case parameters as used for the linear calculations as basis (table 3.1), except for the parameter a/ρ_s , which in these cases is taken to be 300 (here $\rho_s = \sqrt{T_i/m_i}$). This was

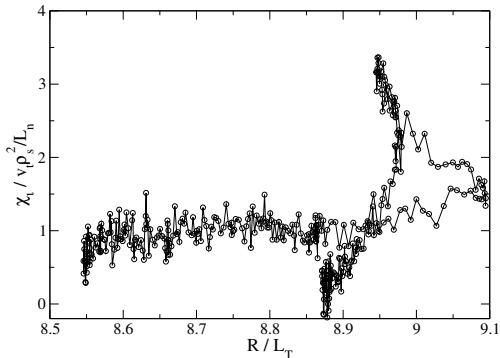


Figure 4.10. Simulation of the Cyclone base case parameters with kinetic electrons and 890 million particles. The transport reaches quickly a gyro-Bohm value after the initial transient.

produced in the kinetic electron cases by scaling the parameters R , a and I_{tot} by a factor of 2, while keeping the other parameters intact.

Evolution of the thermal conductivity $\chi_i(a/2)$ is investigated in two different ways: in time and against the local temperature gradient scale length. The latter is also an important diagnostic, as the change in the local gradient scale length can be utilized in producing R/L_T scans [5]. These results are illustrated in Publication I figure 8 and figure 4.10.

In the first kinetic simulations particle noise was found to be very high (only 1500 particles per cell were used), and no growth of turbulence was seen. However, the choice of $n_i(r = 0.5) = 5 \cdot 10^{19} \text{ m}^{-3}$, in the presence of collisions increased collisionality from $\nu_{ei} L_n / v_{Ti} = 0.45$ to 45, 100 times stronger collisionality than in reference [44]. This enabled a neoclassical transport analysis and noise estimation from this data, and a rather interesting picture emerges in Publication I figure 4. The following results are presented in this figure: flux-surface averaging the charge separation and non-averaged, with collisions and without. With collisions and no averaging the highest χ_i was found, and flux-surface averaging the potential reduced this but retained the dynamics. Without collisions the χ_i value dropped significantly, to the level initially found in the first case. Flux-surface averaging further decreased the conductivity, and no significant time evolution of the χ_i remained to be seen.

This can be interpreted in the following way (PI): collisions induce the neoclassical transport levels, to which noise contributes additively. Flux-surface averaging reduces the noise in $E \times B$ heat flows but retains neoclassical contributions, and removing collisions removes this contribution.

To find the turbulent behavior, the collisionality was decreased by chang-

ing the density to $n_i(r = 0.5) = 5 \cdot 10^{17} \text{ m}^{-3}$, and by varying the particle number to find where the noise level is sufficiently low for the turbulence to grow. Publication I figure 7 shows the ion heat conductivity at $r = a/2$ which saturates after an overshoot that is progressively larger as a function of particles.

Further insight into the saturation is provided by figure 4.10 where the χ_i is plotted as a function of R/L_{T_i} and time in due course of the simulation. The obtained χ_i evolution reflects the features familiar from other (δf) code results in similar cases [56]. After the overshoot and some steepening of the T_i radial profile, χ_i and T_i profile relax towards the gyroBohm condition $\chi L_n / \rho_s^2 v_{T_i} \sim 1$ for ion heat conductivity. One can compare this χ_i value at $R/L_{T_i} = 9$ with the value of $\chi L_n / \rho_s^2 v_{T_i} = 1.3$ obtained in another simulation (see Fig.2 in [57]) in the Cyclone base case where global δf simulations (with adiabatic electrons) were performed. Global simulations may perform differently from the flux tube calculations, which was already stressed in the latter work. However, based on Publication I figure 7, where the end-state fluxes are independent of particle number, we infer that the resulting transport suffers from non-linear noise fluxes which overtake turbulence later on in the simulations. Figure 4.10 also suggest this interpretation, as the conductivity does not exhibit burstiness generally observed in turbulent simulations.

4.3 FT-2 simulations of turbulence and neoclassical physics

The FT-2 tokamak is the perfect experiment for ELMFIRE to simulate. First simulations while early development of the code were performed with FT-2 parameters, and especially investigations of the kinetic electron model were motivated by the experimental conditions of this machine. It was realized from early investigations with the Weiland model that the FT-2 is mostly trapped electron mode unstable, which necessitates the use of a kinetic electron species in simulations. The FT-2 also has high collisionality, low β , large aspect ratio and ρ_* , so it is much less demanding computationally than the big experiments are. Also, neoclassical physics is very prominent in FT-2 shots, and this makes it possible to investigate the interplay between micro-turbulence and neoclassical mechanisms for poloidal flows.

Therefore a lot of work related to this thesis and other publications made with the ELMFIRE concentrate on the FT-2. The role of simultaneous core

heating and edge cooling has been investigated (Publication I), neoclassical investigations were performed (PII), and also comparisons to Doppler reflectometry signal of the density fluctuations has been performed (PVI). Spectral analyses of the fluctuations have been performed from the very beginning of the ELMFIRE project (PIV), which were the starting point for experimental comparisons. Later this work was taken over by S. Leerink.

Table 4.1. Parameter ranges for the FT-2 tokamak used in this work.

$R = 0.55 \text{ m}$	$a = 0.08 \text{ m}$	$R/a = 6.875$
$q = 1.2 - 7$	$\hat{s} = 0.25 - 2$	$I_{tot} = 18 - 55 \text{ kA}$
$T_i(0) = 80 - 120 \text{ eV}$	$B_T(0) = 2.2 \text{ T}$	$n_i(0) = 0.5 \cdot 10^{18} \text{ m}^{-3}$

4.3.1 Spectral investigations and dynamics of a flux-driven system

The initial cases that were of interest were the lower hybrid ion heated cases of the FT-2 given in publications I and IV. They were performed using a stochastic lower-hybrid heating model which specifies a threshold velocity and upscattering of particle energy. Thermalization would occur through the binary collision operator. On the outer boundary, we would employ a charge exchange operator (which based on the probability of this interaction, would bring energy down) and recycling lost particles as re-initialized neutrals (this was done on electron-ion pair basis).

Many different types of simulations of the same basic type were performed, some were started with low gradients and heating would bring this up, as well as starting from a high temperature and retaining the gradient lost through transport using the heating technique. This source was used to inject off-axis energy into the system, which would keep up fluxes. Heat was removed from outer boundary using charge exchange reactions and re-ionization based on the neutral profiles obtained from the experiment.

Several interesting observations were made from these simulations, one of which was the creation of a knee-point in the electron temperature and density in between the heating and cooling regions (published in EPS'05&06 [58, 59]). The fluxes needed to drive the system to this state were similar to the heating power used in the experiments. The current SOL model (used in Publication VII) was not available for this case yet. While some others have attempted to simulate the FT-2 (see Publication

III), currently ELMFIRE is the only code available for this machine.

4.3.2 Neo-classical equilibrium and effect of turbulence

An interesting question in concomitant neoclassical and turbulent investigations is, whether Reynolds stress contribution affects the neoclassically determined poloidal flows. It has been determined earlier [4, 60] that neoclassical flows may interact with turbulence through shearing, by lowering turbulence levels. However, some references also suggested that turbulence might have an effect on neoclassical electric fields as well [61], which needed investigation.

In Publication II we investigated this by modifying the FT-2 parameters so that proper neoclassical applicability regime was better heeded: current was increased to 55 kA, a parabolic current profile was adopted, and deuterium was chosen as the particle species. The FT-2 has operated shots with deuterium plasmas. In figure 4.11 we present the fluctuation

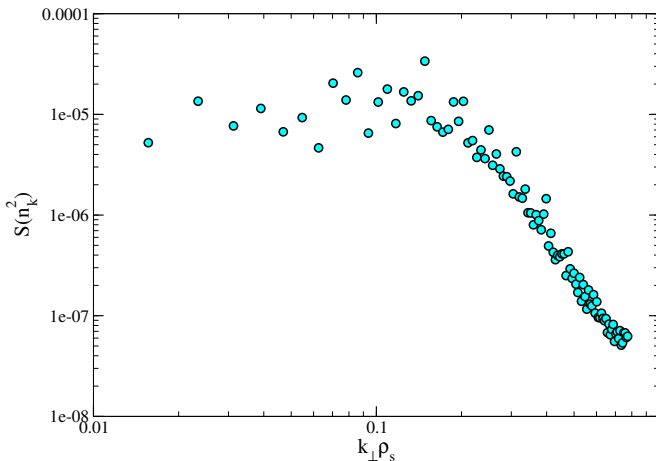


Figure 4.11. Turbulence spectra for the case shown in Publication II. The saturation spectrum clearly exhibits a power law. The slope can be evaluated to be -4.0 ± 0.1 .

spectrum for density in this simulation. The exponent of the spectrum lies near the adiabatic limit of the Hasegawa-Wakatani coupling constant (see Publication IV), although the system is TEM unstable as FT-2 manifests. The PDF of density fluctuations is shown in figure 4.12, In flux-surface averaged simulation of this case, we find a remarkable correspondence with the Hazeltine-Hinton radial electric field (figure 4.13). Only the outermost value differs from theory, which is due to boundary treatment which introduces drag. Inclusion of impurities and lower current

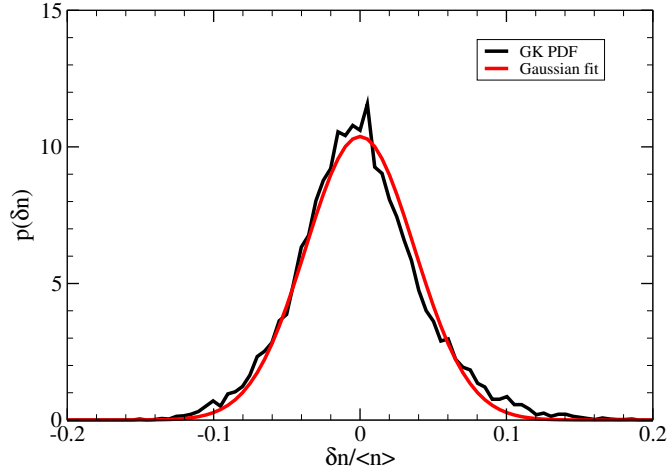


Figure 4.12. Probability distribution function of density fluctuations, relative to background density. We see that the fluctuations are slightly negatively biased compared to the symmetric Gaussian fit. The Gaussian form has since been identified with the geodesic acoustic oscillation (reference VII)

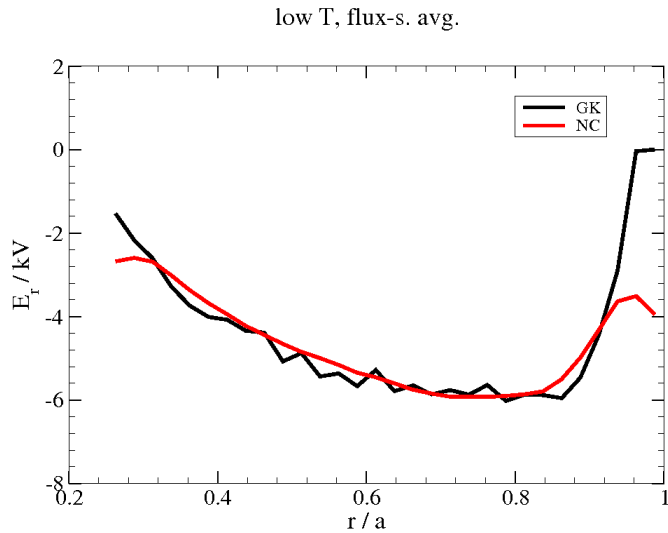


Figure 4.13. Neo-classical electric field from flux-surface averaging. This was only alluded to in Publication II, but was requested to be seen by the referee.

complicates neoclassical analysis, as seen in Publication VII.

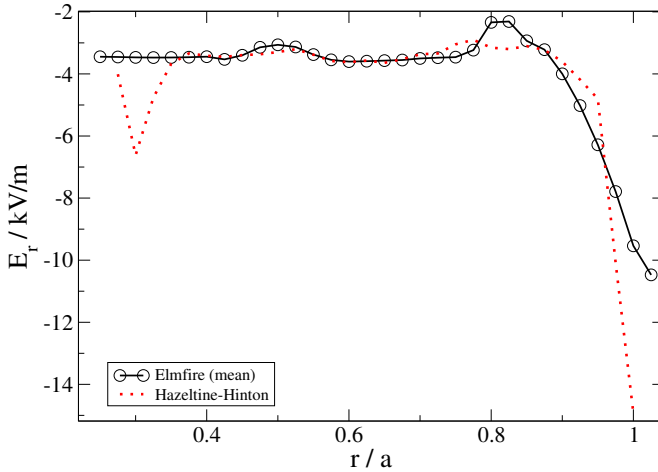


Figure 4.14. Recalculation with the self force corrected. Now we see that the mean field (obtained with Savitzky-Golay filtering) agrees well with the neoclassical expression, contrary to PII.

The only question that remained in this case was the difference observed in the radial electric field when turbulence was allowed to grow. We have since revisited this case by simulating it with the current code versions, and the result for the mean electric field is shown in figure 4.14. Now the neoclassical expression (obtained after profile relaxation) closely follows the simulation result, after local least squares filtering in radius and time. Reynolds stresses remain in the simulation, but they only drive fluctuations of E_r from the NC equilibrium. The reason for this difference is a net particle flux that is caused by a self force due to interpolation choices, which was identified later.

This case has been widely used to improve confidence in the code after further development, because it exhibits turbulence and has simpler neoclassical physics than the case in PVII.

4.3.3 Long-term transport and comparison to Doppler reflectometry

Recently the code results were compared to Doppler reflectometry measurements on the FT-2 tokamak in Publication VII. The difference between this case and the Cyclone results given earlier in this work is the collisional regime: the FT-2 parameters are strongly collisional, while still exhibiting interesting TEM turbulence with strong fluctuations. The required particle numbers were therefore much lower, while it was quickly

found that the high shear in FT-2 required the use of radially dense grid, especially near the outer boundary where the experimental diagnostic was located. We discuss the resolution requirement more in Chapter 5, which was instrumental in broadening the turbulent spectrum which was very coherent in low-resolution runs. In the beginning of the simulation the dynamical neo-classical equilibrium was first developed, and then filtering was turned off and turbulence was allowed to develop. See figure 5.7 for details.

The lessons learned from both of these cases are the basis of current work to simulate Ohmic TEXTOR plasmas, where the parameter regime is closer to Cyclone. There is also an on-going project to simulate ASDEX Upgrade Langmuir probe measurements with the TF-ITM.

5. Some numerical aspects of gyrokinetic particle simulation

On two occasions I have been asked, “Pray, Mr. Babbage, if you put into the machine wrong figures, will the right answers come out?” ... I am not able rightly to apprehend the kind of confusion of ideas that could provoke such a question.

Charles Babbage

This chapter concerns some very important lessons learned while developing the ELMFIRE. We have improved memory consumption, linear system solution, and practical storage of the dynamically collected matrix just to mention a few things not included here, but we deemed them to be outside the scope of this work.

5.1 Discretization, null-space and accuracy

How the numerical approximation of differential operators is defined is of great importance. It is well known that centered differences are difficult to invert, because they generally introduce zero eigenvalues in the discrete system, which usually tend to explode dynamically.

5.1.1 Resolving power of a finite-differencing scheme

The polarization operator for gyrokinetic particle simulations is an elliptic operator, which may be approximated in the long-wavelength limit as a Laplacian. Therefore, we may investigate numerical accuracy with the Poisson equation

$$\nabla^2 \phi = \rho \tag{5.1}$$

as a toy model. The discretized Laplacian operator is $\nabla_h^2 \phi = 1/h^2(\phi(x-h) - 2\phi(x) + \phi(x+h))$, which can be Fourier transformed by taking $\phi(x) = e^{ikx} \phi(k)$. With this we obtain

$$-k^2 \phi(k) = \rho(k), \quad (5.2)$$

$$\frac{2(\cos(hk) - 1)}{h^2} \phi(k) = \rho(k). \quad (5.3)$$

These expressions are pictured in Fig. 5.1. It is trivial to see that the 2nd order Taylor expansion of Eq. 5.3 gives the exact form of Eq. 5.2, but includes $O(h^2)$ error terms. The gyrokinetic operator is Laplacian-like for long wavelengths, as shown in figure 5.2.

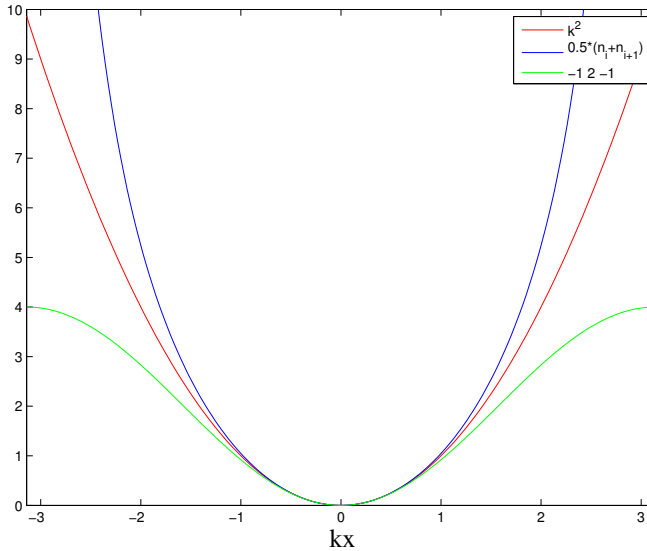


Figure 5.1. Spectra of the Laplace operator, its finite difference and effect of calculating the potential in the centres instead of vertices (when density is interpolated on the grid, like in FEM). It is important to see how Δ_h folds over in high- k , due to $O(k^2)$ error terms.

5.1.2 Comment on the implicit electron model

Explicit schemes for electron dynamics are generally unstable in electrostatic gyrokinetic simulations. This is widely accepted to be due to the ω_H mode [26], which deteriorates the electron solution (see figure 5.3). Several different ways have been suggested as solutions for this problem, such as the split-weight scheme, taking electrons as a fluid, to name a few. These problems are absent in electromagnetic simulations (which have problems of their own), but in electrostatic simulations we have solved this problem by an implicit electron model (see I).

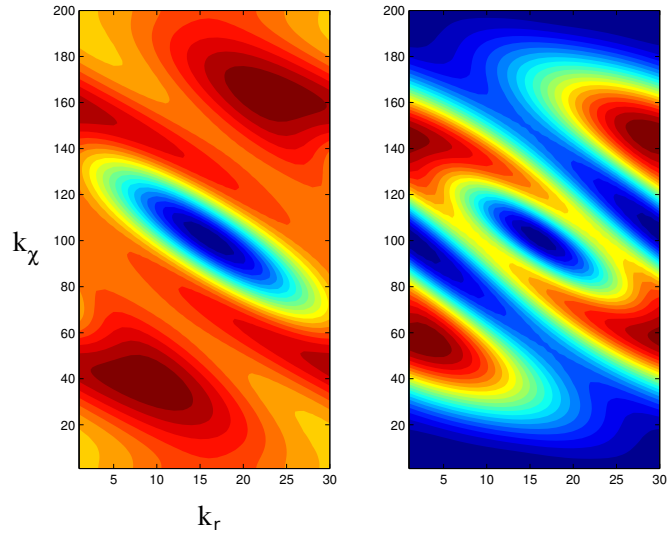


Figure 5.2. Spectra in (k_r, k_χ) -space for the quasi-neutrality operators. We see that the “momentum conserving” interpolation scheme introduces a null-space to the operator (right). Similar behavior may be derived for the Δ_h stencil of $1 - 0 - 2 - 0 - 1$ analytically in 1D. Note the similarity of the spectra in the low- k region, where the Laplacian k^2 -spectrum is accurate (elongation due to non-orthogonal quasi-ballooning coordinates).

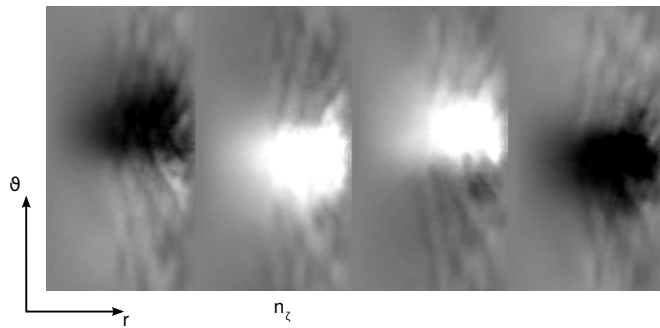


Figure 5.3. Explicit electrons cause a blow-up of electric field, probably due to the ω_H mode; shown as poloidal cross-sections of potential over toroidal sections. On the next time step, the negative values will be positive, and *vice versa*.

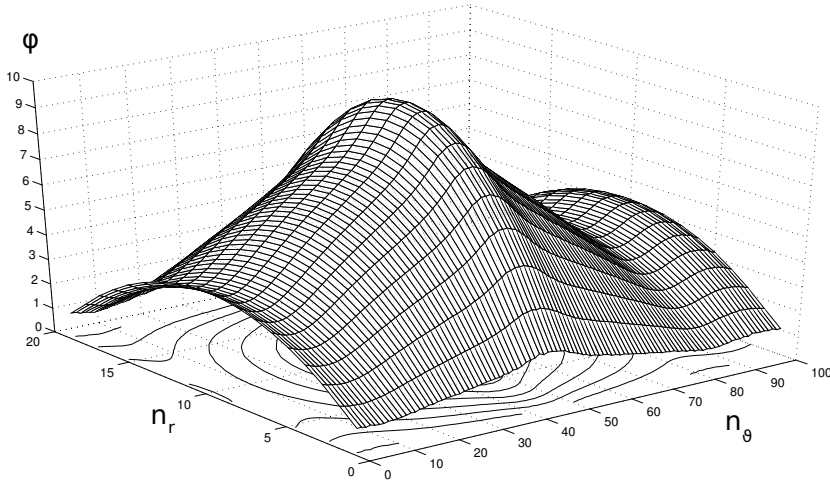


Figure 5.4. Potential disturbance structure created by the localized Maxwell-Boltzmann distribution. Improved initialization on particle orbits removes it completely. The structure is periodic in n_θ .

5.2 Quiescent initialization of the distribution function and toroidal randomization

Naïve initialization with a local Maxwell-Boltzmann distribution, given by

$$f_a(x, v) = n_a(x) \left(\frac{m}{2\pi k_B T} \right)^{3/2} \exp \left\{ -\frac{v_{\parallel}^2 + v_{\perp}^2}{2k_B T} \right\}, \quad (5.4)$$

results in problems in gyrokinetic simulations of tokamak plasmas. The problem is that this distribution is not an eigenfunction of the orbit averaging operator, and therefore causes an initial transient in the electric field when time is allowed to flow (see figure 5.4). Collisional dynamics will relax the distribution eventually, but large dynamic relaxation is undesired in the beginning of turbulence simulations. This problem was already identified and remedied in early simulations with the ASCOT code, where only radial polarization was included [62], and other investigators have later found the same initialization solution widely known as *the canonical Maxwellian* [63]). The techniques to construct this distribution vary. The transient may be eliminated by the following procedure, which has been implemented to ELMFIRE as the preferred option to local Maxwellian:

1. pick particle velocities just like with the local Maxwellian,

2. calculate the particle trajectory over the bounce time ω_B in the absence of \vec{E} ,
3. take particles on this trajectory, and use them for simulation of plasma turbulence.

In the case of equal particle weights, two symmetric particles are initialized instead of a set on the trajectory. The scheme ensures that the distribution is an eigenfunction of the orbit averaging operator, so the violent electric field transient is absent from the simulation.

The quiescent initialization appeared to introduce perturbations in density (see figure 5.5) which were high enough to complicate the growth rate analysis by damping away in the beginning of the linear growth rate analyses while physical modes near the same (m, n) values were being investigated for growth. Unfeasibly high numbers of initialisation markers are needed in poloidal and toroidal directions to suppress this effect (in figure 5.5 we have used 450 million particles). Therefore, in the adiabatic simulations the local Maxwellian initialization was chosen.

Because background flows are suppressed by filtering, the initialization to local Maxwellian does not interfere with the linear dynamics like in the non-linear simulations, which require the quiescent initialization for the reasons mentioned above.

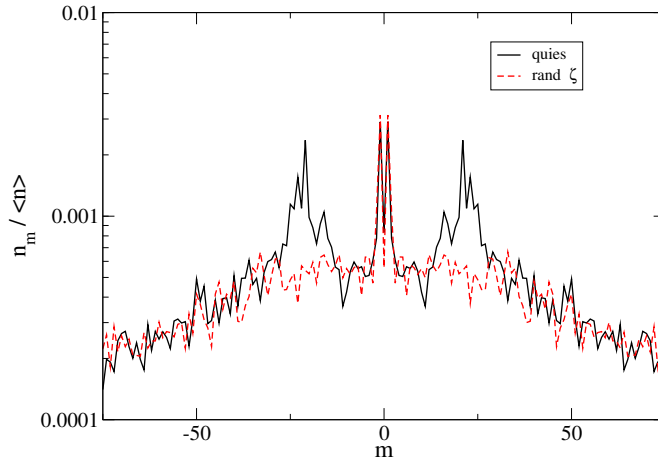


Figure 5.5. Poloidal mode structure (in mode number m) of density in initialization scaled to the flux-surface averaged density. This structure is clearly due to the quiescent initialisation procedure, and can be eliminated by randomisation the ζ -variable of the particles or by using an isotropic Maxwellian initialisation. In this picture the flux-surface averaged value of the zonal component $(0, 0)$ is suppressed.

5.3 Resolution requirements for simulations

Drift-wave turbulence exists in a near-isotropic k_\perp distribution, with the mean $k_x \simeq k_y$. This means that to get a proper turbulence spectrum (and non-linear dynamics), the simulation has to have sufficient overlap of mode spectra on adjacent radial surfaces. This imposes a limit to the radial grid size. Let us assume that locally we may write $q(r) = q_0(1 + \hat{s}(r_0)(r - r_0)/r_0)$, with the shear $\hat{s} = r/q \partial q / \partial r$ (the same for ι , sign reversed). The modes expressed by the quasi-ballooning grid are given by

$$-\frac{N_z}{2} < \frac{m}{q} - n \leq \frac{N_z}{2}, \quad (5.5)$$

so on our reference radius we get $-N_z/2 < m/q_0 - n$ and on the next $-N_z/2 < m/(q_0 + \hat{s} \Delta r/r_0) - n$. Now, to get a uniform spectrum sufficient overlap is needed, which gives us the condition

$$\pi \hat{s} \left[\frac{\Delta r}{r_0 \Delta \theta} - \frac{\Delta r q_0}{r_0 \Delta \zeta} \right] < \Delta m \quad (5.6)$$

where we estimated $n_{\max} \approx m_{\max}/q$, $m_{\max} = \pi/\Delta\theta$ and used $\Delta\zeta = 2\pi/N_z$. Already a few conclusions can be drawn from (5.6): increasing shear will require us to use a smaller radial grid size, and decreasing $\Delta\zeta$ will relax that condition slightly. However, for modest N_z and the requirement that $\Delta m = 1$ we find a simplified condition

$$\frac{\Delta r}{r_0 \Delta \theta} < \frac{1}{\hat{s} \pi}. \quad (5.7)$$

In fact, simulations show that a resolution limit does have a significant impact. If we have too coarse a radial resolution we find that transport levels can be up to a factor of 3 higher than in a case where the resolution condition has been taken into account (see figure 5.6). The resolution

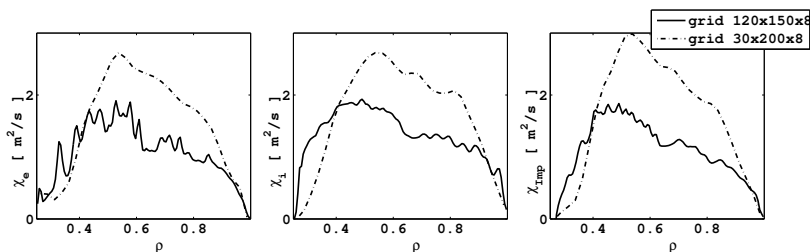


Figure 5.6. Radial resolution impacts χ_i drastically. The case shown is from VII, courtesy of S. Leerink.

limit can be overcome through a different scheme for parallel interpolation, known as the *shifted metric* [64]. This technique has the advantage

of eliminating the complicated quasi-ballooning structure in the computations (all toroidal sections are identical), and only the parallel part of operators require interpolation along the grid. This is more accurate than the quasi-ballooning co-ordinate system, which is $O(h)$, whereas the shifted metric owes its accuracy solely on the accuracy of the interpolation technique which can be of any order. A version of ELMFIRE already incorporates a shifted metric approach, and is being tested for the Cyclone case.

5.4 Impact of averaging in neoclassical simulations

Gyrokinetic particle simulations may be restricted to neoclassical processes by averaging in tokamak plasmas. While this is usually performed by taking only the flux-surface average, it has been observed that the simple flux-surface averaging results in a non-equilibrium distribution function that kick-starts a geodesic acoustic oscillation (GAM) when the simulation is continued without averaging. In addition to the GAM oscillation dynamics, poloidal asymmetry of the electric field is important in impurity dynamics, which is not properly captured by a pure flux-surface average. Non-equilibration of the distribution function may be corrected by including the non-zero m values of the $n = 0$ mode. We propose an orthogonal Fourier basis filtering technique which takes higher m -numbers into account in the electric field, thus removing the spurious GAM oscillation when the simulation is continued without averaging.

The flux surface averaged potential does not allow finite Larmor radius effects to be included, that are important for the dynamics of geodesic acoustic oscillations [65]. Therefore the end state of such simulations is not an equilibrium with respect to GAM oscillations, and it is debatable if they therefore are even an equilibrium of the radial electric field dynamics. The GAM oscillations exhibit the Rosenbluth residual and more complicated dynamics arises due to impurity-ion parallel friction [66]. For this reason, we have applied a technique of averaging the polarization equation starting from the charge separation between electrons and ions which eliminates the turbulent modes but retains the effects of finite Larmor radius and parallel pressure gradients on the neoclassical equilibrium.

In ELMFIRE the polarization operator is constructed so as to have polarization motion of the particles balance any charge separation, which is equivalent to the more widely used approach of separating the polarization density from ion density. This difference complicates filtering,

however, because the electric field solved from polarization needs to be consistent with charge changes locally, and as such may not be separately (outside the solution of the electric potential) averaged.

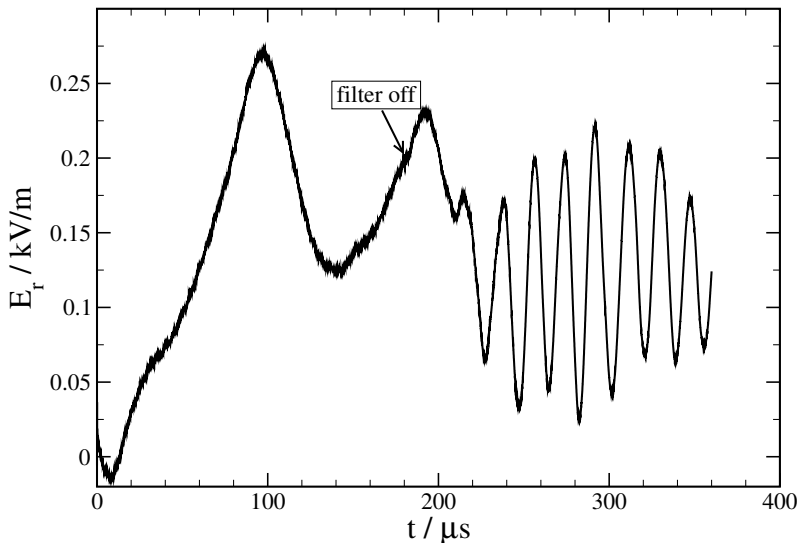


Figure 5.7. Dynamic equilibration of the distribution function due to filtering, which is turned off at $180 \mu\text{s}$. Large oscillations arise only after turbulence develops.

The subtle balance in parallel dynamics in the tokamak frequently produces situations where simple flux-surface averaging is insufficient for capturing the crucial aspects of neoclassical physics. This is illustrated clearly by our physical example: the distribution function thereby generated is not free of dynamical oscillations, and even the saturation radial electric field in the presence of impurities differs greatly depending on the averaging method. However, when non-zero m -modes are included in the filtering technique, the system is undisturbed after filtering is turned off. This is illustrated in figure 5.7.

In the field frequently only flux surface averaged potentials are evolved, which needs to be addressed to obtain better agreement with experiments. This is not a major problem for delta- f codes, but important for full f and gyrofluid codes.

6. Conclusions

This work consists of a mixture of numerics development of ELMFIRE as well as rigorous testing of physical cases with the code. We have developed new techniques of gyrokinetic particle simulation, and a unique technique for kinetic electron treatment. The theoretical basis developed for the code allows for higher order effects and non-linear polarization to be taken into account by changing gyro-sampling points, which appears to allow for easier implementation than the standard formalism. The simulation model is applicable to turbulence and neoclassical analyses due to its use of a binary collision model. We present benchmarking results and comparisons to experiment that solidify confidence to the code and simulation techniques.

We have been able to demonstrate that the simulation recovers neoclassical physics where theory is applicable, and even in cases where recently developed neoclassical theory for impurity dynamics has been needed. The code conserves momentum and energy with proper simulation parameter choices. Diagnostics of these quantities can be used to evaluate if resolution requirements are sufficient.

The most successful linear and non-linear benchmarks of “Cyclone base” case considered in the work are the following: linear growth of the ITG mode for adiabatic electrons, linear growth of the ITG/TEM branch for kinetic electron simulations, and corresponding non-linear simulations with varying temperature profiles. In linear adiabatic analyses excellent results were found, whereas kinetic electron cases were complicated by noise. Analysis of mode energetics made linear growth rate analyses even in these cases possible. The non-linear simulations produced several rather surprising results. The analysis clearly demonstrates that finite orbit effects may in fact play an important role in saturation of transport especially in regards to the standard adiabatic model, and as such,

need to be taken into account in turbulence simulations. Greater particle numbers than expected were needed to obtain well converged non-linear adiabatic simulations of the Cyclone Base case, which was relaxed to all the way to stability through transport.

We investigated the reactive fluid model for turbulent transport scaling that has been developed by Coppi and adopted by Weiland (e.g., in Ref. [12,40]), which is used as a part of transport models. The fluid equations presented in Chapter 3 do capture some of the physics associated with ITG/TEM branch of drift modes, however the model tends to predict excessively high mode growth rates when k_{\perp} is chosen away from the mixing length estimate. With this caveat, we may use this model as an order-of-magnitude estimate for simulation parameters, but more refined models (such as GS2 code) were needed in benchmarking.

The observation that convergence may be improved by increasing the radial simulation box number and particle per cell values allowed us to compare measurements of FT-2 tokamak to simulations. The ELMFIRE has been utilized in interpretation of experimental data obtained from microwave backscattering measurements, with direct measurements of micro- to macro-scale transport phenomena in the FT-2 tokamak being quantitatively reproduced by ELMFIRE predictions. The robust presence of geodesic acoustic modes was later observed also in experiments.

Gyrokinetic particle simulations may be restricted to neoclassical processes by averaging in tokamak plasmas. While this is usually performed by taking only the flux-surface average, it has been observed that the simple flux-surface averaging results in a non-equilibrium distribution function that kick-starts a geodesic acoustic oscillation (GAM) when the simulation is continued without averaging. In addition to the GAM oscillation dynamics, poloidal asymmetry of the electric field is important impurity dynamics, which is not properly captured by a pure flux-surface average. Non-equilibration of the distribution function may be corrected by including $m \neq 0$ modes of the $n = 0$ mode. In this work we proposed an orthogonal Fourier basis filtering technique which takes the non-zonal component into account in the electric field, thus removing the spurious GAM oscillation which arises when the simulation is continued without averaging. This system was used successfully to first develop the neoclassical equilibrium before turning on turbulence in FT-2 Doppler reflectometry comparisons.

One of the outstanding problems of transport processes in tokamaks is

the L-H transition and in general transport barrier formation. We have presented the first self-consistent simulations where heating and cooling processes create a transport barrier like structure in the simulation. The benchmarking that is presented in more detail here was partly motivated by discussions on this work.

The computational requirements of ELMFIRE have slowed progress in investigations, but with the current generation of supercomputers it can tackle many important questions of transport. Only full f and total- f codes (or, δf code iteration within transport models) can be expected to produce a meaningful steady state for experimental set-ups. This seems to be the direction most other codes are going. To improve ELMFIRE's applicability in broader regimes, especially geometry and inclusion of magnetostatics need to be considered in the future. An improved SOL model for limiter tokamaks is already projected as a short-term goal, which may later be expanded with other developments to a shaped divertor configuration. At this stage, the code would be able to treat a much broader set of instabilities (and turbulence thereof), such as kinetic ballooning and drift-Alfén modes. Also, implementation of the full pullback transformations enable investigations of strongly driven systems where short wavelength (electron) modes co-exist with fluid modes, in addition to the moderate wavelength modes ($k_{\perp} \rho_s \leq 1$) that are simulated now.

Using the ELMFIRE code as an investigative platform, we may be able to develop more cost-effective fusion reactors to the DEMO phase and beyond.

Bibliography

- [1] J. Lovelock, “Gaia: A New Look at Life on Earth”, Oxford Publishing (2000)
- [2] J.M. Diamond, “Collapse: How Societies Choose to Fail or Succeed”, Viking Press (2005)
- [3] H. Biglari, P. H. Diamond, and P. W. Terry, “Influence of sheared poloidal rotation on edge turbulence”, *Phys. Fluids B* **2** 1 (1990)
- [4] J.W. Connor and H.R. Wilson, “A review of theories of the L-H transition”, *Plasma Phys. Control. Fusion* **42** R1 (2000)
- [5] B. Scott, private communication
- [6] R. D. Hazeltine, J. D. Meiss, “Plasma Confinement”, Addison-Wesley (1992)
- [7] J.B. Taylor and R.J. Hastie, *Plasma Phys* **10**, 479 (1968)
- [8] W.W. Lee, *Phys. Fluids* **26**, 556–562 (1983)
- [9] D.H.E. Dubin *et al.*, *Phys. Fluids* **26**, 3524–3535 (1983)
- [10] R.D. Sydora, “Three-dimensional gyrokinetic particle simulation of low-frequency drift instabilities”, *Physics of Fluids B* **2**, 1455 (1990).
- [11] S.E. Parker and W.W. Lee, *Phys. Fluids* **B5**, 77 (1993).
- [12] A.M. Dimits *et al.*, *Phys. Plasmas* **7**, 969–983 (2000)
- [13] Y. Chen and S. Parker, *Phys. Plasmas* **7**, 2095 (2001).
- [14] F. Jenko and W. Dorland, *Plasmas Phys. Controlled Fusion* **43**, A141 (2001).
- [15] Z. Lin and W.W. Lee, *Phys. Rev. E* **52**, 5646 (1995).

- [16] L. Villard *et al.*, *Nucl. Fusion* **44**, 172-180 (2004).
- [17] P.P. Sosenko, P. Bertrand, and V.K. Decyk, *Physica Scripta* **64**, 264 (2001)
- [18] A.J. Brizard and T.S. Hahm, “Foundations of nonlinear gyrokinetic theory”, *Reviews of Modern Physics* **79** 421–468 (2007)
- [19] J.L.V. Lewandowski *et al.*, *Phys. Plasmas* **13**, 072306 (2006)
- [20] B. Scott, *Proc. 33rd EPS Conf.*, Rome (2006)
- [21] Y. Sarazin *et al.*, *Proc. 33rd EPS Conf.*, Rome (2006)
- [22] J.A. Heikkinen, S.J. Janhunen, T.P. Kiviniemi, F. Ogando, *Journal of Computational Physics* **227** 5582 (2008)
- [23] A.B. Langdon, *Phys. Fluids* **22**, 163 (1979)
- [24] Z. Lin *et al.*, *Proc. 24th IAEA FEC*, TH8/4 (2004)
- [25] C.K. Birdsall and A. B. Langdon, “Plasma physics via computer simulation”, Taylor & Francis Group (2005)
- [26] W. W. Lee, “Gyrokinetic Particle Simulation Model”, *J. of Comp. Physics* **72**, 243 (1987)
- [27] J. A. Heikkinen and M. Nora, *Phys. Plasmas* **18** 022310 (2011)
- [28] D. Pfirsch and D. Correa-Restrepo, *J. Plasma Phys.* **70**, 719 (2004).
- [29] D. Correa-Restrepo and D. Pfirsch, *J. Plasma Phys.* **70**, 757 (2004).
- [30] M. Kruskal, *J. Math. Phys.* **3**, 806 (1962).
- [31] J. Larsson, *J. Math. Phys.* **27**, 495 (1986).
- [32] R.G. Littlejohn, *J. Plasma Phys.* **29**, 111 (1983).
- [33] H. Sugama, *Phys. Plasmas* **7**, 466 (2000).
- [34] H. Qin, R.R. Cohen, W.M. Nevins, and X.Q. Xu, *Contrib. Plasma Phys.* **46**, 473 (2006).
- [35] A. M. Dimits, “Fluid simulations of tokamak turbulence in quasiballooning coordinates”, *Phys. Review E* **48** 5 4070 (1993)
- [36] F.I. Parra and P. Catto, *Plasma Phys. Controll. Fusion* **50**, 065014 (2008).

- [37] R. B. White, "Theory of Tokamak Plasmas", North-Holland (1989)
- [38] R. B. White, M. S. Chance, "Hamiltonian guiding center drift orbit calculation for plasmas of arbitrary cross section", *Phys. Fluids* **27** 10, 2455 (1984)
- [39] R. B. White, A. H. Boozer, "Rapid guiding center calculations", *Phys. Plasmas* **2** 8 (1995)
- [40] J. Weiland, "Collective Modes in Inhomogeneous Plasma; Kinetic and Advanced Fluid Theory", IOP Publishing Ltd (2000)
- [41] P. Helander, D.J. Sigmar, "Collisional transport in magnetized plasmas", Cambridge monographs on plasma physics (2002)
- [42] M. Kotschenreuther, G. Rewoldt, and W.M. Tang, "Comparison of Initial Value and Eigenvalue Codes for Kinetic Toroidal Plasma Instabilities", *Computer Physics Communications* **88** 128 (1995).
- [43] A. Bottino, A. G. Peeters *et al.*, "Nonlinear low noise particle-in-cell simulations of electron temperature gradient driven turbulence", *Phys. Plasmas* **14** 010701 (2007)
- [44] Y. Chen, S.E. Parker *et al.*, "Simulations of turbulent transport with kinetic electrons and electromagnetic effects", *Nuclear Fusion* **43** 1121-1127 (2003)
- [45] M. Fivaz *et al.*, "Finite element approach to global gyrokinetic Particle-In-Cell simulations using magnetic coordinates", *Comp. Phys. Comm.* **111** 27 (1998)
- [46] R. Balescu, "Aspects of anomalous transport in plasmas", IOP Series in Plasma Physics (2005)
- [47] Connaughton C.P., Nadiga B.T., Nazarenko S. and Quinn B.E., "Modulational instability of Rossby and drift waves and generation of zonal jets", *Journal of Fluid Mechanics* **654** 207-231 (2010)
- [48] Kim C. B., "Scalings of forced Hasegawa Mima equation by power-law noise", *Plasma Phys. Control. Fusion* **54** 085021 (2012)
- [49] F. Chen, "Spectrum of low- β plasma turbulence", *Physical Review Letters* **15** 9 381 (1965)
- [50] S.J. Camargo, D. Biskamp, B.D. Scott, "Resistive drift-wave turbulence", *Physics of Plasmas* **2** 1 (1995)

- [51] T.E. Stringer, "Different forms of the plasma energy conservation equation", *Plasma Physics and Controlled Fusion* **33** 14 1715-1722 (1991)
- [52] C.S. Chang, "Enhancement of neoclassical transport coefficients by a poloidal electric field in tokamaks", *Physics of Fluids* **26** 8 2140-2149 (1983)
- [53] S. Ma, R.D. Sydora, J.M. Dawson, Binary collision model in gyrokinetic simulation of plasmas, *Comput. Phys. Commun.* **77** 190 (1993)
- [54] B. F. McMillan, S. Jolliet, T. M. Tran, L. Villard, A. Bottino, and P. Angelino, "Long global gyrokinetic simulations: Source terms and particle noise control", *Physics of Plasmas* **15** 5 052308 (2008).
- [55] S.I. Krasheninnikov and P.N. Yushmanov, "The influence of a radial electric-field on neoclassical orbits and ion prompt losses from tokamak edge plasmas", *Physics of Plasmas* **1** 1186 (1999)
- [56] S. Jolliet, A. Bottino, P. Angelino et al., "Ion and electron dynamics in nonlinear PIC simulations", *AIP Conference Proc.* 871, 124 (2006).
- [57] S.E. Parker, C. Kim, and Y. Chen, "Large-scale gyrokinetic turbulence simulations: effects of profile variation", *Phys. Plasmas* **6** 1709 (1999).
- [58] T.P. Kiviniemi, J.A. Heikkinen, S.J. Janhunen, "Full f particle simulation of internal transport barrier formation", 32nd EPS Conference on Plasma Phys. Tarragona, 27 June - 1 July 2005 ECA Vol.29C, P-2.022 (2005)
- [59] J.A. Heikkinen, S.Henriksson, S. Janhunen ; T.P. Kiviniemi, M. Nora, F. Ogando, "Full f gyrokinetic simulation of transport in tokamak plasmas", 33rd EPS Conference on Plasma Phys. Rome, 19 - 23 June 2006 ECA Vol.30I, P-4.158 (2006)
- [60] J.A. Heikkinen, T.P. Kiviniemi, A.G. Peeters, "Neoclassical radial current balance in tokamaks and transition to the H-mode", *Physical Review Letters* **84** pp. 487-490 (2000)
- [61] Stringer T.E., "Neoclassical transport in the presence of fluctuations", *Nuclear Fusion* **32**/8 1421 (1992)

- [62] J.A Heikkinen, T.P Kiviniemi, T Kurki-Suonio, A.G Peeters, S.K Sipilä, “Particle Simulation of the Neoclassical Plasmas”, *Journal of Computational Physics* **173** 2 527 548 (2001)
- [63] P. Angelino, A. Bottino, R. Hatzky, S. Jolliet, O. Sauter, T. M. Tran, and L. Villard, “On the definition of a kinetic equilibrium in global gyrokinetic simulations”, *Phys. Plasmas* 13, 052304 (2006)
- [64] Scott B, “Shifted metric procedure for flux tube treatments of toroidal geometry: Avoiding grid deformation”, *Physics of Plasmas* **8** 447 (2001)
- [65] Falchetto G L, Ottaviani M, Garbet X, Smolyakov A 2007 *Physics of Plasmas* **14** 082304
- [66] Landreman M, Fulop T 2011 *Physics of plasmas* **18**

Energies involved in nuclear bonds are more than million times higher than those in chemical bonds. This makes it possible to create very effective reactors for energy production: by splitting heavy nuclei (fission) or by merging light nuclei (fusion). Energy produced in fusion reactions exceed that of fission by an order of magnitude, but the realization of a commercial fusion reactor has up to now eluded scientists due to the high energy barrier for achieving them. The best performing fusion device is the *tokamak*, where the thermonuclear plasma is confined using strong magnetic fields in toroidal configuration. One major factor that decreases efficiency, and hence power production, is turbulent transport. In *Iter*, the next big fusion device with the projected capability of considerable net energy production, transport has been optimized by enlarging the plasma cross-section. However, this is an expensive road to take.

In this work we describe development and benchmarking of a kinetic model capable of simulating turbulent transport in tokamaks.



ISBN 978-952-60-5098-0
ISBN 978-952-60-5099-7 (pdf)
ISSN-L 1799-4934
ISSN 1799-4934
ISSN 1799-4942 (pdf)

Aalto University
School of Science
Department of Applied Physics
www.aalto.fi

BUSINESS +
ECONOMY

ART +
DESIGN +
ARCHITECTURE

SCIENCE +
TECHNOLOGY

CROSSOVER

DOCTORAL
DISSERTATIONS